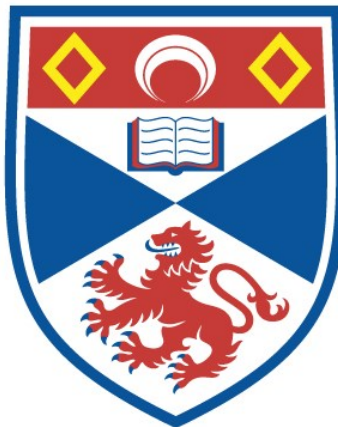


**The effects of partial ionization on
magnetic flux emergence and solar
eruptive events**

Georgios Chouliaras

A thesis submitted for the degree of PhD
at the
University of St Andrews



2025

Full metadata for this thesis is available in
St Andrews Research Repository
at:
<https://research-repository.st-andrews.ac.uk/>

Identifier to use to cite or link to this thesis:
DOI: <https://doi.org/10.17630/sta/1179>

This item is protected by original copyright

This item is licensed under a
Creative Commons Licence

<https://creativecommons.org/licenses/by-nc-nd/4.0/>

Abstract

The process of magnetic flux emergence is closely linked to the formation of solar active regions, which are the main sites for most solar eruptions. The Sun's lower atmosphere and a part of its upper convection zone are partially ionized. In this thesis, we modified the one-fluid magnetohydrodynamic equations to include the effects of partial ionization. Our work involves comparing two simulation scenarios: one with a fully ionized plasma (FI) and the other with a partially ionized plasma (PI). We analyzed and compared these scenarios in both an unmagnetized solar atmosphere and a magnetized solar atmosphere.

Our analysis shows that in the PI case, less dense plasma rises more easily to the photospheric layer than in the FI case. The PI plasma changes the structure of the emerging magnetic field, shaping bipolar regions differently and causing the magnetic field to expand upwards sooner. We have found that partial ionization reduces cooling during adiabatic expansion but does not heat the atmospheric plasma. In our 3D experiments, we have found that PI does not prevent coronal unstable magnetic structures from erupting into the outer solar atmosphere. The failed emergence of the flux tube axis in the PI case created differences in the dynamical evolution of the magnetic field in the solar atmosphere compared to the FI case. We also observed differences in temperature, density, and vertical velocity profiles during eruptions, highlighting the impact of partial ionization in the lower atmosphere and upper convection zone.

Comparing PI and FI simulations in a magnetized corona, we found that the first reconnection jet is a multithermal jet and is slower, cooler, and less dense in PI than in FI. For inverted-Y-shaped standard jet we find that the PI jet is less hot, less dense, but faster than the FI jet. We have found the presence of mini-filament-structures in both simulations. We have found that PI have more energetic blowout jets. To conclude this PhD thesis provided new results and shed light on the effects of the partially ionized plasma on magnetic flux emergence and solar eruptive events.

Candidate's Declaration

I, Georgios Chouliaras, do hereby certify that this thesis, submitted for the degree of PhD, which is approximately 30,000 words in length, has been written by me, and that it is the record of work carried out by me, or principally by myself in collaboration with others as acknowledged, and that it has not been submitted in any previous application for any degree. I confirm that any appendices included in my thesis contain only material permitted by the *Assessment of Postgraduate Research Students* policy.

I was admitted as a research student at the University of St Andrews in September 2020.

I received funding from an organisation or institution and have acknowledged the funder(s) in the full text of my thesis.

Date: _____

Signature of candidate: _____

Supervisor's Declaration

I hereby certify that the candidate has fulfilled the conditions of the Resolution and Regulations appropriate for the degree of PhD in the University of St Andrews and that the candidate is qualified to submit this thesis in application for that degree. I confirm that any appendices included in the thesis contain only material permitted by the *Assessment of Postgraduate Research Students* policy.

Date: _____

Signature of supervisor: _____

Permission for Publication

In submitting this thesis to the University of St Andrews we understand that we are giving permission for it to be made available for use in accordance with the regulations of the University Library for the time being in force, subject to any copyright vested in the work not being affected thereby. We also understand, unless exempt by an award of an embargo as requested below, that the title and the abstract will be published, and that a copy of the work may be made and supplied to any bona fide library or research worker, that this thesis will be electronically accessible for personal or research use and that the library has the right to migrate this thesis into new electronic forms as required to ensure continued access to the thesis.

I, Georgios Chouliaras, confirm that my thesis does not contain any third-party material that requires copyright clearance.

The following is an agreed request by candidate and supervisor regarding the publication of this thesis:

Printed Copy

No embargo on print copy.

Electronic Copy

No embargo on electronic copy.

Date: _____

Signature of candidate: _____

Date: _____

Signature of supervisor: _____

Underpinning Research Data or Digital Outputs

Candidate's Declaration

I, Georgios Chouliaras, hereby certify that no requirements to deposit original research data or digital outputs apply to this thesis and that, where appropriate, secondary data used have been referenced in the full text of my thesis.

Date: _____

Signature of candidate: _____

General acknowledgements

I would first like to express my gratitude to my supervisor, Dr. Vasilis Archontis, for his support and guidance throughout my PhD research. I also extend my thanks to the entire Solar and Magnetospheric Theory group for being available to answer every question—whether related to research or not—during my PhD journey. The weekly seminars and the insightful questions, suggestions, and advice from all the experienced scientists in the group were invaluable and contributed to the improvement of this thesis.

I am grateful to my friends who made my time living in St Andrews enjoyable. Last but certainly not least, I must thank the real heroes: my family Argyris, Athena and Orestis and my life partner, Stefania, who provided unwavering moral and spiritual support throughout these years. Their help was instrumental in overcoming the challenges of this PhD journey, and without them, the completion of this degree would have remained a mere fantasy.

Funding

This work was supported by the European Research Council through the Synergy grant No. 810218 (“The Whole Sun,” ERC-2018-SyG).

This work was supported by the Royal Society grant RGF/EA/180232.

Publications

- Effects of partial ionization on magnetic flux emergence in the Sun. Chouliaras et al 2023: <https://ui.adsabs.harvard.edu/abs/2023ApJ...952...21C>
- Magnetic flux emergence and solar eruptions in partially ionized plasmas. Chouliaras et al 2024 (Submitted to ApJ)
- Energy and helicity evolution in a flux emergence simulation. K. Moraitis, V. Archontis, and G. Chouliaras 2024 (Submitted to A&A)

Let the future tell the truth, and evaluate each one according to his work and accomplishments. The present is theirs; the future, for which I have really worked, is mine.

— *Nikola Tesla*

Contents

1	Introduction	1
1.1	The Sun	1
1.1.1	The Sun's interior	2
1.1.2	The Sun's atmosphere	3
1.2	Magnetohydrodynamic equations	7
2	The magnetic flux emergence process	15
2.0.1	The magnetic buoyancy and the magnetic flux tubes	16
2.1	Numerical simulations	19
2.1.1	Solar eruptions and solar jets	27
2.2	Partial ionization	29
2.2.1	Models that determine the environmental profile of the Sun. . .	30
3	Effects of partial ionization on the magnetic flux emergence in the Sun.	35
3.1	Our Model	35
3.1.1	The Lare3D code	35
3.1.2	Equations	37
3.1.3	Initial conditions	43
3.2	Results	51
3.2.1	Magnetic flux emergence through the solar convection zone .	51
3.2.2	Emergence of Magnetic Flux at the photosphere	53
3.2.3	Evolution of Flux and Energy	56
3.2.4	Magnetic flux emergence at solar atmosphere	62
3.3	Discussion	66

4 Effects of partial ionization on solar eruptions.	69
4.1 Results	69
4.1.1 Analysis of the Pre-Eruptive Stage	69
4.1.2 Topology of fieldlines and height-time profile.	72
4.1.3 The rising motion of the erupting field	77
4.1.4 The first eruption	78
4.1.5 Energy evolution during eruptions	80
4.1.6 Neutrals, emergence, and eruptions	83
4.2 Discussion	84
5 Effects of partial ionization on solar jets.	87
5.1 Numerical Setup	88
5.2 Results	89
5.2.1 The Emergence of the Magnetic Flux to the solar surface.	89
5.2.2 The comparison of the kinetic energy budget of the solar eruptive events.	90
5.2.3 Comparison of the standard jets.	92
5.2.4 Comparison and evolution of the eruption driven jets.	104
5.2.5 The blowout jets	106
5.2.6 The dynamic evolution of the blowout jets in PI.	106
5.3 Discussion	112
6 Conclusions	115

Chapter 1

Introduction

1.1 The Sun

The stars constitute the sources that provide chemical elements to the interstellar medium throughout their life and more significantly at the end of it. They have been formed from the gravitational collapse of molecular clouds. At their core they build energy from the nuclear fusion of hydrogen to helium, but also with other elements, the resulted radiation pressure counters their own gravitational pressure in order to stay in hydrodynamic equilibrium. The star in our solar system called the Sun, has mass of approximately $M_{\odot} = 1.99 \times 10^{30} \text{ kg}$ and radius $R_{\odot} = 6.960 \times 10^8 \text{ m}$. All the information about the Sun have been taken by the following books (Golub & Pasachoff, 1997; Stix, 2002). Currently is on the main sequence of its evolution. This number is so vast that in our solar system (planets, asteroids etc.) is the 99% of the total mass. The age of the Sun is approximately 4.6 billion years and it will spend on the main sequence of its evolution 4.4 billion years more. Its temperature distribution varies tremendously from its core (15 million Kelvin) till its surface (5500K) and corona (1 – 2 million Kelvin). Due to the high temperature the bulk mass on the Sun is at the fourth state of the matter called plasma. It consists of electrons, ions (atomic nuclei), photons and neutral atoms at some specific layers.

1.1.1 The Sun's interior

The solar interior, being optically thick, prevents radiation from escaping easily. As a result, we cannot directly detect photons from this region, making it challenging to assess its structure. However, we can infer details about it based on our understanding of physics, particularly through the field of helioseismology (Kosovichev & Zharkova, 1998; Lindsey & Braun, 2000; Hathaway et al., 2000; Beck & Schou, 2000). The solar interior consists of three distinct regions, each characterized by unique physical processes: the core, the radiative zone, and the convection zone.

A fundamental source of life on Earth is the energy emanating from the Sun. This energy primarily originates from the Sun's core, where it is produced through the nuclear fusion of hydrogen into helium and other elements.



The Helium atom consists of 2 protons and 2 neutrons, but the actual mass of Helium is less than the sum of the masses of 2 protons and 2 neutrons. This mass deficit is the source of energy produced in the nuclear reaction, as described by the equation $E = mc^2$. This energy is emitted in the form of two γ -rays, each with an energy equivalent of 26.7 MeV, and two electron neutrinos that propagate outwards, interacting minimally with the matter of the solar interior.

This energy is transported through the radiative zone via radiative diffusion. The energy travels in the form of electromagnetic radiation (photons). High energy photons enter a high-density environment, where they are absorbed and re-emitted numerous times due to collisions with plasma particles. The mean free path for the radiation is only about 1 cm. Consequently, it takes approximately 1.60×10^5 years for the photons to cross the radiative zone, which spans approximately $0.7R_\odot$ in length.

The radiative interior, including the core, rotates approximately as a rigid body, while the convection zone rotates at a different rate cause of differential rotation. This creates a shear layer at the bottom of the convection zone known as the tachocline, analogous to the ocean's thermocline (Spiegel 1992). Helioseismology has been utilized to detect this layer, which is thought to be a transition zone from the radiative to the convection zone. It is believed that the toroidal fields,

which later create active regions, are generated in the tachocline through dynamo processes. (Tobias et al., 1995; Kichatinov & Rüdiger, 1996; Brun & Zahn, 2006; Hughes, 2007) The convection zone is dominated by turbulence (Reynolds number $\approx 10^{12}$), significantly impacting numerical simulations due to high diffusivities. In this zone, the primary heat transfer mechanism is convection, although radiative transfer still plays a role.

1.1.2 The Sun's atmosphere

The Solar atmosphere is primarily divided into four different regions: the photosphere, which is essentially the solar surface, the chromosphere, the transition region, and the solar corona.

The photosphere is the thinnest layer of the solar atmosphere with a thickness of 500 km, yet it has the lowest temperature, which is several thousand Kelvin. In figure 1.1 we observe that the solar surface undergoes a granulation effect where hot plasma ascends from below and forms granules that “live” for nearly 20 minutes. Then, the plasma cools and begins to descend at the edges of the granule, creating a downflow in this specific region. The granulation can be locally disrupted by the presence of sunspots and strong magnetic fields. The optical depth is a parameter that provides information about the transparency of a medium and is defined by the following equation:

$$I = I_0 e^{-\tau} \quad (1.2)$$

where I is the intensity of the observed radiation after it has crossed a medium, and I_0 is the intensity of the radiation generated by the original source. At the boundary of $\tau = 1$, the initial intensity has dropped by a factor of e . The photosphere, with an optical depth $\tau < 1$, is the region from which radiation can escape. Indeed, the photosphere, deriving its name from the Greek word “phos” meaning light, is the layer from which we receive solar radiation. Figure 1.2 depicts the complexity of the photospheric magnetic field that ascends from below in bipolar modes, forming bipolar regions. We observe the dynamics of the photospheric magnetic field via magnetograms, gaining information to infer the role of the photospheric magnetic field in the formation of active regions and sunspots.

Above the photosphere lies a thin layer called the chromosphere with a thickness of 2,500K. Its density is 10^{-4} times that of the photosphere, and due to the brightness of the photosphere, it is not observable under regular circumstances. We can observe it during a solar eclipse, where it appears as a reddish thin layer due to the red color of the Balmer spectrum. This density decrease can be described mathematically using the concept of scale height, λ , which represents the characteristic distance over which the density falls by a factor of e . Using the relation $\rho = \rho_0 e^{-\frac{z}{\lambda}}$,

where ρ is the density at height z , we can estimate that the chromosphere lies approximately 9.2 scale heights above the photosphere. This means that the density at this height has dropped by a factor of 10^4 , consistent with the observed difference in density between the chromosphere and the photosphere. The temperature varies from 3,800K to 3×10^4 K at the upper boundary before the transition region. The dynamic nature of the solar magnetic field is also visible in this layer, with structures such as prominences, filaments, and spicules. Prominences are thought to be luminous arcade structures consisting of cool chromospheric material. They usually stay within the magnetic field loop and its cool plasma due to the adiabatic expansion of the loop. Prominences remain confined within the magnetic field loop because the magnetic field exerts forces that trap the cooler, denser plasma. The magnetic pressure and tension of the field lines provide stability and prevent the plasma from dispersing. This confinement allows prominences to persist for extended periods within the corona, which is otherwise much hotter and less dense. While prominences are made of much cooler and denser plasma compared to the surrounding corona, they are indeed set within the corona. The cooler chromospheric material that makes up prominences is suspended in the hot, tenuous plasma of the corona, confined by the magnetic field loops. Despite the temperature contrast, they are considered a part of the Sun's outer atmosphere. Filaments are essentially the same as prominences; the only difference is that filaments are observed on the solar disk, while prominences are seen on the solar limb. Both can erupt and may evolve into a Coronal Mass Ejection (CME) when they reach the corona.

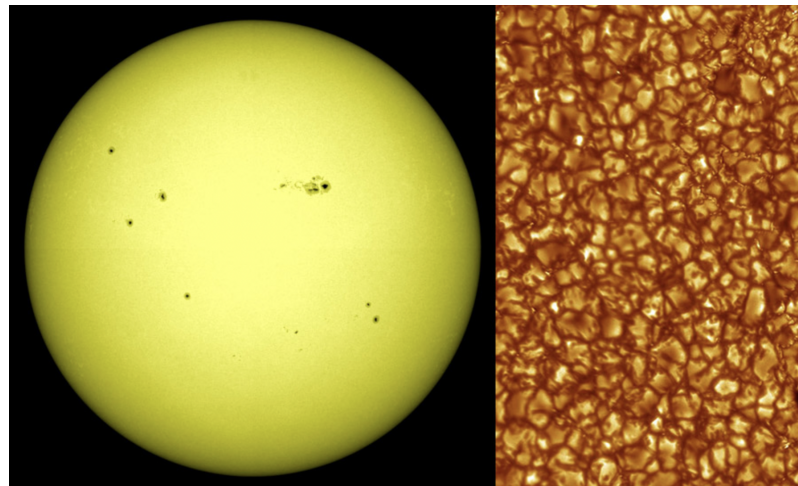


Figure 1.1: 2 images that display sun spots (left) and the granulation that takes place in the photosphere (right). References:NASA/SDO and the AIA, EVE, and HMI science teams (left); Royal Swedish Academy of Sciences - Oddbjorn Engvold, Jun Elin Wiik, Luc Rouppe van der Voort (right)

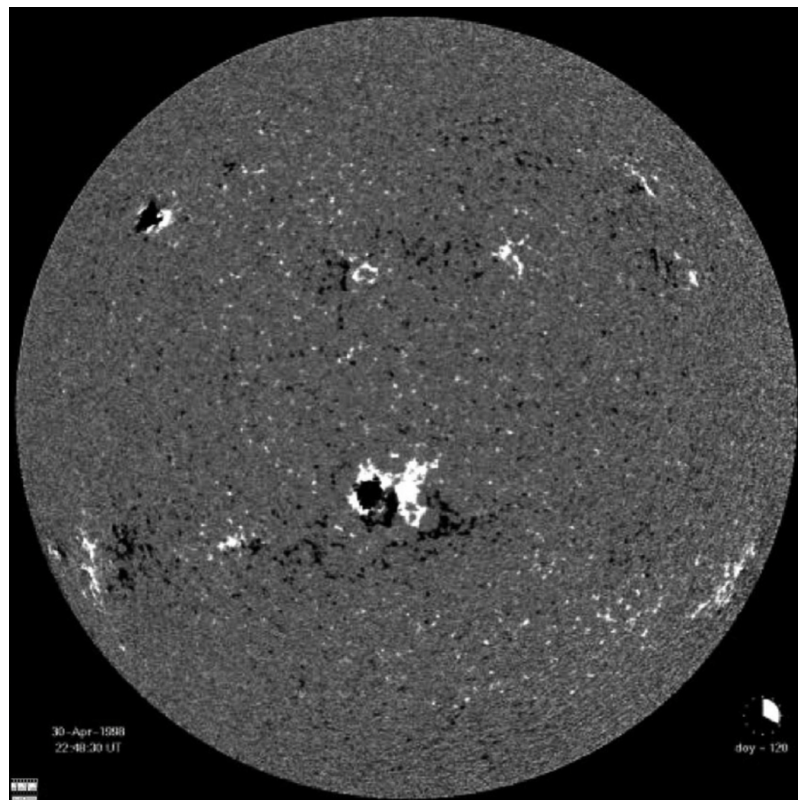


Figure 1.2: A global magnetogram that depicts the positive vertical component of the magnetic field as white and the negative one as black. From the MDI instrument on the ESA/NASA SoHO spacecraft figure in Priest (2012)

The boundary layer that divides the chromosphere from the top layer of the solar atmosphere is called the transition region. It is nearly 100 km thick, and in this region, the temperature grows exponentially, reaching values of 1 MK at the start of the corona. In this region, the gas pressure is much smaller than the magnetic pressure. Consequently, the plasma beta (β)—the ratio of gas pressure to magnetic pressure—is far less than 1. Therefore, the magnetic field dominates the physical processes governing the dynamic evolution of this layer, rendering the transition region non-uniform. This magnetic dominance affects our ability to accurately define the boundaries of this layer.

To illustrate this, consider the following calculations:

1. Gas Pressure (P_{gas}):

$$P_{\text{gas}} = nk_{\text{B}}T$$

Where:

- n is the particle number density.
- k_{B} is the Boltzmann constant (1.38×10^{-16} erg K $^{-1}$).
- T is the temperature.

Using typical values for the solar transition region Priest (2014):

$$n = 1 \times 10^{11} \text{ cm}^{-3}, \quad T = 1 \times 10^5 \text{ K}$$

Calculation:

$$P_{\text{gas}} = nk_{\text{B}}T = (1 \times 10^{11} \text{ cm}^{-3})(1.38 \times 10^{-16} \text{ erg K}^{-1})(1 \times 10^5 \text{ K}) = 1.38 \text{ erg cm}^{-3}$$

2. Magnetic Pressure (P_{mag}):

$$P_{\text{mag}} = \frac{B^2}{8\pi}$$

For a magnetic field strength of $B = 10$ G:

$$P_{\text{mag}} = \frac{(10 \text{ G})^2}{8\pi} = \frac{100}{25.13} \approx 3.98 \text{ erg cm}^{-3}$$

3. Plasma Beta (β):

$$\beta = \frac{P_{\text{gas}}}{P_{\text{mag}}} = \frac{1.38}{3.98} \approx 0.35$$

Since $\beta < 1$, the magnetic pressure dominates over the gas pressure. Therefore, the dominant physical processes for the dynamic evolution of this layer are governed by the magnetic field, making the transition region non-uniform. This significantly affects our ability to accurately define the boundaries of this layer.

The final layer of the solar atmosphere is the corona. The temperature values here show substantial differences compared to the solar surface. Until 1940, it was believed that the temperature of the Sun decreases with height. After 1940, it was well-established that the temperature in the corona exceeds 1 MK, introducing a significant scientific query that remains unresolved. The heating mechanism underlying this phenomenon is discussed in Parnell & De Moortel (2012). As the magnetic field dominates the dynamics in this region, the heating mechanism is believed to be directly linked to it.

1.2 Magnetohydrodynamic equations

Suppose a system with a moving electrically conductive fluid in a magnetized medium. To assess the behavior of this system, one should couple the laws of hydrodynamics (Navier-Stokes equations) and electromagnetism (Maxwell's equations). This coupled set of equations is called the Magnetohydrodynamic (MHD) set of equations

and examines the behavior of a moving electrically conductive fluid in a magnetized medium. MHD has three effects that simply explain the behavior of this system from the physics point of view. The relative motion between the conducting fluid and the magnetic field will create an electromotive force with magnitude $|\mathbf{u} \times \mathbf{B}|$, where \mathbf{u} is the velocity vector field and \mathbf{B} is the magnetic field, a result from Faraday's law of induction. Ampere's law is used to explain that these induced currents will induce a second magnetic field, and this interaction will have a physical interpretation that the fluid is "dragging" the magnetic field lines. The overall magnetic field will interact with the induced currents in the form of the magnetic Lorentz force $\mathbf{J} \times \mathbf{B}$, acting perpendicular to the plane defined by the current density and the combined magnetic field. This means that the magnetic field will "pull" the conductive fluid. This can be thought of as the magnetic field lines being frozen in the plasma flow. This idea, which constitutes the Alfvén theorem, was proposed in 1942 by Hannes Alfvén and is the fundamental principle of MHD.

James Clark Maxwell was the one who tried to explain the dynamic behavior of an electromagnetic field with the following four equations:

1. Solenoidal condition:

$$\nabla \cdot \mathbf{B} = 0, \quad (1.3)$$

This condition implies that magnetic field lines neither start nor end but form continuous loops. It arises from one of Maxwell's equations, specifically Gauss's law for magnetism, which states that the net magnetic flux through any closed surface is zero. This reflects the non-existence of magnetic monopoles and ensures the field is conserved and divergence-free.

2. Ampere's law:

$$\nabla \times \mathbf{B} = \mu_0 \mathbf{J} + \frac{1}{c^2} \frac{\partial \mathbf{E}}{\partial t}, \quad (1.4)$$

It basically states that the movement of a current will induce a magnetic field.

3. Faraday's law:

$$\nabla \times \mathbf{E} = - \frac{\partial \mathbf{B}}{\partial t}, \quad (1.5)$$

This law implies that a changing magnetic field over time induces a circulating electric field, which is essential for the dynamics of conducting fluids in a plasma. This induced electric field influences the motion of charged particles, contributing to the complex behavior of the plasma in the presence of magnetic fields.

4. Gauss's law:

$$\nabla \cdot \mathbf{E} = \frac{\rho}{\epsilon_0}, \quad (1.6)$$

Equations (1.5) and (1.6) imply that a non-steady magnetic field or a non-zero charge distribution (ρ) can create an electric field.

To the above set of equations, \mathbf{J} is the current density, \mathbf{E} is the electric field, c is the speed of light, ϵ_0 represents the permittivity of free space with a value of $8.854 \times 10^{-12} \text{ F m}^{-1}$, and μ_0 is the magnetic permeability with a value of $4\pi \times 10^{-7} \text{ H m}^{-1}$. These two parameters can be combined to yield the square of the speed of light:

$$c^2 = \frac{1}{\mu_0 \epsilon_0} \quad (1.7)$$

In this thesis, we limit ourselves to velocities that are far smaller than the speed of light (normal MHD). In particular, such an approximation has an effect on Ampere's law, which simplifies to:

$$\nabla \times \mathbf{B} = \mu_0 \mathbf{J}. \quad (1.8)$$

Another characteristic that solar plasmas possess is charge neutrality. Inside the plasma, the cumulative sum of the number densities of negative and positive ions will be much smaller than the total number density:

$$n^+ - n^- \ll n, \quad (1.9)$$

Ohm's Law

Assuming a frame of reference moving in the same way as the plasma in the presence of a magnetic field, Ohm's law provides information about the current

density. According to this law, the current density is proportional to the total electric field (both the initial and the induced one):

$$\mathbf{j} = \sigma(\mathbf{E} + \mathbf{v} \times \mathbf{B}), \quad (1.10)$$

where σ is the electrical conductivity.

Generalized Ohm's Law

The stratification of the solar interior and atmosphere adds an extra level of complexity to the system, requiring the use of a generalized form of Ohm's law. Assuming a plasma with number densities for electrons, ionized atoms, and neutral atoms, namely n_e , n_i , n_0 , Ohm's law can be expressed by the following complicated equation:

$$\begin{aligned} n_e e (\mathbf{E}_0 + \frac{\nabla p_e}{n_e e}) = & \frac{m_e}{e} \left(\frac{\partial \mathbf{j}}{\partial t} + \nabla \cdot (\mathbf{v} \mathbf{j} + \mathbf{j} \mathbf{v}) \right) \\ & + \left(\frac{1}{\Omega_e \tau_{ei}} + \frac{1}{\Omega_e \tau_{en}} \right) B \cdot \mathbf{j} + \mathbf{j} \times \mathbf{B} \\ & + \frac{\xi^2 \Omega_i \tau_{in}}{B} [\nabla p_e \times \mathbf{B} - (\mathbf{j} \times \mathbf{B}) \times \mathbf{B}]. \end{aligned} \quad (1.11)$$

where v is the mean velocity of the plasma, E_0 is the total electric field (initial plus induced), $\Omega_e = \frac{eB}{m_e}$ and $\Omega_i = \frac{eB}{m_p}$ are the gyration frequencies of electrons and ions, $\xi = \frac{n_0}{n_0 + n_e}$ is the neutral fraction, τ_{ei} is the electron-ion collision time, and τ_{en} , τ_{in} are the times for collisions between electrons and neutrals, and neutrals with ions, respectively (Priest 2014). Usually, ∇p_e , which is the electron pressure gradient, and the electron inertia on the Sun are small compared to other species, so they are negligible. Under these premises, Ohm's law yields the following simpler expression:

$$\mathbf{E}_0 = \frac{\mathbf{j}}{\sigma} + \frac{1}{n_e e} \mathbf{j} \times \mathbf{B} - \frac{\xi^2 \Omega_i \tau_{in}}{n_e e B} (\mathbf{j} \times \mathbf{B}) \times \mathbf{B}. \quad (1.12)$$

Induction Equation

Combining Ohm's law, Ampere's law, and Faraday's law to eliminate the electric

field and current density, we obtain an important equation governing the evolution of the magnetic field:

$$\frac{\partial \mathbf{B}}{\partial t} = -\nabla \times (-\mathbf{v} \times \mathbf{B} + \frac{\mathbf{j}}{\sigma}) \quad (1.13)$$

$$= \nabla \times (\mathbf{v} \times \mathbf{B}) - \nabla \times (\eta \nabla \times \mathbf{B}) \quad (1.14)$$

where η is the magnetic diffusivity, $\eta = \frac{1}{\sigma\mu_0}$. The induction equation consists of two terms: $\nabla \times (\mathbf{v} \times \mathbf{B})$, considered as magnetic advection, provides information on how the motion of the plasma flow affects the evolution of the magnetic field. The term $-\nabla \times (\eta \nabla \times \mathbf{B})$, considered as magnetic diffusion, describes how the dissipative nature of the plasma flow affects the magnetic field's evolution. It is important to assess in our observable system which term dominates. Assuming a plasma velocity scale and length scale v_0, L_0 , there is a dimensionless number called the Magnetic Reynolds number, $R_m = \frac{v_0 L_0}{\eta}$, that compares which of the above terms dominates. When this number is much less than one, it indicates that magnetic diffusivity is very large in this area, leading to the deduction that the magnetic diffusion term will dominate the induction equation. Thus, knowledge of which term dominates can lead to important conclusions about the evolution of the magnetic field.

The plasma motion affects the evolution of the magnetic field via the induction equation, and we obtain information about the current density through Ohm's law. However, the plasma motion is being constrained by two conservation laws (mass and energy) and the equivalent of the Navier-Stokes equation of motion defined for plasma.

Mass Continuity Equation

In a frame of reference moving with the plasma flow, the inflow of mass at every time is equal to the outflow, ensuring mass conservation.

$$\frac{D\rho}{Dt} = -\rho \nabla \cdot \mathbf{v} \quad (1.15)$$

The advection derivative is $\frac{D\phi}{Dt} = \frac{\partial\phi}{\partial t} + \mathbf{u} \cdot \nabla \phi$.

Equation of Motion

Assuming a system with moving plasma in the presence of a magnetic field, a grav-

itational field, and a viscous plasma flow, the motion of the plasma is governed by the following equation of motion:

$$\rho \frac{D\mathbf{v}}{Dt} = -\nabla p + \mathbf{j} \times \mathbf{B} + F_g + F_v, \quad (1.16)$$

where ∇p is the pressure gradient, $\mathbf{j} \times \mathbf{B}$ is the Lorentz force, F_g is the gravitational force from the gravitational field, and F_v is the force representing the effects of a viscous plasma flow:

$$F_g = -\rho g_{\odot} \hat{r}, \quad (1.17)$$

The gravitational acceleration on the Sun is $g_{\odot} = 274 \text{ m/s}^2$, while the viscous force has the following expression:

$$F_v = \rho v \left[\nabla^2 \mathbf{v} + \frac{1}{3} \nabla (\nabla \cdot \mathbf{v}) \right], \quad (1.18)$$

where v is the coefficient of kinematic viscosity, this term represents the isotropic viscosity.

Another important equation that is part of the set of MHD equations is the perfect gas law. Assuming a gas that consists of n number of particles, then the perfect gas law yields:

$$p = nk_B T, \quad (1.19)$$

where T is the mean temperature of the plasma, n is the number of the particles per m^3 , and k_B is the Boltzmann constant ($k_B = 1.381 \times 10^{-23} \text{ m}^2 \text{ kg s}^{-2} \text{ K}^{-1}$).

The last equation that completes the set of MHD equations is the one that depicts the conservation of energy:

$$\frac{\rho^{\gamma}}{\gamma - 1} \frac{D}{Dt} \left(\frac{p}{\rho^{\gamma}} \right) = -\nabla \cdot \mathbf{q} - L_r + \frac{\mathbf{j}^2}{\sigma} + F_H, \quad (1.20)$$

where $\gamma = \frac{5}{3}$ when the plasma consists of fully ionized hydrogen, $\nabla \cdot \mathbf{q}$ represents the heat flux with $\mathbf{q} = -\mathbf{k} \nabla T$, L_r represents the net radiation, $\frac{\mathbf{j}^2}{\sigma}$ is the Ohmic dissipation, and the last term represents additional heating from other sources e.g viscosity.

So, the complete set of MHD equations that governs the motion of a plasma in the presence of a magnetic field is the following:

$$\frac{\rho^\gamma}{\gamma - 1} \frac{D}{Dt} \left(\frac{p}{\rho\gamma} \right) = -\nabla \cdot \mathbf{q} - L_r + \frac{\mathbf{j}^2}{\sigma} + F_H, \quad (1.21)$$

$$p = nk_B T, \quad (1.22)$$

$$\rho \frac{D\mathbf{v}}{Dt} = -\nabla p + \mathbf{j} \times \mathbf{B} + F_g + F_v, \quad (1.23)$$

$$\frac{D\rho}{Dt} + \nabla \cdot (\rho\mathbf{v}) = 0, \quad (1.24)$$

$$\frac{D\mathbf{B}}{Dt} = \nabla \times (\mathbf{v} \times \mathbf{B}) - \nabla \times (\eta \nabla \times \mathbf{B}). \quad (1.25)$$

Chapter 2

The magnetic flux emergence process

The introductory section aimed to highlight key aspects of the Sun’s nature and the MHD equations that describe the behavior of the Sun’s plasma near magnetic fields. Observations have shown that the Sun’s magnetic field and flux change in an 22-year cycle, a phenomenon that remains a topic of interest in heliophysics (e.g. Beer (2000); Howe et al. (2005); Haigh (2007); Nandy (2011)).

In astrophysics, understanding celestial objects often involves analyzing the light they emit or absorb, including their molecular or atomic spectra. These analyses help us infer their structure and, using the Doppler effect, determine their motion relative to Earth.

The magnetic field is crucial in many astrophysical environments. Measuring it is challenging due to its complexity and limited measurement methods like the Zeeman effect and the Davis-Chandrasekhar method. However, the Sun’s proximity allows for more direct observation with satellites. This access enables detailed studies of the Sun’s magnetic field, including creating magnetograms to map its vertical component at the solar surface.

Figure 2.1, derived from the work of Jiang et al. (2019), incorporates observations from the Solar Dynamic Observatory (SDO) that contains a solar magnetogram as well as images from the 171 angstrom emission line . This figure vividly illustrates intense magnetic activity, marked by numerous magnetic structures, and the forma-

tion of a highly twisted sigmoidal structure preceding an explosive event.

Regions with such intense magnetic activity on the Sun are called Active Regions (ARs). Examining the magnetogram, we notice areas of white and black, representing the magnetic field's positive and negative maxima, respectively. ARs are key in producing solar phenomena with explosive characteristics, like solar flares, coronal jets, and coronal mass ejections (CMEs), which can impact technology and life on Earth.

These regions are crucial in the development of such events Parker (1955). The activity in ARs is strongly linked to the presence of a strong magnetic field. The emergence of the magnetic field into these areas leads to the formation of ARs, paving the way for the intense magnetic activity that triggers solar eruptive events (Shimizu et al., 1992; Berghmans & Clette, 1999; Kano et al., 2010). Therefore, the emergence of magnetic flux is a key factor in driving the Sun's dynamic activity.

2.0.1 The magnetic buoyancy and the magnetic flux tubes

The emergence of magnetic flux is a complex process that requires meticulous examination. To accurately investigate this phenomenon, it is necessary to connect the magnetic structure in the solar atmosphere to its origins within the solar interior. This connection is challenging, as the journey of the magnetic flux spans diverse regions with distinct environments. The theory of magnetic field enhancement in the tachocline has been addressed, but reconciling the observed solar loops with the presumed magnetic flux sheets is difficult. These sheets display complexities, rather than the expected spherical symmetry, which need further exploration.

In the tachocline, MHD instabilities cause these magnetic sheets to become unstable. The work by Cattaneo & Hughes (1988) used non-linear MHD simulations to examine a uniform magnetic field in a convectively stable atmosphere. They found that the magnetic field is susceptible to Rayleigh-Taylor (RT) instabilities, which lead to plasma flows with intense shearing velocities and activate secondary Kelvin-Helmholtz instabilities. This mechanism results in gas being intricately wrapped in areas dominated by intense vortices, causing the magnetic sheet to disintegrate into smaller fragments with cylindrical symmetry, known as magnetic flux tubes. A similar outcome has been found by (Fan, 2001a) as we display in Figure 2.2. In this

figure, there is initially a horizontal sheet of magnetic field that is stable against buoyancy instability. The magnetic field sheet is disturbed by adding a horizontal velocity field. After the velocity field is added, the magnetic field becomes unstable with respect to buoyancy instability (undular buoyancy instability). As a result, disturbances are formed that develop into arc-shaped magnetic flux tubes.

Magnetic flux tubes are unique structures where magnetic field lines converge into tubular configurations, surrounded by a region of relatively weaker magnetic fields. These tubes facilitate the transfer of magnetic flux across areas with different magnetic field intensities. Due to their heightened magnetic pressure and reduced density, these tubes are prone to buoyancy instabilities, causing them to ascend through the convection zone and give rise to various solar phenomena. This has been consistently reported in studies such as those by Matthews et al. (1995) and Fan (2001a).

Numerical simulations are important for understanding the process of magnetic flux emergence. By basing these simulations on plasma physics, MHD, and other relevant disciplines, and comparing the results with observational data, we gain comprehensive insights into this intricate solar process.

Within the context of Parker's magnetic buoyancy theory (Parker, 1955), we go deeper into the dynamics of these tubes under varying pressure conditions.

Considering the magnetic field within a flux tube, it has magnetic pressure $\frac{B^2}{2\mu}$, thus the equality of the pressure will be:

$$P_e = P_i + \frac{B^2}{2\mu} \quad (2.1)$$

The external pressure P_e of the flux tube relies on the internal pressure P_i and the magnetic field pressure $\frac{B^2}{2\mu}$, μ defined earlier. If we assume that the flux tube is in thermal equilibrium and the densities are ρ_e and ρ_i the 2.1 yields to the following

$$\begin{aligned} \frac{k_B T \rho_e}{m} &= \frac{k_B T \rho_i}{m} + \frac{B_i^2}{2\mu} \\ \Rightarrow \rho_e &= \rho_i + \frac{\mu_m B^2}{k_b T 2\mu_0} \implies \frac{\Delta\rho}{\rho} = \beta^{-1}; \end{aligned} \quad (2.2)$$

Thus $\rho_i < \rho_e$ therefore the flux tube will have less dense plasma inside compare to the density of the ambient environment. It will move like the bubble inside a water medium, it will try to move upwards and emerge, this is called magnetic buoyancy.

Now let us assume that the length of this tube is L and its crossection is D then the buoyancy force that acts on this flux tube will scale with the difference of the densities like that $LDg(\rho_e - \rho_i)$. As the flux tube emerging due to the buoyancy a magnetic tension is beeing acted on the magnetic field lines given by the following equation:

$$-\frac{1}{\mu_0}(\mathbf{B} \cdot \nabla)\mathbf{B} = \hat{W} \frac{d}{ds} \left(\frac{B^2}{2\mu_0} \right) + \hat{S} \left(\frac{B^2}{\mu_0 R} \right) \quad (2.3)$$

The magnetic pressure gradient term, $\hat{W} \frac{d}{ds} \left(\frac{B^2}{2\mu_0} \right)$, is associated with the gradient of magnetic pressure, given by $\frac{B^2}{2\mu_0}$. This gradient creates a force that pushes the magnetic field lines apart. In this term, \hat{W} is the unit vector tangent to the flux tube. The buoyancy term, $\hat{S} \left(\frac{B^2}{\mu_0 R} \right)$, represents a buoyancy-related force on the flux tube. Here, \hat{S} is the unit vector perpendicular to the flux tube, indicating the direction of the buoyancy force. The magnetic tension term, $-\frac{1}{\mu_0}(\mathbf{B} \cdot \nabla)\mathbf{B}$, represents the magnetic tension force. This force acts to straighten curved magnetic field lines. In this expression, \mathbf{B} is the magnetic field, and ∇ is the gradient. The dot product $(\mathbf{B} \cdot \nabla)\mathbf{B}$ describes how the magnetic field varies along its direction.

The magnetic tension acting on the magnetic field lines at this specific stage plays a important role in the evolution of the flux tube within the solar interior. When the flux tube begins to emerge and curves, it experiences a restoring force due to the tension at its boundaries. For the flux tube to continue emerging, the buoyancy force must exceed the magnetic tension, i.e., $(\rho_e - \rho_i)g > \frac{B^2}{\mu_0 L}$. Using relation (2.2), we can determine the minimum length the flux tube must possess to emerge through the solar interior:

$$L > \frac{2k_b T}{\mu_m g} \quad (2.4)$$

Assuming the pressure scale height is given by $H_p = \frac{k_b T}{m_p g}$, if the length of an flux tube is twice or more the pressure scale height, it will emerge through the convection zone. For this simplistic scenario to hold true, it's essential to assume that the buoyancy force dominates over the convective forces.

2.1 Numerical simulations

We discussed about the Sun's magnetic field, exploring how it forms into a flux tube and the necessary length it must attain to ascend through the convection zone. This understanding of buoyancy instability was encapsulated in a seminal paper by Parker in 1955 (Parker, 1955). Given the complexity of our laboratory settings – where we deal with environments characterized by convective motions, turbulence-dominated zones, and magnetically dominated regions – studying the magnetic flux emergence process becomes challenging. Typically, these simulations begin with a horizontal flux tube in radial force equilibrium that is susceptible to buoyancy instability. This state is achieved by altering various independent thermodynamic variables, such as density, temperature, and entropy.

The approach of maintaining equal entropy was employed by (Fan et al., 1994), where the initial toroidal ring was in mechanical equilibrium, albeit with a temperature differing from its surroundings. In contrast, the study by (Caligari et al., 1995) initialized with a toroidal ring that matched the ambient medium's density. This equilibrium was maintained by balancing the rotational force against the magnetic curvature force in the direction perpendicular to the rotational axis. As a result, the flux tube is cooler than its surroundings and rotates more rapidly.

The observed “Omega loops” in the Sun's atmosphere necessitate that the initial conditions for the horizontal flux tube possess a stronger buoyancy force at its centre compared to its edges. This ensures that the flux tube adopts the characteristic omega loop shape. Fan (Fan, 2001b) proposed an initial representation of the buoyant effect through the modeling of reduced density at the core of the flux tube. This reduction leads to an intensified buoyant force at the centre due to its diminished density, a phenomenon known as the “density deficit”. Mathematically,

this concept is expressed by:

$$\Delta\rho = \frac{\rho_1(r)}{\rho_0(z)} \exp\left(-\frac{r^2}{\lambda^2}\right)$$

In this expression, ρ represents the intrinsic density of the tube, while ρ_1 stands for the mean density inside the flux tube, ρ_0 stands for the density of the background. Moreover, λ characterizes a distance scale beyond which the tube is essentially field-free. Under this premise, the Gaussian decrement in density causes the centre of the flux tube to ascend more rapidly, leading to the emergence of an Ω -loop. This approach has been widely adopted in simulations for its simplicity and provides a comparative framework due to the diversity of variables that can be contrasted between different models.

An important characteristic of a flux tube is the twist in their magnetic field lines around the central axis. Flux tube, located within the Sun's turbulent convection zone, are influenced by a complex interplay of forces, including magnetic tension, buoyancy, and the Coriolis force. Among the key factors affecting the behavior of these tubes is their twist. The presence or absence of a twist in these flux tubes impacts their stability and dynamics, making it more than just a geometrical aspect.

An untwisted magnetic flux tube is much like a delicate thread in a storm. Without the stabilizing effect of a twist, these tubes are highly prone to magnetic buoyancy instability. In such cases, the less dense, magnetized regions within the tube have a strong tendency to rise, often leading to disorganized and individual ascents, resulting in fragmentation.

Moreover, the Kelvin-Helmholtz instability, prevalent in environments with velocity shears, can impact untwisted flux tubes. As these tubes navigate through the convection zone, turbulent motions and differential rotation create velocity variations across the tube. Without the stabilizing influence of a twist, these variations can lead the flux tube to form vortex structures, compromising its coherence.

However, the introduction of a twist into these flux tubes dramatically changes their dynamics. The twist provides structural strength, helping the tube counteract the destabilizing effects of buoyancy and shear instabilities. In the turbulent convection zone, a twisted flux tube is more resistant to deformation, maintaining its structure and longevity. Research by Emonet & Moreno-Insertis (1998) involved

simulations with flux tubes of varying twist levels. They discovered that highly twisted tubes did not suffer the magnetic flux degradation and fragmentation into two vortices seen in tubes with less twist. Their high-twist findings are depicted in figure 2.3, which is Figure 9 in their paper, displaying the y-component of the vorticity vector at different simulation times. This figure demonstrates the stability of the flux tube and the presence of two vortices with distinct rotational directions at its tail. However, a very high twist can render the flux tube kink unstable, presenting challenges for its evolution.

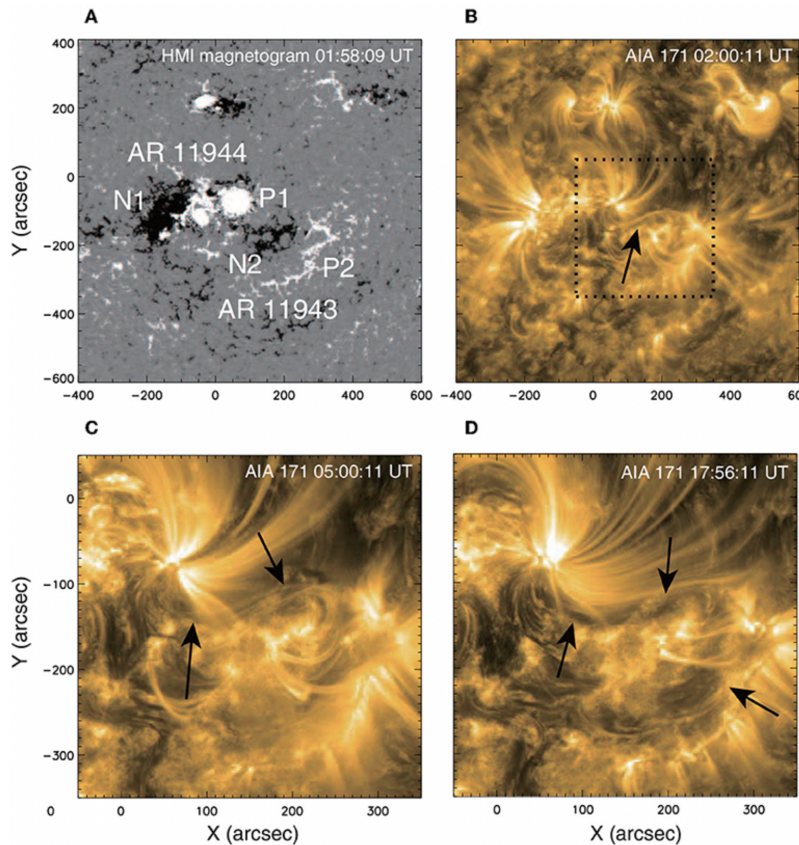


Figure 2.1: (A) The SDO/HMI magnetogram displays the arrangement of magnetic polarities near the flare site. The main polarities, N1 and P1, form AR 11944, while N2 and P2 make up AR 11943. The flare primarily involved polarities P1 and N2. (B) The SDO/AIA image at 171 Å shows the same region as in (A), with a sigmoidal coronal loop at the flare site indicated by an arrow. (C) A zoomed-in view highlights the sigmoid and a filament, marked by arrows. (D) The filament channels are shown here, as highlighted by the arrows.

Magara & Longcope (2001) were among the first to conduct a magnetic flux emergence experiment using a horizontally twisted Flux Tube (TFT) at the upper convection zone. They applied the density deficit method to induce buoyancy.

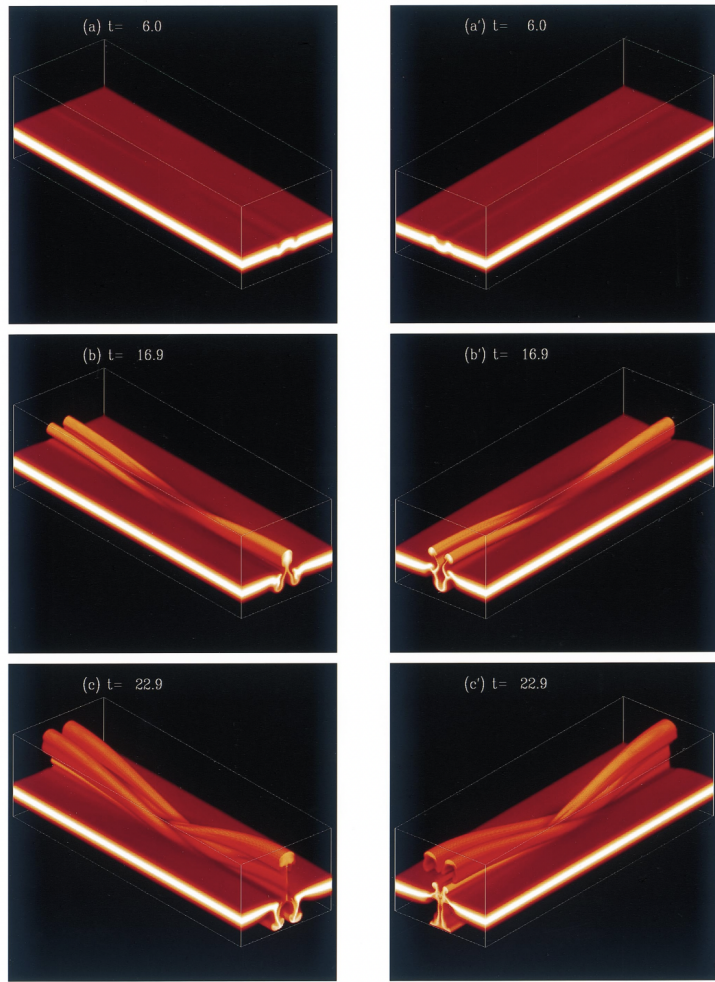


Figure 2.2: The formation of a magnetic flux tube through the disruption of a horizontal sheet of magnetic field. The figures depict the magnetic field strength $|B|$.

Their 2.5D numerical simulations featured a highly stratified atmosphere, mirroring the convection zone's temperature evolution as described by Stix (1991). The setup included an isothermal layer for the photosphere, a transition region, and a high-temperature, field-free isothermal corona. Initially, the magnetic tube rose through the convection zone due to magnetic buoyancy, progressing towards the photosphere. As it emerged, the tube expanded horizontally because its magnetic pressure exceeded that of the surrounding environment. Upon reaching the cooler photosphere, the tube's ascent slowed, and it became compressed, creating an interface with the lower atmosphere. This interface experienced Rayleigh-Taylor instability, caused by denser plasma overlying lighter, magnetically-rich plasma, propelling

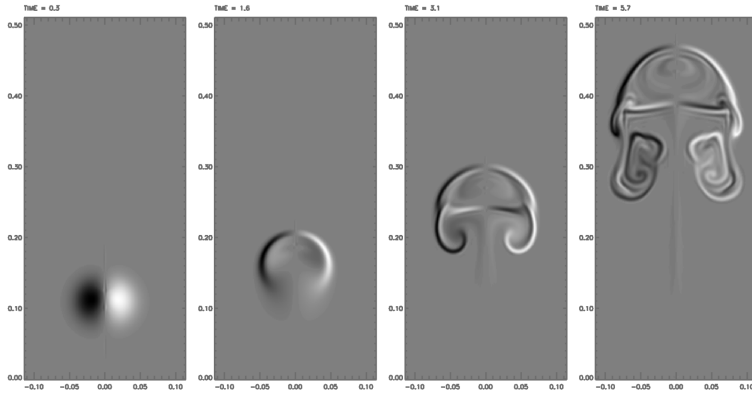


Figure 2.3: The y-component of the vorticity vector at different times of the simulation. This is the case with the high twist in the paper by (Emonet & Moreno-Insertis, 1998)(Figure 9).

the tube through the photosphere. As the tube emerged above the photosphere, it expanded due to decreasing atmospheric gas pressure, yet its main axis remained anchored near or just below the photosphere. These dynamics are depicted in figure 2.4, Figure 2 of Magara & Longcope (2001), showing the tube's cross-section evolution over time, with filled contours for gas density, white contours for magnetic field lines, and arrows for the velocity field.

A subsequent study by Toriumi & Yokoyama (2011) used 2D simulations in a stratified atmosphere akin to Magara & Longcope (2001). They positioned their TFT deep in the convection zone, about 20×10^3 km from the Sun's surface, with a strong magnetic field of $B = 15 \times 10^4$ G and a large radius. Despite initial buoyancy, the tube's evolution within the convection zone paralleled Emonet & Moreno-Insertis (1998)'s findings. In the solar atmosphere, its behavior was similar to Magara & Longcope (2001)'s results. A distinctive aspect of Toriumi & Yokoyama (2011)'s approach was the inclusion of a convectively stable photosphere, which led to the tube slowing down at a considerably greater depth than observed in Magara & Longcope (2001), indicating a potential different underlying mechanism.

In their study, Archontis et al. (2004) conducted 3D resistive MHD simulations in a highly stratified solar atmosphere, divided into two isothermal layers representing the lower atmosphere and the corona, and a transitional region of notable temperature change. A horizontal TFT was placed in the upper convection zone.

The tube's upward movement through the convection zone was primarily driven

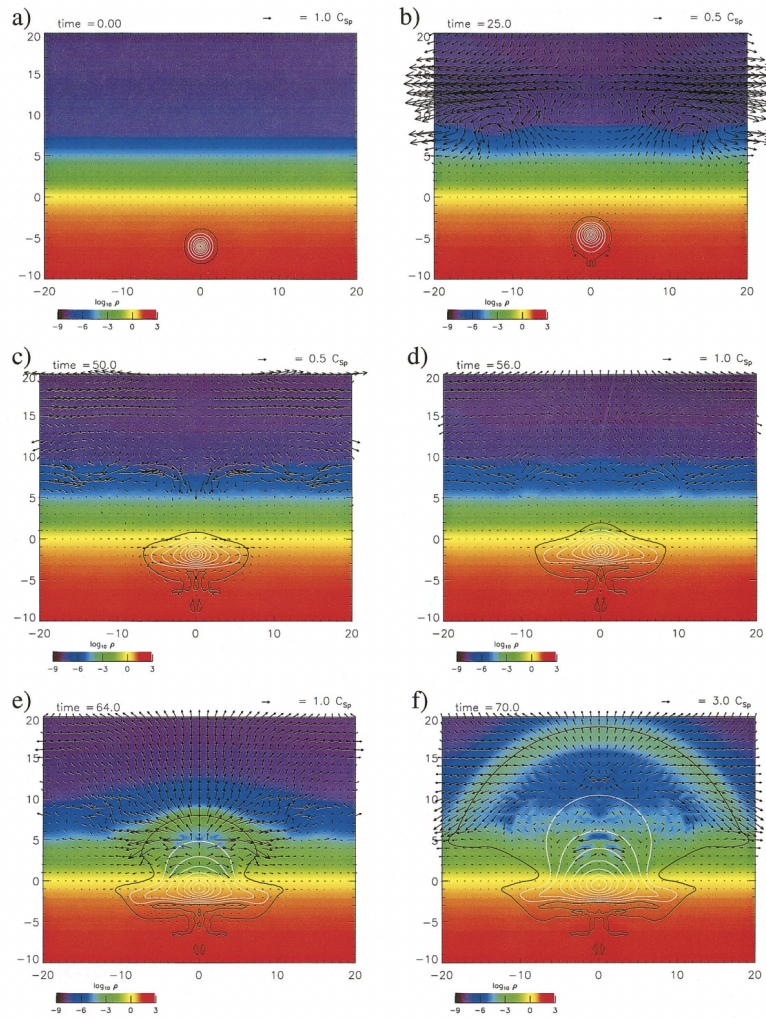


Figure 2.4: Figure 2 in the paper by (Magara & Longcope, 2001) display the temporal evolution of the crossection of the twisted flux tube. The filled contours corresponds to the gas density, the white contours are the magnetic field lines and the arrows correspond to the velocity field.

by buoyancy due to a density deficit, with drag from the surrounding environment acting as a counterforce. The Lorentz force had minimal impact at this stage due to little bending of the tube's axis. Cross-section observations of the tube showed patterns similar to those in Emonet & Moreno-Insertis (1998). The tube experienced minimal stretching as it ascended to the photosphere. The axial field strength decreased in accordance with the principle of magnetic flux conservation: $B_y(z) = B_y(z_0) \frac{\rho(z)}{\rho(z_0)}$.

The centre of the tube, being more buoyant, showed an increase in the azimuthal

field at the front and a decrease at the back. As the tube neared the photosphere, all field components diminished due to the tube's expansion. The decrease in azimuthal components was slower compared to axial ones, resulting in an increased field line pitch.

The ascent of the tube also generated a compression wave, initially mild in the convection zone but intensifying into a shock wave in the lower atmosphere. In the isothermal lower atmosphere, the post-shock speed followed an exponential decay pattern due to decreasing density. This pattern altered in the transition region, with the speed initially slowing down, then reducing, influenced by varying temperatures. Upon entering the corona, these changes became more gradual.

The main highlight of this study was the emergence of the TFT into the solar atmosphere. As the tube rose from the convection zone, it underwent changes in speed, expansion, and density. Upon reaching the photosphere, it faced challenges due to different expansion rates in vertical and horizontal directions, showing horizontal expansion. The emergence was also influenced by isothermal stratification in the lower atmosphere and buoyancy instability above the photosphere, essential for the tube's successful emergence into the corona. A pivotal criterion introduced in this work is the following inequality:

$$-H_p \frac{\partial(\log B)}{\partial z} \geq -\frac{\gamma}{2} \beta \delta + \tilde{k}_\parallel^2 \left(1 + \frac{\tilde{k}_\perp^2}{\tilde{k}_z^2} \right) \quad (2.5)$$

which the tube must satisfy to ensure its emergence. The derivation of this equation is based on the stability conditions of a rising magnetic flux tube in the solar atmosphere. It specifically addresses the buoyancy instability that occurs when the magnetic field decreases with height, which reduces the stabilizing gas pressure gradient. The equation is derived from the magnetic Rayleigh-Taylor instability criterion, which describes how a top-heavy magnetic field configuration can become unstable. The derivation incorporates the effects of both the magnetic and gas pressures, represented by the ratio β (the ratio of gas pressure to magnetic pressure), and the superadiabatic excess δ . The wavenumbers k_\parallel and k_\perp describe the perturbations parallel and perpendicular to the magnetic field lines. When the destabilizing effect of the magnetic pressure gradient outweighs the stabilizing effect of the gas pressure gradient, the buoyancy instability sets in, allowing the magnetic flux tube to rise further into the atmosphere. This condition essentially acts as a gatekeeper,

dictating whether the tube can successfully emerge into the solar atmosphere. This inequality essentially expresses the buoyancy instability that Acheson first introduced in the paper Acheson (1979) in the parameters that easily been used in all the simulations. H_p is the pressure scale height given by $H_p \geq (\frac{\partial \ln p}{\partial z})^{-1}$, δ is the superadiabatic excess

$$\delta = \nabla - \nabla_{ad}$$

in this context ∇ is the logarithmic temperature gradient and ∇_{ad} is its adiabatic value, the \tilde{k}_\perp and \tilde{k}_\parallel are the wavenumber of the perturbations that take place parallel to or perpendicular to the magnetic field. The term on the left-hand side of the equation signifies the effect of instability caused by the decreasing value of B with altitude, particularly in the tube's apex. In their study, Archontis et al. (2004) focused on the influence of the $\beta\delta$ term, crucial in solar stratification. For isothermal stratification, δ is -0.4, leading to stabilization. However, this stabilizing effect diminishes as β decreases, occurring when magnetic pressure overtakes gas pressure during the tube's transition across the photosphere. As the tube approaches the photosphere, its leading layers exhibit a lower value on the left-hand side of the inequality compared to the right-hand side's stratification term. With a decreasing plasma β , the ratio eventually drops below 1, triggering buoyancy instability that propels the magnetized plasma towards the corona.

Studies using stratified atmospheres with horizontal TFT have revealed several key insights:

1. A heightened density deficit at the tube's core increases buoyancy, leading to the formation of an Omega loop shape.
2. The tube's emergence initially causes a compression wave, which becomes a shockwave in the lower atmosphere.
3. Near the solar surface, horizontal expansion due to magnetic pressure ceases when gas pressure becomes dominant, forming a boundary layer where magnetic flux accumulates.
4. The tube's movement through the solar atmosphere is influenced by criteria from Acheson (1979); Archontis et al. (2004), involving expansive motion driven by magnetic pressure.

2.1.1 Solar eruptions and solar jets

The Sun's activities, especially solar eruptions, significantly impact Earth. These events in the Sun's atmosphere are closely related to magnetic flux emergence. In Figure 2.1, an active region before a solar flare displays a twisted, sigmoidal structure, prompting studies to understand the connection between these formations and magnetic flux emergence. Simplified models, such as a field-free corona, are important for comprehensively understanding magnetic flux emergence and its role to solar eruptive events.

Syntelis et al. (2017) conducted 3D resistive MHD simulations with a horizontal TFT in the upper convection zone, using the density deficit approach from Fan (2001a). Their study clarified the mechanisms driving solar eruptions. As the tube reached the solar surface, it displayed two opposing polarities that gradually diverged. The apex, moving toward the atmosphere, formed a PIL between these polarities, leading to shearing and converging motions. This created a current sheet, triggering magnetic reconnection and forming a shear arcade structure. Over time, a twisted magnetic flux rope (FR) developed. The expanding field above the FR, the envelope field, weakened, causing torus instability in the FR and leading to further reconnection above the PIL through tether cutting. This generated a fast reconnection jet, driving the FR forward with increased momentum. However, the magnetic tension of the envelope field was insufficient to contain the erupting FR, leading to its ejection.

This eruption mechanism involves torus instability and tether cutting reconnection. Internal reconnection is critical for the FR to overcome the magnetic tension of the envelope field for successful ejection. Initial and boundary conditions are key in these experiments. Many studies with an unmagnetized corona led to confined eruptions due to the inability of the FRs to counteract magnetic tension Leake et al. (2022). However, studies like (Fan, 2009; Archontis & Török, 2008) observed explosive solar eruptions in a field-free corona, emphasizing the importance of magnetic flux emergence.

Experiments in a magnetized corona provide unique perspectives on solar eruptions. Archontis & Hood (2012) found that the amount of twist in a coronal flux rope affects the ascent of dense plasma post-eruption. If the ambient coronal field is stronger than the erupting field, the flux rope may deform and prevent eruption.

In contrast, an oppositely oriented coronal field can lead to significant ejective eruptions, while a parallel field might result in confined eruptions due to inadequate reconnection.

Archontis et al. (2013) performed 3D MHD simulations on jets in emerging flux regions. Their study revealed that external reconnection between the emerging and ambient fields produces standard reconnection jets. As the flux rope ascends, it displaces the surrounding field, creating jets from both external and internal reconnections. This results in a “blowout” jet that combines cooler plasma from the erupting core with hotter jets, exhibiting an untwisting trajectory as it ascends.

Moreno-Insertis & Galsgaard (2013) conducted 3D MHD simulations in a stratified atmosphere with a horizontal buoyant TFT and a unipolar ambient magnetic field. Their findings on solar jets and eruptions closely match recent observational studies. The plasma temperature and density, jet velocities, and dimensions align with Shimojo & Shibata (2000) and Savcheva et al. (2007), though jet lifetimes were longer.

The study also explores blowout jets, as documented by Moore et al. (2010a), where some jet events exhibit eruptive patterns alongside ejection. The simulations replicate various eruptive phenomena, including tether-cutting reconnection and secondary twisted flux-rope ejection, potentially due to kink or torus instabilities. The eruptions transition from high-velocity to more chaotic patterns, demonstrating a connection between theoretical simulations and observational data in understanding solar phenomena related to magnetic flux emergence.

The aforementioned studies concentrated on strong coronal jets arising from effective magnetic reconnection, influenced by the alignment of the emerged flux system with the ambient magnetic field. Antiparallel orientation between these systems increases the likelihood of generating strong coronal jets or CMEs. Conversely, surges are transient events characterized by lower velocities (approximately 10 – 20 km/s), filamentary structures, and chromospheric origins.

In his 2015 study, MacTaggart et al. (2015) carried out 3D resistive MHD simulations, developing three distinct models. These models employed an Emerging Flux Region (EFR) closely parallel to the ambient horizontal field, deliberately designed to inhibit the formation of strong coronal jets and favor surge generation. The research found a pronounced link between the occurrence of surges and magnetic

reconnection within the systems. Reconnection was categorized into four distinct phases, with each phase corresponding to the initiation of surges. The second model produced surges akin to the first, albeit with a reduced magnitude of the EFR. The third model, featuring a different ambient field geometry, aimed to replicate Guglielmino et al. (2010) findings, where surges were observed to flow away from a sunspot. This simulation successfully reproduced the preferred direction of surges away from the EFR.

To conclude, these models effectively generated surges that mirrored typical speeds seen in solar observations, exhibited the characteristic filamentary density structure, underscored their linkage to various reconnection events, and examined the impact of the ambient magnetic field's configuration on the direction of surges.

2.2 Partial ionization

All these numerical simulations provided a great amount of knowledge in the scientific community regarding the magnetic flux emergence process and the subsequent interplay that the emerging flux system is having with the ambient coronal field and its role on the solar eruptive phenomena. All these studies were conducted using a plasma constituted by atomic Hydrogen. Some of the simulations also used heat conduction which created a more realistic the process of the transfer of heating flow through the magnetic field lines. The Sun is composed of approximately 75% hydrogen by mass, aligning closely with real-world measurements. Simulations that mimic the Sun's actual conditions serve as a virtual laboratory, allowing for the refinement of theoretical models in solar physics. This synergy between theory and simulation enhances our understanding of solar phenomena, especially where direct observation is hampered by the Sun's intense brightness or the minuteness of certain events. High-fidelity simulations are indispensable, filling the gap between observable solar events and their underlying physics, thus aiding in the interpretation of observational data. Accurate simulations are vital for reliable space weather forecasts, critical for protecting both space-based and terrestrial technological systems.

Plasma, often described as the fourth state of matter, is distinct due to its ionized properties. Unlike the predominantly electrically neutral atoms and molecules in solids, liquids, and gases, plasmas are characterized by a significant proportion

of ionized particles. This ionization, entailing the removal of electrons, leads to the coexistence of free electrons and positively charged ions. Temperature is a determinant of a plasma's ionization state. In various astrophysical and laboratory settings, gases exhibit “partial ionization”, not being fully ionized. This is a key aspect in diverse environments such as the cores of neutron stars, molecular clouds crucial to star formation, and the Sun. The ionization degree in these systems hinges on plasma conditions like temperature, pressure, and density, with insights into these parameters derived from both theoretical models and observational data.

2.2.1 Models that determine the environmental profile of the Sun.

Understanding the internal stratification of the Sun, is important in solar physics. The standard solar model provides a foundational framework for the Sun’s internal structure and dynamics. Governed by the hydrostatic equilibrium equation, $\frac{dP}{dr} = -\rho g$, this model delineates how pressure, P , varies with depth against density, ρ , and gravitational acceleration, g and r is the radius. The energy transport equation distinguishes regions of radiative and convective transport. Within convective domains, the onset of convective instability is marked by the Schwarzschild criterion, $\nabla_{\text{rad}} > \nabla_{\text{ad}}$. Complementing these theoretical constructs, helioseismology offers a means to probe the Sun’s interior by examining its oscillation modes, providing constraints on internal sound speed profiles and other structural parameters. Stix’s contributions, particularly his 2004 work Stix (2004), have been important in advancing our understanding of solar oscillations and their implications for the Sun’s internal structures. Stix’s theoretical model has enhanced our understanding of the Sun’s optically thick interior. A priori, assessing the dimensions of the convection and radiative zones is challenging due to this opacity. Within the Sun’s interior, the mean free path of a photon is so small that the regions where photons are emitted and absorbed are essentially at the same temperature. Consequently, these areas satisfy local thermodynamic equilibrium (LTE). Stix’s model provides insights into the approximate temperature gradient within the convection zone. Drawing from the findings by Perez et al. (2009), we know that hydrogen is nearly 90% ionized at the top of the convection zone. Further, the adiabatic component of the temperature gradient becomes negligible about 1 Mm beneath the Sun’s surface. Armed with this information, we infer that the Sun’s upper convection zone allows for the

presence of neutral atoms. These atoms could influence energy transport dynamics or introduce other effects. It's important to differentiate between the solar atmosphere and the solar convection zone. The solar atmosphere, which is optically thin, means that photons can escape relatively freely without being scattered or absorbed multiple times. This characteristic implies that it doesn't satisfy LTE (Local Thermodynamic Equilibrium), necessitating a distinct approach to deduce the properties of the solar atmosphere.

An important model that tries to give us clues about the intricate structure of the solar atmosphere is the Val-C model Vernazza et al. (1981). Using Skylab's observations of the quiet Sun in the 40-140 nm EUV range, the study shows the detailed structure of the chromosphere. The team created different chromospheric models for six brightness levels, from a dim cell centre to a very bright network element. They did this by solving equations for non-LTE radiative transfer, statistical equilibrium, and hydrostatic equilibrium to find the best temperature-density distribution that matched the observed spectra. Their detailed hydrogen atomic model includes eight distinct levels, plus levels 9-12. The model also considers partial frequency redistribution effects. While they matched observed and calculated intensities in certain ranges, the temperature minimum they found differs from other observations. The study's analysis of radiative cooling rates highlights the dominance of the Ly-alpha ($L\alpha$) cooling rate in the transition region. This refers to the cooling effect caused by the Ly-alpha emission, which is a significant radiative transition in hydrogen atoms. This transition allows hydrogen atoms to release energy and cool the plasma effectively. Additionally, the Balmer continuum plays an important role in the chromosphere. The research carefully compares its findings with other models and provides detailed information on atomic data, observational data, model calculations, model properties, and a thorough examination of the temperature minimum and energy balance.

Avrett & Loeser (2008) introduce a detailed one-dimensional, time-independent model of the average quiet-Sun chromosphere and transition region. This model includes complex non-LTE radiative transfer calculations for various elements like H, C i-iv, and O i-vi. It is based on the SUMER atlas of the extreme ultraviolet spectrum by Curdt et al. (2001). The chromospheric model is semi-empirical, with the temperature distribution adjusted to match observed and predicted continuum intensities, line profiles, and intensities closely. The transition region model

is theoretical, balancing radiative losses and energy flowing from the corona, including thermal conduction and particle diffusion. This model improves on the earlier Model C by Vernazza et al. (1981), featuring a more accurate transition region, refined photospheric base, and more chromospheric observations.

Despite minor differences between observed and calculated lines, the agreement is very good, considering uncertainties in atomic rates and cross sections. The temperature distribution from (Stix, 2004; Avrett & Loeser, 2008) allows neutral atoms in the upper convection zone, photosphere, and chromosphere. Therefore, we expect that partially ionized plasma in these regions will affect the dynamics and thermodynamics of the plasma and may also impact the magnetic fields emerging from the Sun’s interior.

From these models, we conclude that the upper convection zone, photosphere, and chromosphere are regions where plasma may exist in a partially ionized state. The presence of neutral particles in these layers likely plays a significant role in shaping plasma behavior and its interactions with magnetic fields. By incorporating the effects of partial ionization into our numerical simulations, we gain valuable insights into how this aspect of plasma physics influences the process of magnetic flux emergence.

The solar community has recognized the importance of partial ionization, and efforts have been made to include this factor in numerical experiments. These simulations aim to more accurately replicate the conditions in the Sun’s outer layers, where the interplay between neutrals and ions is a significant component of the overall dynamics.

Improving our simulations to include partial ionization enhances our understanding of the magnetic flux emergence process and solar physics. This refinement leads to more accurate representations of the Sun’s activities by elucidating the complex mechanisms involved. Leake & Arber (2006) performed 2.5D MHD simulations, considering the role of neutrals in the solar atmosphere and employing a generalized Ohm’s law for a fluid with three components, based on the model by Braginskii (1965), while excluding pressure and Hall terms. Their studies revealed an increased rate of magnetic flux emergence and a higher diffusivity of the emerging magnetic field. They found currents reaching the corona aligned with the magnetic field due to perpendicular resistivity caused by ion-neutral collisions, leading to a force-free

coronal magnetic field. This initial inclusion of partial ionization suggested that neutrals affect the magnetic field's dynamics with solar plasma.

The earlier model of Leake & Arber (2006) utilized a simple equation of state without considering ionization-recombination dynamics. This was expanded to 3D by Arber et al. (2007), who confirmed the initial findings and noted that perpendicular resistivity reduced currents and that partial ionization led to less chromospheric material moving into the corona.

Leake & Linton (2013) further updated their model (2.5D) to include ionization-recombination effects. They simulated the ascent of magnetic flux tubes of various sizes and initial flux values, showing that these effects slowed the tubes' rise and limited their peak height. The partially ionized experiments showed tubes carrying up to 89% less material upwards. A major finding was that adding ionization-recombination resulted in less magnetic free energy in the corona, making the formation and eruption of unstable coronal structures less likely.

More recent and more sophisticated 2.5D numerical simulations of magnetic flux emergence were carried out from Nóbrega-Siverio et al. (2020). They used the Bifrost radiation-magnetohydrodynamic code, which models the magnetic flux emergence from the convection zone to the corona, including non-equilibrium (NEQ) effects on atomic hydrogen and H₂ molecules, as well as ambipolar diffusion.

The study specifically explores the rise of magnetized plasma through the solar atmosphere, focusing on the chromosphere, where the plasma exhibits non-local thermodynamic equilibrium and partial ionization. The research aims to assess the impact of NEQ ionization and recombination of hydrogen, molecule formation, and the role of ambipolar diffusion on the dynamics and thermodynamics of the flux emergence process. They found that ambipolar diffusion is shown to be less influential on the total unsigned emerged magnetic flux but plays a key role in heating the plasma via shocks within the emerged region.

The studies previously conducted were important in enhancing our comprehension of the simulation of partially ionized plasma within the Sun and its influence on the magnetic flux emergence process. However, a majority of these investigations were confined to 2.5D simulations, with the sole 3D study by (Arber et al., 2007) omitting the effects of ionization and recombination of neutral hydrogen. This thesis will try to fill this void and carry 3D numerical simulations including the effects of

the ionization and recombination of neutral atoms in the equation of state. This is to be done without the inclusion of heat conduction or comprehensive radiative transfer, enabling us to discern the intrinsic effects of partially ionized plasma on the magnetic flux emergence process. Once these effects are understood, more intricate physical processes can be added in the future, thus allowing for a clear identification of specific phenomena to partial ionization. Consequently, the objective of this thesis is to incorporate the effects of partial ionization into a 3D magnetic flux emergence experiment. The aim is to investigate its impact on the overall process and to scrutinize its role in the genesis of solar eruptions and on the dynamics of solar jets.

Chapter 3

Effects of partial ionization on the magnetic flux emergence in the Sun.

The emergence of the Sun’s magnetic flux is important, driving many solar events like the formation of active regions, flares, jets, and eruptions. Historically, this process has seen extensive research through 3D MHD numerical simulations (e.g Moreno-Insertis & Emonet (1996); Magara & Longcope (2001); Fan (2001b); Manchester et al. (2004); Archontis et al. (2004)).

3.1 Our Model

3.1.1 The Lare3D code

The Lare3D (Arber et al., 2001) is a computational code designed for simulating three-dimensional MHD phenomena. It utilizes the resistive MHD equations to model the behavior of conducting fluids in the presence of magnetic fields. The Lare3D, employs the Lagrangian remapping method, it involves a two-step process that splits the computational time step to handle the fluid dynamics effectively. Initially, during the Lagrangian phase, the code computes the fluid flow by moving the grid with the fluid, allowing it to accurately track the motion and deformation of

fluid elements. After this, an Eulerian remap phase takes place, where the computed properties are mapped back onto a fixed grid, correcting for any distortions that occurred during the Lagrangian step. This process, repeated at each time step, ensures both the accuracy of fluid advection and the stability of the computational mesh over time.

At the core of Lare3D’s numerical approach is a second order predictor-corrector scheme, which iteratively forecasts and refines the simulation’s state to ensure adherence to physical laws. The predictor phase estimates future states of the plasma and magnetic fields, while the corrector phase adjusts these predictions to satisfy the MHD equations, particularly the divergence-free condition of the magnetic field.

The code has a staggered grid, a staggered grid is a computational mesh layout where different variables are stored at distinct locations within each grid cell. In such a grid, scalar variables like pressure and density are located at the cell centres, while vector components such as velocities and magnetic field components are positioned at the cell faces or edges. In Lare3D specifically the magnetic field is evaluated at cell faces and the components of the velocity field at the cell corners like in figure 3.1. This arrangement helps to improve the numerical accuracy of derivatives and fluxes calculated in the simulation and is particularly effective in maintaining the divergence-free condition for vector fields, like the magnetic field in MHD simulations.

Lare3D employs artificial viscosity, a numerical technique designed to stabilize the simulation and capture the sharp discontinuities associated with shocks. This approach works by smoothing out steep gradients in the flow variables, which effectively spreads the shock over several grid cells and prevents non-physical oscillations. By carefully balancing the amount of artificial viscosity, Lare3D can accurately represent shock waves without sacrificing the overall fidelity of the simulation of high-speed fluid dynamics. This characteristic enhances the code to be a great tool of capturing shocks considering that most of the available codes encounter issues.

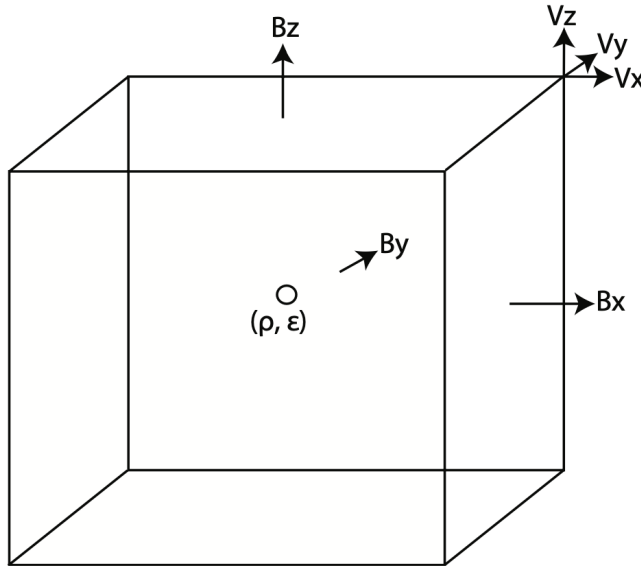


Figure 3.1: The evaluation of the variables in the Lare3D’s stagger grid (credit Larexd manual)

3.1.2 Equations

We numerically solve the 3D time-dependent, compressible, resistive MHD equations in Cartesian geometry using the Lare3D code. In order to include the effects of partial ionization to our experiment we modified the MHD equations (neglecting Hall term).

We assume populations of ions (i), neutrals (n) and electrons (e). Therefore, the total mass density (ρ), gas pressure (P) and specific energy (ϵ) are obtained by summing over the three species. For instance, $\rho = \sum_k m_k n_k$, where $k = i, e, n$ and m_k and n_k are the mass and number density of the species k .

The resulting MHD equations solved are:

$$\frac{D\rho}{Dt} = -\rho \nabla \cdot \mathbf{v}, \quad (3.1)$$

$$\rho \frac{D\mathbf{v}}{Dt} = -\nabla P + \mathbf{j} \times \mathbf{B} - g_0 \hat{\mathbf{z}} + \mathbf{S}_{visc}, \quad (3.2)$$

$$\frac{D\mathbf{B}}{Dt} = -\mathbf{B} (\nabla \cdot \mathbf{v}) + (\mathbf{B} \cdot \nabla) \mathbf{v} - \nabla \times [\eta \mathbf{j}_{||} + (\eta + \eta_{\perp}) \mathbf{j}_{\perp}], \quad (3.3)$$

$$\rho \frac{D\epsilon}{Dt} = -P\nabla \cdot \mathbf{v} + \eta j_{\parallel}^2 + (\eta + \eta_{\perp})j_{\perp}^2 + Q_{visc}, \quad (3.4)$$

where \mathbf{v} , \mathbf{B} , ρ , P are namely the velocity vector, magnetic field vector, density and gas pressure.

Gravity is $g_0 = 274 \text{ m s}^{-1}$. Viscosity is added through $\mathbf{S}_{visc} = \frac{\partial \sigma_{ij}}{\partial x_j} \hat{\mathbf{e}}_i$ and $Q_{visc} = \varepsilon_{ij}\sigma_{ij}$, where $\sigma_{ij} = 2\nu(\varepsilon_{ij} - \frac{1}{3}\delta_{ij}\nabla \cdot \mathbf{v})$ and $\varepsilon_{ij} = \frac{1}{2}\left(\frac{\partial v_i}{\partial x_j} + \frac{\partial v_j}{\partial x_i}\right)$, and $\nu = 622 \text{ kg m}^{-1} \text{ s}^{-1}$ (10^{-2} in non-dimensional units). In a magnetized plasma, viscosity behaves differently compared to neutral fluids due to the influence of magnetic fields. This viscosity can be anisotropic, meaning that the plasma exhibits different viscous responses depending on the orientation of motion relative to the magnetic field. Specifically, the velocity difference between particles can be affected by the alignment of their motion with the magnetic field lines. The current density is treated using its components parallel (\mathbf{j}_{\parallel}) and perpendicular (\mathbf{j}_{\perp}) to the magnetic field vector. These are defined as

$$\mathbf{j}_{\parallel} = \frac{(\mathbf{j} \cdot \mathbf{B})\mathbf{B}}{B^2} \quad \text{and} \quad \mathbf{j}_{\perp} = \frac{\mathbf{B} \times (\mathbf{j} \times \mathbf{B})}{B^2}, \quad (3.5)$$

where $\mathbf{j} = \frac{1}{\mu_0}\nabla \times \mathbf{B}$ is the full current density vector.

In modeling the interactions between charged particles and neutrals, we consider the collisional frequencies, which account for the momentum transfer between species. These frequencies are important for understanding the dynamics in partially ionized plasmas. The effective collisional frequency between a charged particle of type k and a neutral particle of type l , denoted as ν'_{kl} , can be represented as a function of their masses m_k and m_l , and their relative velocity v_{kl} :

$$\nu'_{kl} = \frac{m_l}{m_l + m_k} \nu_{kl} \quad (3.6)$$

This equation follows from the momentum exchange principle, where k can be an electron or an ion, and l is a neutral atom. The collisional frequencies between ions and neutrals (ν_{in}) and electrons and neutrals (ν_{en}) can be estimated using expressions derived from kinetic theory Spitzer (1962), taking into account the mass of ions (m_i) and electrons (m_e), the neutral density n_n , and the temperature-dependent cross-sections Σ_{in} and Σ_{en} :

$$\nu_{in} = n_n \sqrt{\frac{8k_B T}{\pi m_{in}}} \Sigma_{in} \quad (3.7)$$

$$\nu_{en} = n_n \sqrt{\frac{8k_B T}{\pi m_{en}}} \Sigma_{en} \quad (3.8)$$

Here, m_{in} and m_{en} are the reduced masses for the ion-neutral and electron-neutral pairs, respectively, and k_B is the Boltzmann constant. The reduced mass, μ , for a two-particle system with masses m_1 and m_2 is defined as $\mu = \frac{m_1 m_2}{m_1 + m_2}$. In this context, m_{in} and m_{en} represent the reduced masses of the ion-neutral and electron-neutral pairs, accounting for their relative contributions in interactions. $\Sigma_{in} = 5 \times 10^{-19} \text{ m}^2$ and $\Sigma_{en} = 10^{-19} \text{ m}^2$ are the ion-neutral and electron-neutral cross-sections, respectively. The effective collision frequency of electrons with ions ν_{ei} , representing the rate of momentum transfer, is derived considering the charged particle densities, their relative velocities, and cross-sectional areas, guided by Coulomb's law:

$$\nu_{ei} = 5.89 \times 10^{-24} \frac{n_i \Lambda Z^2}{T^{3/2}} \quad (3.9)$$

In this context, Λ is the Coulomb logarithm, Z is the charge number of ions. This relation reflects the frequency of effective collisions affecting the electron's motion due to the ions' electric field. For the effective collision frequencies of our species we followed (Spitzer, 1962; Leake et al., 2005).

We do not calculate the uniform resistivity from the collision frequencies of electrons with ions and neutrals as Leake & Linton (2013). Instead, we use a constant uniform resistivity of $\eta = 4.6 \Omega \text{ m}$ (10^{-2} in non-dimensional units). That way, we focus only on the effects of the perpendicular resistivity term (η_\perp). The perpendicular resistivity due to the ambipolar diffusion of neutrals is given by

$$\eta_\perp = \frac{\xi_n B^2}{\alpha_n}, \quad (3.10)$$

where $\alpha_n = m_e n_e \nu'_{en} + m_i n_i \nu'_{in}$ is calculated using the effective collisional frequencies for electron-neutral collisions (ν'_{en}) and for ion-neutral collisions (ν'_{in}) as we discussed before. The neutral fraction (ξ_n) is defined as

$$\xi_n = \frac{n_n}{n_n + n_i}. \quad (3.11)$$

Just for clarity, we note here that the expressions and names used for the perpendicular resistivity vary in the literature. For instance, Leake & Linton (2013) refer to it as Pedersen resistivity ($\eta_p = \eta + \eta_\perp$), grouping the resistivity terms of the current density perpendicular to the field (Eq. 3.3, 3.4) in one term. Arber et al. (2007) refer to the perpendicular resistivity as Cowling resistivity ($\eta_c = \eta_\perp$), while Martínez-Sykora et al. (2012) refer to it as ambipolar diffusion resistivity ($\eta_{amb} = n_\perp$). Irrespective of the name used or the grouping of the terms, eventually, the terms used to describe the resistive effects in the induction and energy equation are the same. To accurately include the damping of the MHD waves through ion-neutral collisions we used the generalised Ohm's law Braginskii (1965):

$$E + (\mathbf{v} \times \mathbf{B}) = \frac{1}{\sigma} \frac{\nabla \times \mathbf{B}}{\mu_0} - \frac{\xi^2}{\alpha_n} \left[\frac{(\nabla \times \mathbf{B}) \times \mathbf{B}}{\mu_0} \right] = \frac{1}{\sigma} \mathbf{j} + \frac{\xi^2 B_0^2}{\alpha_n} \mathbf{j}_\perp \quad (3.12)$$

The combination of the Ohm's law and the Faraday law of induction gave us the induction equation 3.3. The Hall effect term is been neglected. Assuming a plasma comprised purely of hydrogen, simplifications are made with $m_{in} = m_n/2$ and $\xi_n = \rho_n/\rho$, which leads to:

$$\alpha_n = \frac{1}{2} \xi_n (1 - \xi_n) \frac{\rho^2}{m_n} \sqrt{\frac{16 k_B T}{\pi m_i}} \Sigma_{in}. \quad (3.13)$$

perpendicular conductivity is defined by:

$$\sigma_\perp = \frac{\sigma}{1 + \xi_n^2 B_0^2 / \alpha_n \sigma}, \quad (3.14)$$

from which Coulomb and perpendicular resistivities, η and η_\perp , are inversely proportional to their respective conductivities. This yields:

$$\frac{\xi_n^2 B_0^2}{\alpha_n} = \eta_\perp - \eta. \quad (3.15)$$

Therefore, Equation 3.12 is transformed into:

$$E + (\mathbf{v} \times \mathbf{B}) = \eta \mathbf{j} + (\eta_{\perp} - \eta) \mathbf{j}_{\perp}, \quad (3.16)$$

which simplifies to:

$$E + (\mathbf{v} \times \mathbf{B}) = \eta \mathbf{j}_{\parallel} + \eta_{\perp} \mathbf{j}_{\perp}. \quad (3.17)$$

This describes that the perpendicular resistivity dissipates the currents that lie perpendicular to the magnetic field and the Spitzer resistivity acts and dissipates the currents parallel to the magnetic field. The heating term due to frictional Joule heating is:

$$Q = (E + (\mathbf{v} \times \mathbf{B})) \cdot \mathbf{j} = \eta \mathbf{j}_{\parallel}^2 + \eta_{\perp} \mathbf{j}_{\perp}^2, \quad (3.18)$$

with \mathbf{j}_{\parallel} and \mathbf{j}_{\perp} being the current components parallel and perpendicular to the magnetic field. We also solve the ideal gas law, which is

$$P = \frac{\rho k_B T}{\mu_m}, \quad \text{where } \mu_m = \frac{m_i}{2 - \xi_n}. \quad (3.19)$$

For the reduced mass μ_m , we use $m_i = m_f m_p$, where m_p is the mass of proton and $m_f = 1.25$, k_B is Boltzmann constant.

For the specific internal energy equation, we take into account changes both to the temperature and to the ionization level,

$$\epsilon = \frac{k_B T}{\mu_m(\gamma - 1)} + (1 - \xi_n) \frac{X_i}{m_i}, \quad (3.20)$$

where $\gamma = 5/3$ and $X_i = 13.6$ eV is the first ionization energy of hydrogen. When performing simulations without the effects of partial ionization ($\xi_n = 1$), we omit the second term of the equation and keep only the gas term to compare the results with previous simulations of fully ionized plasma. The second term on this equation is the induced effects of the ionization-recombination to the equation of state.

For regions below photosphere the environment there is in local thermodynamic equilibrium (LTE) due to small mean free path, so in order to properly calculate ξ_n

we used the Saha equation which yields to:

$$\frac{(n_i)^2}{n_n} = \frac{2}{N_H} \left(\frac{2\pi m_e k_B T}{h^2} \right)^{\frac{3}{2}} e^{-\frac{\xi_n}{k_B T}} \quad (3.21)$$

The n_i is the number density of ions, n_n is the number density of neutrals, N_H is the total number density, h is the Planck constant and m_e is the mass of the electron. For the solar atmosphere the problem has an additional complexity as the chromosphere is in non-LTE condition so in order to properly calculate ξ_n the regular Saha equation is insufficient. We followed the method that Leake & Linton (2013) described using a modified Saha equation Brown (1973) which derives the $\frac{(n_i)^2}{n_n}$ ratio in an environment which departs from the LTE. So a steady state solution of the ionization equation according to (Athay & Thomas, 1961) yields to :

$$\frac{n_i^2}{n_n} = \frac{f(T)}{b(T)}, \quad (3.22)$$

$$f(T) = \left(\frac{2\pi m_e k T}{h^3} \right)^{\frac{3}{2}} \exp \left(-\frac{X_i}{kT} \right), \quad (3.23)$$

$$b(T) = \frac{T}{w T_R} \exp \left(\frac{X_i}{4kT} \left(\frac{T}{T_R} - 1 \right) \right) \quad (3.24)$$

T_R is the temperature of the photospheric radiation field while w is its dilution factor. In our Sun's interior the $T_R = T$ and $w = 1$ therefore $b(T) = 1$ however, in our Sun's atmosphere we use $T_R = 6420K$ and $w = 0.5$ like (Leake & Linton, 2013). This ratio of $\frac{n_i^2}{n_n}$ can be calculated using the following formula:

$$r = \frac{n_n}{n_i} = \frac{1}{2} \left(-1 + \sqrt{1 + \frac{4\rho n_i^2}{m_i n_n}} \right) \quad (3.25)$$

To determine the neutral fraction ξ_n , using this definition of r 3.25, we can rewrite the expression for ξ_n as follows:

$$\xi_n = \frac{n_n}{n_n + n_i} = \frac{rn_i}{rn_i + n_i}$$

We can factor out n_i in the denominator:

$$\xi_n = \frac{rn_i}{n_i(r+1)} = \frac{r}{r+1}$$

Thus, we arrive at the expression:

$$\xi_n = \frac{r}{1+r}$$

This formulation shows that ξ_n is dependent on the ratio r . The above set of equations is normalized using the photospheric values of density $\rho_u = 1.67 \times 10^{-7} \text{ g cm}^{-3}$, length $H_u = 180 \text{ km}$ and magnetic field strength $B_c = 300 \text{ G}$. Using the value of m_i mentioned before, we get temperature $T_u = 649 \text{ K}$, velocity $v_u = 2.1 \text{ km s}^{-1}$ and time $t_u = 86.9 \text{ s}$.

3.1.3 Initial conditions

The computational domain has a physical size of 64.8^3 Mm in a 420^3 uniform grid. The interior extends at $-7.2 \text{ Mm} \leq z < 0 \text{ Mm}$, the photospheric-chromospheric layer at $0 \text{ Mm} \leq z < 1.8 \text{ Mm}$, the transition region at $1.8 \text{ Mm} \leq z < 3.2 \text{ Mm}$ and an isothermal corona at $3.2 \text{ Mm} \leq z < 57.6 \text{ Mm}$. In our simulation, we employ three types of boundary conditions: periodic, open, and closed.

1. ****Periodic Boundary Conditions**:** These conditions are applied in the y -direction. Periodic boundary conditions mean that the simulation domain behaves as if it is continuous and wraps around in the y -direction. In other words, the values on one boundary match the values on the opposite boundary, creating a seamless transition. This allows for a representation of an infinite domain in the y -direction by reducing edge effects and minimizing artificial reflections.
2. ****Open Boundary Conditions**:** In the x -direction and at the top of the numerical box, we use open boundary conditions. Open boundaries allow material, energy, or waves to flow out of the simulation domain freely without reflecting back into the domain. This is useful for simulating astrophysical plasmas where waves and fluxes are expected to leave the system, ensuring that they do not artificially accumulate or reflect within the computational grid.
3. ****Closed Boundary Condition**:** At the bottom of the numerical box, we

use a closed boundary condition. A closed boundary condition prevents material, energy, or waves from entering or leaving the domain at this boundary, effectively acting as a rigid wall. These boundary conditions help ensure that the simulation accurately reflects the intended physical processes while managing the interaction of the domain with its edges. We place a cylindrical twisted flux tube $2.3Mm$ below photosphere.

We use two simulations in this study (FI and PI). The FI assumes a fully ionized plasma while the PI assumes a partially ionized plasma, our goal is to compare this two simulation to infer the differences and the effects that the partially ionized plasma will have to the magnetic flux emergence process.

The background of both simulations is comprised by an adiabatically stratified solar interior (making the interior marginally stable to convection) and a stratified model atmosphere, both in hydrostatic equilibrium. We note that the reduced mass for the FI simulation is $\mu_m = m_i$ instead of $\mu_m = m_i/2$. That way we take into account the mass of the neutrals and get realistic coronal densities.

For both simulations, we assume the temperature of the atmosphere ($z > 0$) to follow a tangential temperature profile,

$$T(z) = T_{ph} + \frac{T_{cor} - T_{ph}}{2} \left(\tanh \frac{z - z_{cor}}{w_{tr}} + 1 \right), \quad (3.26)$$

where $T_{ph} = 6360$ K, $T_{cor} = 0.95$ MK, $z_{cor} = 2.52$ Mm and $w_{tr} = 0.18$ Mm. Having set this atmospheric temperature profile, we numerically solve the hydrostatic equation $dP/dz = -gz$ using an Euler method with central differences solver to derive the density of the atmosphere. We get a photospheric density of $\rho_{ph} = 1.67 \times 10^{-4}$ kg m⁻³. For PI, we also calculate the neutral fraction ξ_n of the resulting T and ρ profiles as we discussed before.

To setup the initial stratification below the photosphere ($z < 0$), we require the vertical temperature gradient, assuming that a plasma element moves adiabatically. That is estimated using energy Eq. 3.20. For the FI simulation ($\xi_n = 0$) we omit the second term of Eq. 3.20, which simplifies the equation significantly. From that equation, the temperature profile for FI is:

$$\left(\frac{dT}{dz} \right)_a = -\frac{\mu_m g}{k_B} \frac{\gamma - 1}{\gamma}. \quad (3.27)$$

This equation is solved analytically and then the density is calculated by solving numerically the hydrostatic equation. The boundary conditions are T_{ph} and ρ_{ph} . This stratification have been used in numerous FI flux emergence simulations (e.g. Fan, 2001b; Manchester et al., 2004; Archontis et al., 2004; Moreno-Insertis et al., 2008; Toriumi & Yokoyama, 2011; Leake et al., 2013; Syntelis et al., 2017).

However, in PI, the full Eq. 3.20 is needed in order to derive the temperature profile of the solar interior. Otherwise, the PI interior will not be adiabatically and convectively stable. Taking into account the full Eq. 3.20, Leake & Linton (2013) showed that the temperature profile for the solar interior becomes:

$$\left(\frac{dT}{dz}\right)_a = -\frac{\mu_m g}{k_B} \frac{\gamma - 1}{\gamma} \left(\frac{1 + \theta \frac{\zeta(1-\zeta)}{2}}{\frac{\gamma}{\gamma-1} + \theta^2 \frac{\zeta(1-\zeta)}{2}} \right), \quad (3.28)$$

where

$$\theta = \frac{\gamma}{\gamma - 1} + \frac{X_i}{k_B T}, \quad \text{and} \quad \zeta = 1 - \xi_n. \quad (3.29)$$

The method to solve this equation is described in Leake & Linton (2013). Briefly, we initially set $\zeta = 1$ (i.e. assume the plasma to be FI) and use as boundary conditions T_{ph} and ρ_{ph} . We use a 4th order Runge-Kutta scheme to solve Eq. 3.28 for $z < 0$ and then find the density by numerically solving the hydrostatic equation. Using the Saha equation, we calculate for the current T and ρ a new ionization fraction, ξ_n , and then the new ζ and θ . Then, we iterate these steps, until ζ converges for a set of T , ρ in the interior.

The resulting temperature, density and neutral fraction of the stratified interior and atmosphere is shown in Fig. 3.2. We overplot the same parameters from the model atmosphere C7 of Avrett & Loeser (2008) for comparison. In the temperature profile plot, the small difference between our curves and the C7 model is due to the fact that we are using only a plasma with hydrogen atom, while the C7 model also includes helium atom.

Inside the interior, we place a horizontal cylindrical twisted flux tube along the y -axis. The magnetic field of the flux tube is defined as

$$B_y = B_0 \exp(-r^2/R^2), \quad (3.30)$$

$$B_\phi = \alpha r B_y, \quad (3.31)$$

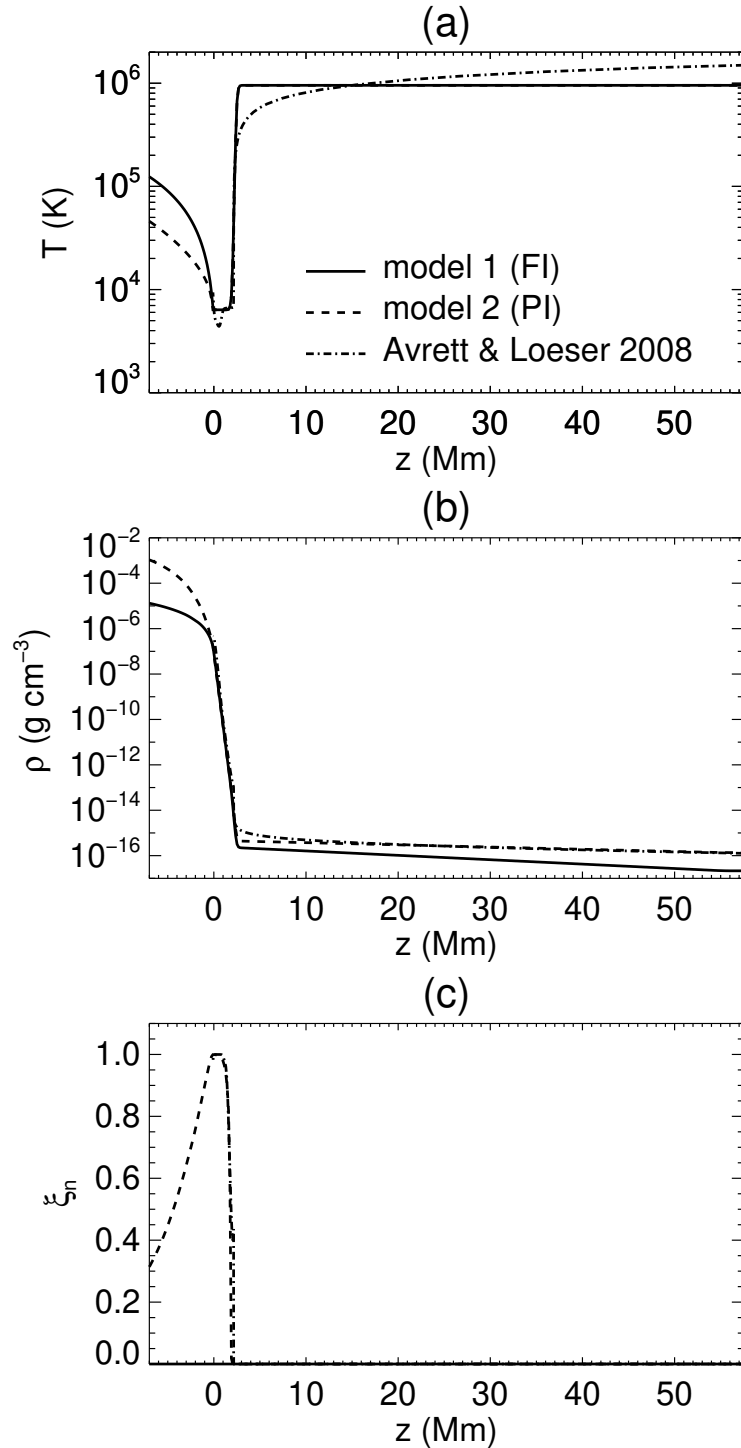


Figure 3.2: The (a) temperature stratification, (b) density stratification and (c) the neutral fraction of the solar interior and the atmosphere of the simulations. The solid line is FI (solid) and the dashed line is PI (dashed). Over plotted with a dashed-dot line is model C7 of Avrett & Loeser (2008) for comparison.

where $R = 450$ km is a measure of the FT's radius, r is the radial distance from the FT's axis and $\alpha/2\pi$ is the twist per unit of length. We set $\alpha = 0.4$ (0.0023 km $^{-1}$), which makes the flux tube highly twisted but kink stable. To ensure radial force balance in the flux tube with the surrounding plasma, the internal gas pressure p_i inside the tube is adjusted based on the external gas pressure and the magnetic field of the tube. The internal pressure p_i is defined as:

$$p_i = p_e + p_{\text{exc}},$$

where:

- p_e is the external gas pressure, which represents the background plasma pressure outside the flux tube,
- p_{exc} is the pressure excess resulting from the magnetic field within the flux tube.

Given the magnetic field components of the flux tube, the pressure excess p_{exc} is derived as:

$$p_{\text{exc}} = \frac{1}{2\mu} \left(\alpha^2 \left(\frac{R^2}{2} - r^2 \right) - 1 \right) B_y^2,$$

where:

- μ is the magnetic permeability,
- α represents the twist parameter of the magnetic field,
- R is the characteristic radius of the flux tube,
- r is the radial distance from the flux tube axis,
- B_y is the longitudinal magnetic field component.

This pressure profile ensures that the radial gas pressure gradient balances the magnetic forces, maintaining equilibrium within the flux tube. The total pressure (gas + magnetic) inside the tube equals the external total pressure, satisfying the equilibrium condition.

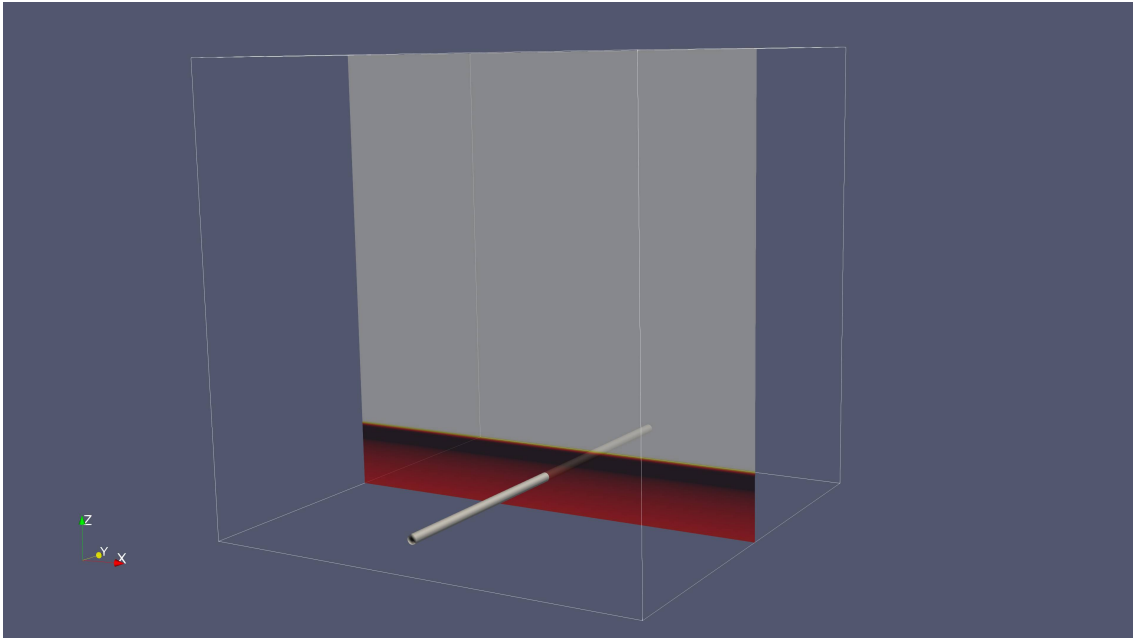


Figure 3.3: 3D flux tube representation at the start of the simulation.

For FI, we set the magnetic field's strength to $B_0 = 3150$ G ($\beta = 18.4$). Notice in Fig. 3.2 that the FI and PI background stratifications have different densities and temperatures in the interior, as it results from solving two different equations. For PI, we, therefore, do not use the same B_0 as FI, but the same β . That results to $B_0 = 7882$ G for PI.

At figure 3.3 we have plotted in 3D the isocontours of the magnetic field configuration, just to display how the initial conditions look. The FT is placed at the upper convection zone and the contour plot in the xz midplane corresponds to the logarithm of the temperature at the start of each simulation. If we took the projection of the magnetic field configuration of the FT to the xz plane will look like circular contours as we show in figure 3.4, the white contours correspond to the axial magnetic field component B_y and the filled contours correspond to the logarithm of the density at the start of the simulation.

To make the flux tube emerge, we change the density profile inside the flux tube. For FI, we use the usual method (e.g. Fan, 2001b). The background solar interior has a pressure, temperature and density profile of P_0 , T_0 and ρ_0 . By adding the flux tube, we add an additional pressure excess due to the magnetic field. Firstly, we require this pressure excess to be in radial force equilibrium ($dP_{exc}/dr = (\mathbf{j} \times \mathbf{B})\hat{\mathbf{e}}_r$,

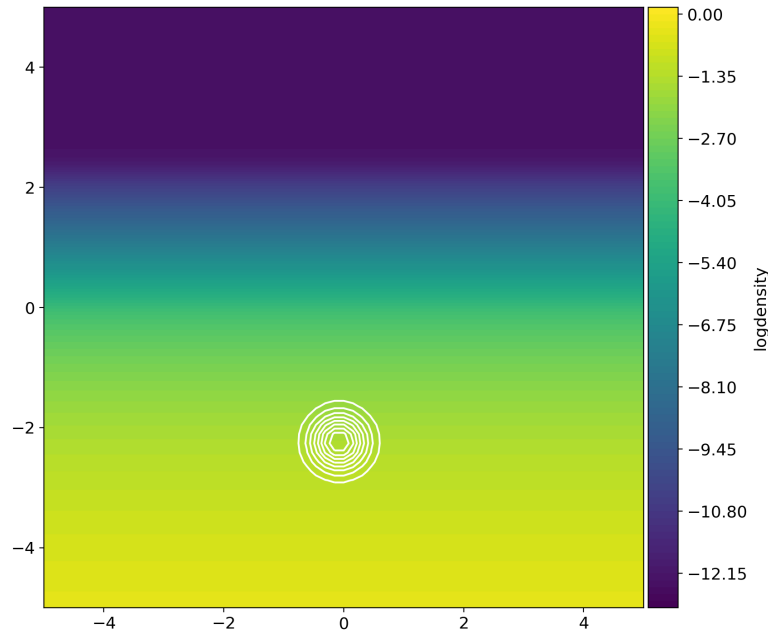


Figure 3.4: contour plot of the magnetic field at the start of the simulation in the xz midplane.

finding the equation of P_{exc} to be (Murray et al., 2006):

$$P_{exc} = \frac{1}{2\mu} \left[\alpha^2 \left(\frac{R^2}{2} - r^2 \right) - 1 \right] B_y^2 \quad (3.32)$$

Then, we require the flux tube to be in pressure equilibrium. The gas pressure in the interior of the tube, P_i , becomes $P_i = P_0 - P_{exc}$. Because inside the solar interior the isotropic thermal conduction is large, we expect the magnetized plasma to be in thermal equilibrium with the background non-magnetized plasma. We therefore set the flux tube to be in thermal equilibrium with the background ($T_i = T_0$). That leads to a density deficit ($\Delta\rho = \rho_i - \rho_0$) in the interior of the flux tube of $\Delta\rho = -\rho_0 P_{exc}/P_0$ that makes the flux tube buoyant. To avoid emerging the whole length of the flux tube, we reduce the density deficit towards the flanks of the flux

tube by

$$\Delta\rho = -\rho_0 \frac{P_{exc}}{P_0} e^{-y^2/\lambda^2}, \quad (3.33)$$

where λ is thus a measure of the length of the buoyant part of the flux tube. The above ensures that the middle part of the flux tube will be buoyant, while the flanks will not. Thus the flux tube will adopt an Ω -loop shape. We use $\lambda = 0.9$ Mm.

For PI we need to follow the same steps, but also take into account that changes in ρ_i result in changes in the neutral fraction and therefore the reduced mass in the interior of the tube. P_{exc} will be the same. By setting $P_i = P_0 - P_{exc}$ and $T_i = T_0$, we get when the flux tube is in pressure balance and in thermal equilibrium with the background, the density in the interior of the flux tube is:

$$\rho_{i,teq} = \rho_0 \frac{\mu_{mi}}{\mu_{m0}} (1 - P_{exc}/P_0), \quad (3.34)$$

where μ_{mi} and μ_{m0} are the reduced mass of the interior of the flux tube and of the non-magnetized background. To make the flux tube adopt an Ω -loop shape as before, we use a function that sets the density at the middle part of the flux tube to $\rho_i = \rho_{i,teq}$ and at the flanks to $\rho_i = \rho_0$:

$$\Delta\rho = -\rho_0 \left[1 - \frac{\mu_{mi}}{\mu_{m0}} (1 - P_{exc}/P_0) \right] e^{-y^2/\lambda^2}. \quad (3.35)$$

Indeed, notice that for $y = 0$, $\rho_i = \rho_{i,teq}$ and that for $y \gg \lambda$, $\rho_i = \rho_0$. Also, for $\mu_{mi} = \mu_{m0}$ (i.e. non PI effects), we recover Eq. 3.33.

To calculate ρ_i and μ_i , we numerically solve Eq. 3.35 in the following manner:

1. First, P_{exc} is calculated and $P_i = P_0 - P_{exc}$ is set.
2. Then, μ_{m0} of the background is found.
3. An initial guess for μ_{mi} is assumed to be $\mu_{mi} = \mu_{m0}$.
4. Then, ρ_i is calculated from Eq. 3.35.
5. The internal energy ϵ_i is calculated from Eq. 3.20. Then, the temperature T_i is calculated from Eq. 3.19

6. Based on the current values of temperature and density, the new ξ_{ni} and μ_{mi} are computed.
7. Steps 4-6 are repeated until ξ_{ni} converges to a value.

Using the above method, we derive the temperature, specific energy, density and gas pressure profile of the flux tube and the corresponding neutral fraction of the magnetized plasma.

3.2 Results

3.2.1 Magnetic flux emergence through the solar convection zone

To examine the magnetic flux emergence beneath the photosphere, we initially track the upward movement of both the tube's center and its apex in both simulations. The tube's centre is identified at the vertical xz-midplane, where B_y is at its peak and B_x switches its sign along the height. We simply determine the tube's apex as the point where the magnetic field's strength drops to approximately $0.001 \times B_0$ at the boundary of the field. The progression of the emergence over time in both simulations is depicted in Figure 3.5.

Our observations indicate that the axis of the tube in both simulations emerges similarly up to approximately $t = 25$ minutes (see Figure 3.5). Yet, post the $t = 25$ minute mark, the emergence patterns of the two flux tubes diverge. In the FI scenario, the tube's axis continues in its ascent until it touches the photosphere. Conversely, in the PI scenario, the tube's axis remains situated roughly 2Mm beneath the photosphere for the simulation's duration. We attribute the difference to the ion-neutral interactions, in the solar upper convection zone. At the area that the axis is, the ion-neutral collisions are not sufficient to have the slippage effect so the transfer of momentum from the ion-neutral interactions acts like "friction" thus slowing the rise of the FT axis. The failed emergence in the PI case is an important result. The axis carries the majority of the flux that will emerge into the solar atmosphere, so its sub-photospheric retention impacts the overall magnetic flux emergence process. From Figure 3.5, we also find that the expansion of the magnetic field above

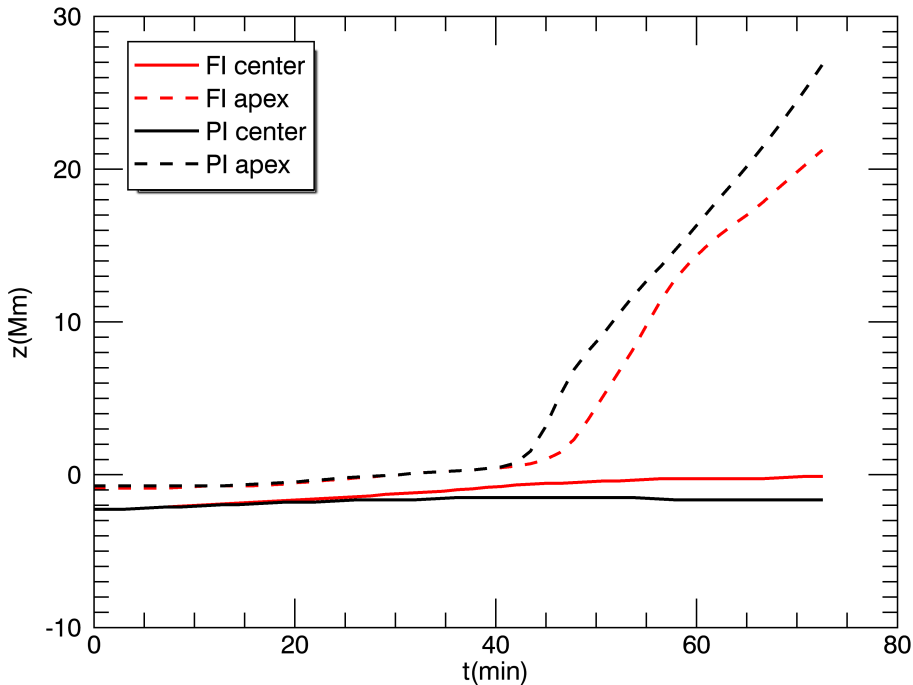


Figure 3.5: Height time profile of flux tube axis and apex on both our simulations.

the photosphere occurs earlier in the PI simulation. This is because, the inclusion of the ion-neutral collisions and the increased dissipation allows the magnetic field to slip through the plasma during emergence and, thus, it doesn't carry within it so dense plasma as in the FI case. Thus, the apex of the field is less heavy in the PI case and it can expand earlier.

The observed effect is also evident beneath the photosphere. Both Figure 3.6 and Figure 3.7 depict the magnetic flux tube's emergence within the solar interior for the two respective simulations. The contours, representing the tube's cross-section at the vertical xz -midplane, correspond to B_y values exceeding $3 \times 10^{-3}T$. In the FI scenario (see Figure 3.6), the field's emergence exhibits a conventional pattern consistent with numerous previous magnetic flux emergence studies. Specifically, the tube ascends vertically, and upon nearing the photosphere, its ascent moderates, and it extends horizontally before eventually becoming unstable and emerging beyond the photosphere. Conversely, in the PI scenario (as seen in Figure 3.7), the tube's cross-sectional shape, particularly its upper section approaching the ph-

tosphere, is distinct. Notably, it appears less flattened and lacks the pronounced horizontal expansion characteristic of the FI scenario, assuming a more spindle-like configuration. For instance, at times $t = 22$, $t = 33$, and $t = 43$ minutes, the tube demonstrates more pronounced vertical than horizontal stretching. We posit that the perpendicular resistivity effectively dissipates cross-field currents, facilitating the magnetic field's ability to "slip" through the plasma. This results in a unique emergence pattern for the field. Consequently, the emergent bipolar region at the photosphere manifests with a different shape.

3.2.2 Emergence of Magnetic Flux at the photosphere

Figure 3.8 displays the vertical component of the magnetic field at the photosphere over time. The general evolution reveals the characteristic pattern of an emerging bipolar region. Initially, two opposite polarities are visible along the x-axis, mainly due to the tube's significant twist, and later move apart along the y-axis. This results in the formation of a distinct polarity inversion line (PIL) between them.

There are noticeable differences in the evolution of the emerging region between the two cases. In the PI scenario, the polarities present a more circular and compact shape. This observation aligns with the first row of Figure 3.8, where the magnetic contours at the intersection with the photosphere in the PI case appear more vertical. Additionally, the magnetic tails adjacent to the PIL are more pronounced in the FI case, as shown in the second row of Figure 3.8.

To better comprehend these differences, we analyzed the evolution of the magnetic field's components at the photosphere. Figure 3.9 illustrates the peak values of these components at $x=y=0$, at the photosphere's base. These values are normalized using the maximum of the initial total magnetic field. Two primary observations emerge: First, a larger proportion of the magnetic field components reaches the photosphere in the FI case; this is linked with the presence of neutral atoms in the upper convection zone. Consequently, they introduced a heightened perpendicular resistivity thus greater magnetic diffusivity at the convetcion zone in comparison with the FI simulation impacting the proportion of the magnetic field that reaches the photosphere. Second, the dominant component in the PI scenario is B_z , which is consistent with the appearance of the polarities in the first row of Figure 3.8. Conversely, in the FI case, the axial component, B_y , is predominant, matching the

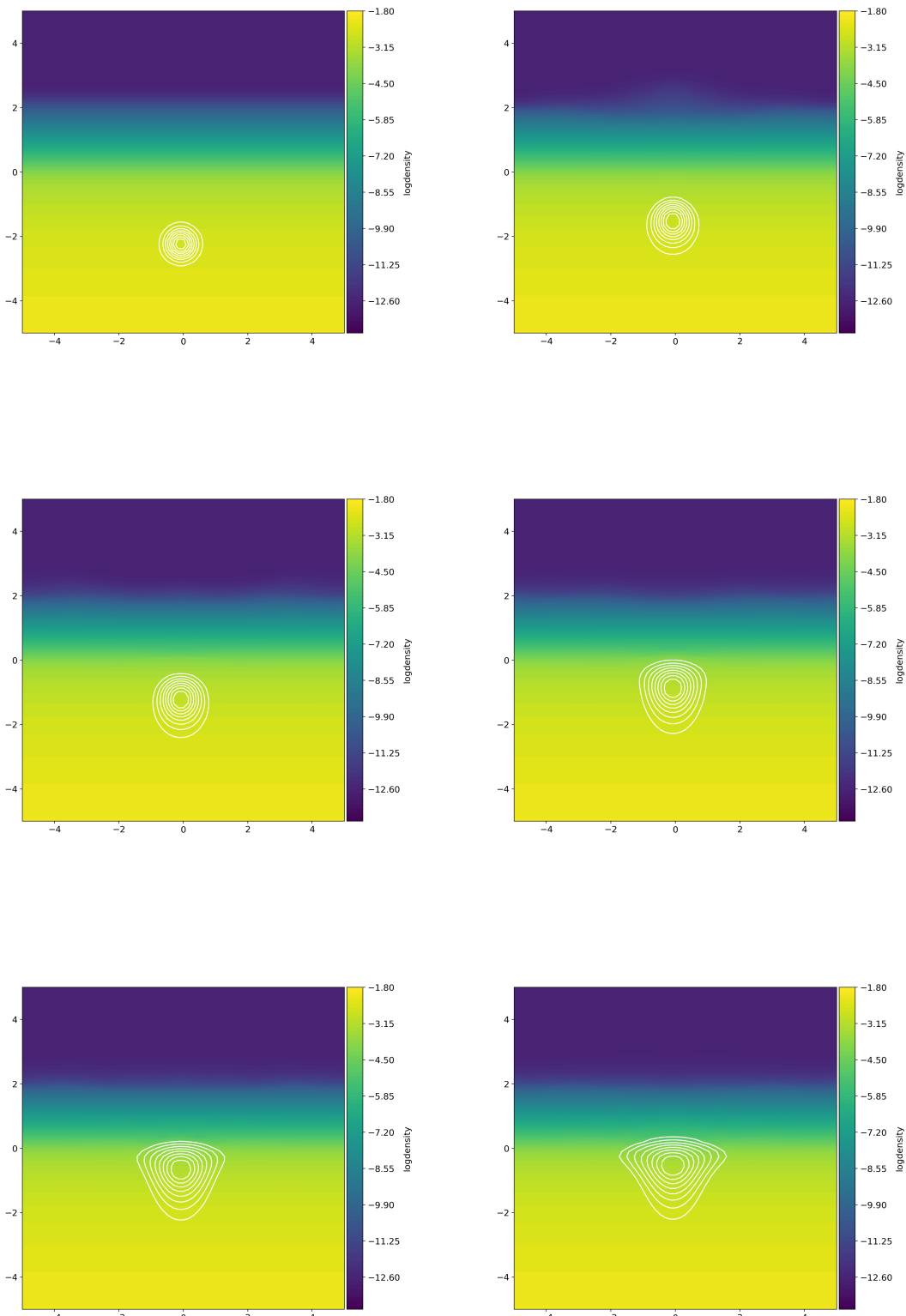


Figure 3.6: The evolution of B_y on xz plane on the FI simulation from up left to bottom right at $t=0, 22, 29, 36, 40, 43$ minutes.

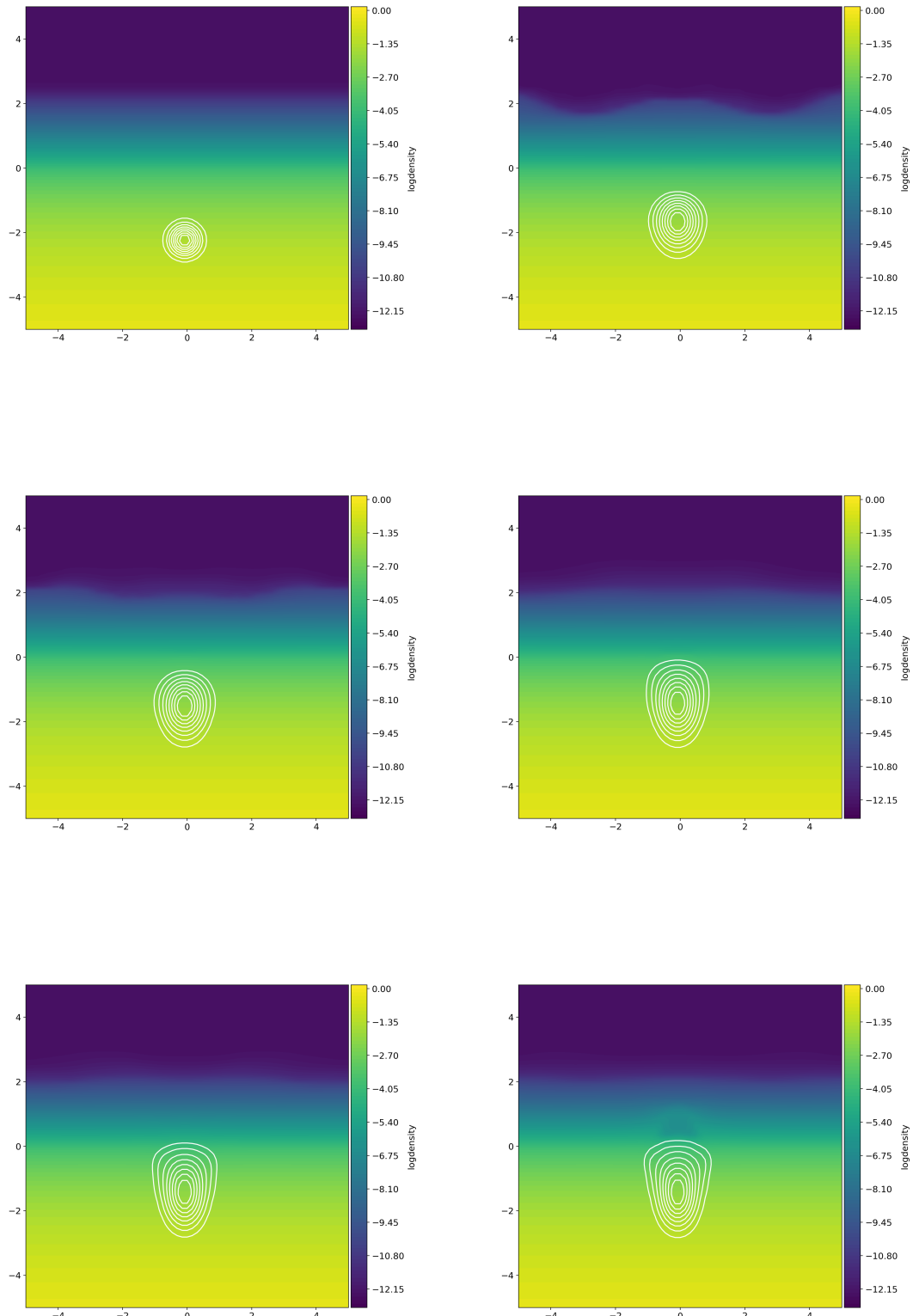


Figure 3.7: The evolution of B_y on xz plane on the PI simulation from up left to bottom right at $t=0, 22, 29, 36, 40, 43$ minutes.

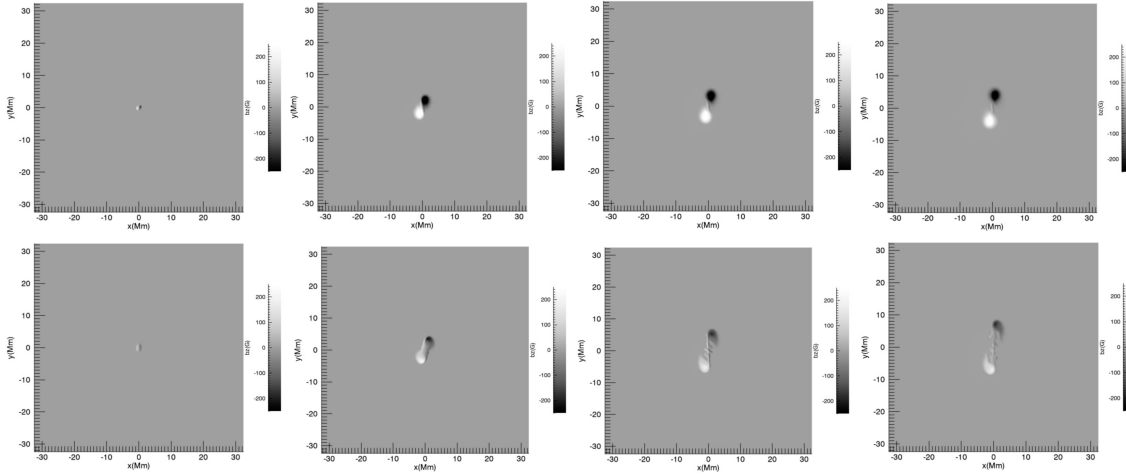


Figure 3.8: The evolution of bipolar region on PI simulation(first row) and FI simulation (second row) from left to right 43,72,115 and 159 minutes.

height-time profile of the tube shown in Figure 3.5.

3.2.3 Evolution of Flux and Energy

To understand the balance between emergence and shearing processes, we trace the temporal evolution of the Poynting flux at $z = 1.2Mm$. We categorize the Poynting flux into two distinct contributions: the “emergence” and the “shear”, defined as:

$$S_{xy} \text{emergence} = +\frac{1}{4\pi} \int_x \int_y v_z (B_x^2 + B_y^2) dx dy \quad (3.36)$$

$$S_{xy} \text{shear} = -\frac{1}{4\pi} \int_x \int_y (v_x B_x + v_y B_y) B_z dx dy \quad (3.37)$$

Figures 3.10 and 3.11 depict the temporal evolution of these contributions for the FI and PI simulations respectively. Meanwhile, Figure 3.12 highlights the difference between the shear and emergence contributions. The emergence term is larger than the shear term, which is reasonable, since the intense shearing starts after the bipolar region emerges at the photosphere. Eventually, the shear term becomes larger than the emergence term and it becomes the dominant term during the evolution of the system. Post $t = 80min$, the periodic patterns emerge as a result of solar eruptions. The intricacies of these eruptive patterns will be discussed in a subsequent chapter.

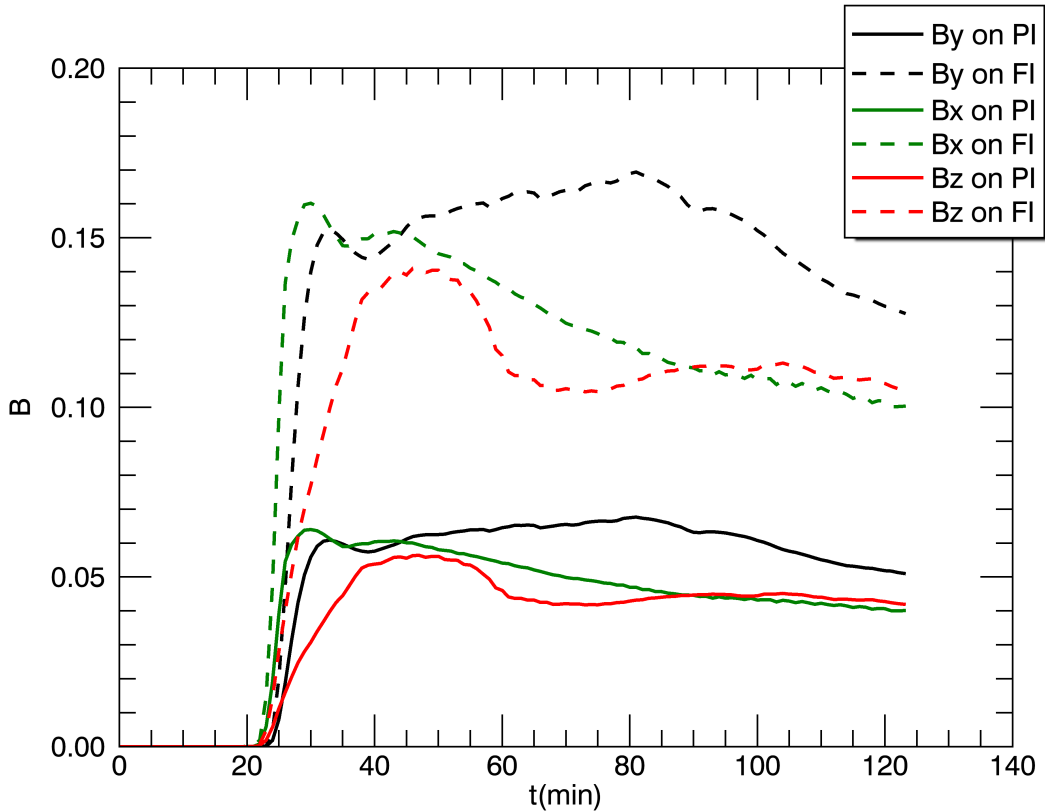


Figure 3.9: Time evolution of the normalized B components at the base of the photosphere.

The difference between the two terms is larger in the PI case.

In order to enhance the robustness of our results we run a simulation that we termed Fib0pi with a fully ionized plasma. This simulation has exactly the same setup as the FI but it has the same initial magnetic field as the PI. In this simulation (Fib0pi) the disparity between the terms is even more evident. The latter indicates that the inclusion of the partial ionization alone does not determine solely the amount of energy and/or flux, which is transferred at the photosphere and above an emerging bipolar region.

To quantify the in-plane flux, we calculate the normalized in-plane flux using the formula:

$$\frac{F_{xz}}{F_{xz_0}} = \frac{\int_{z>1.2Mm} \int_x B_y dx dz}{\int_z \int_x B_{y0} dx dz} \quad (3.38)$$

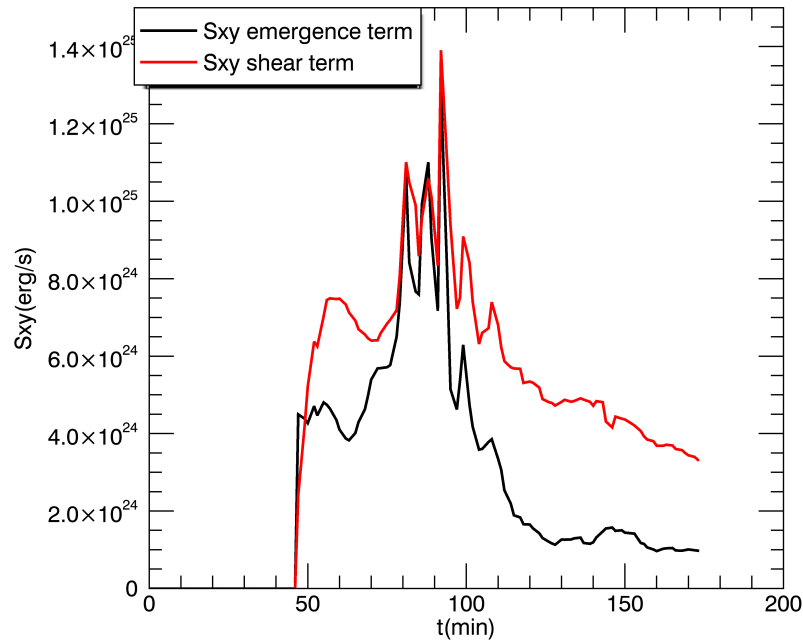


Figure 3.10: Emergence and shear term of Poynting flux on FI simulation at the mid-photosphere.

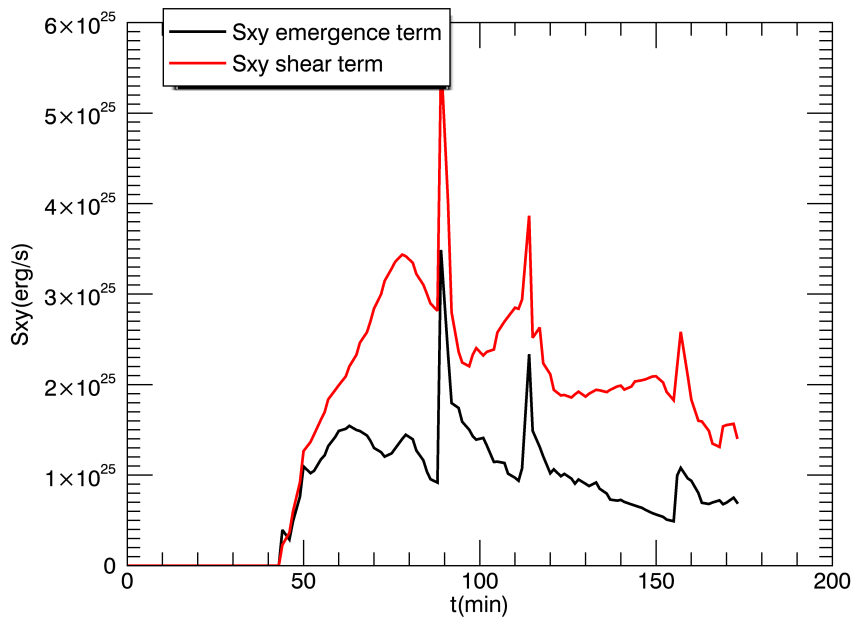


Figure 3.11: Emergence and shear term of Poynting flux on PI simulation at the mid-photosphere.

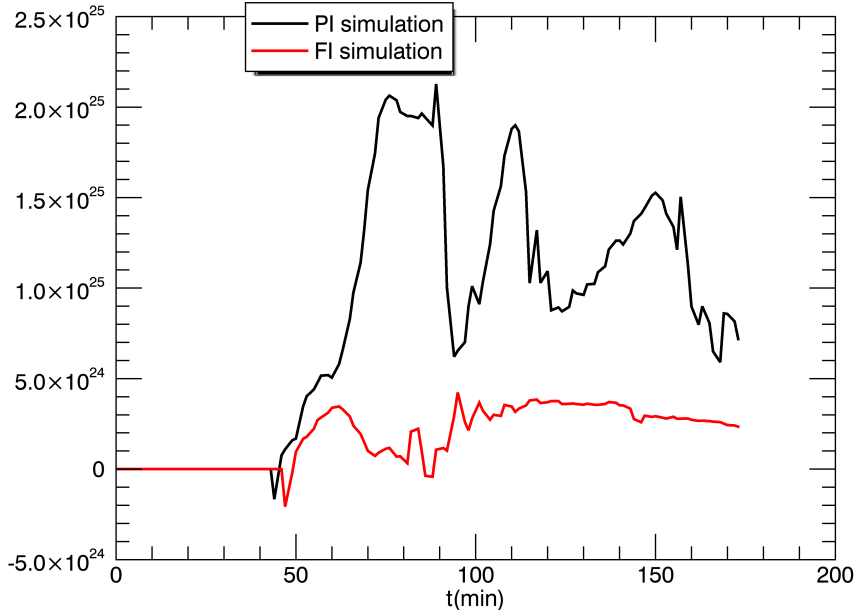


Figure 3.12: The difference between the shear and emergence terms of the Poynting flux.

where B_{y_0} represents the axial component of the magnetic field within the flux tube at $t = 0$ and $y = 0$. The resulting data is illustrated in Figure 3.13. For the initial period, specifically for $t \leq 53$ minutes, the in-plane flux in the PI scenario surpasses that of the FI scenario. This is attributed to the earlier emergence and expansion of the tube above the photosphere in the PI case. However, as the system progresses, the FI scenario takes the lead, exhibiting a greater in-plane flux. This observation suggests that a more substantial fraction of the axial field (B_y) is conveyed above the photosphere in the FI scenario.

To quantify the unsigned normalized in-plane vertical flux, we employed the equation:

$$\frac{F_{xy}}{F_{xy_0}} = \frac{\int_x \int_y |B_z| dx dy}{\int_x \int_y |B_{z_0}| dx dy} \quad (3.39)$$

This flux is normalized with respect to the total initial in-plane vertical flux. For our analysis, the full range of x and y-axes was considered, while the z-value is fixed at 1.2 Mm above the photosphere. The resulting behavior is displayed in Figure

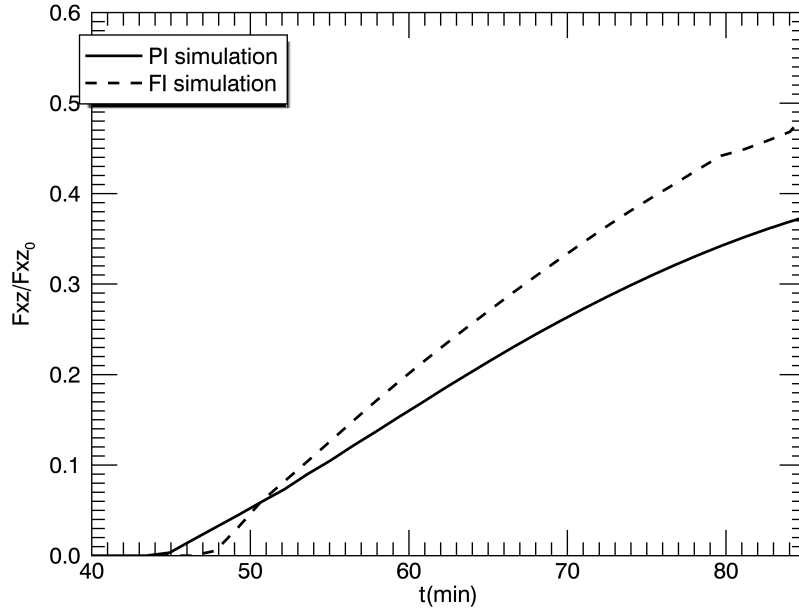


Figure 3.13: Emerged normalized in plane flux above $z=1.2\text{Mm}$.

3.14. Initially, a swift ascent in flux is observed in both scenarios, attributable to the magnetic flux tube's early emergence at this altitude. This initial rise is then followed by a more gradual increase, eventually plateauing as the flux available for emergence at this height is exhausted. Overall, the peak vertical flux observed above the photosphere exhibits similarities in both simulations, with the FI case showing a slightly elevated value. Notably, including PI doesn't significantly enhance the emergence of vertical flux in the solar atmosphere.

Further, we also wanted to study the evolution of the proportion of the axial field energy (linked to the axial field component B_y) in relation to the total magnetic energy that gets transmitted to the solar atmosphere, the y coordinate is 0. For this purpose, we computed:

$$E_{axial} = \frac{\int_x \int_{z>0.36} B_y^2 dx dz}{\int_x \int_{z>0.36} |B|^2 dx dz} \quad (3.40)$$

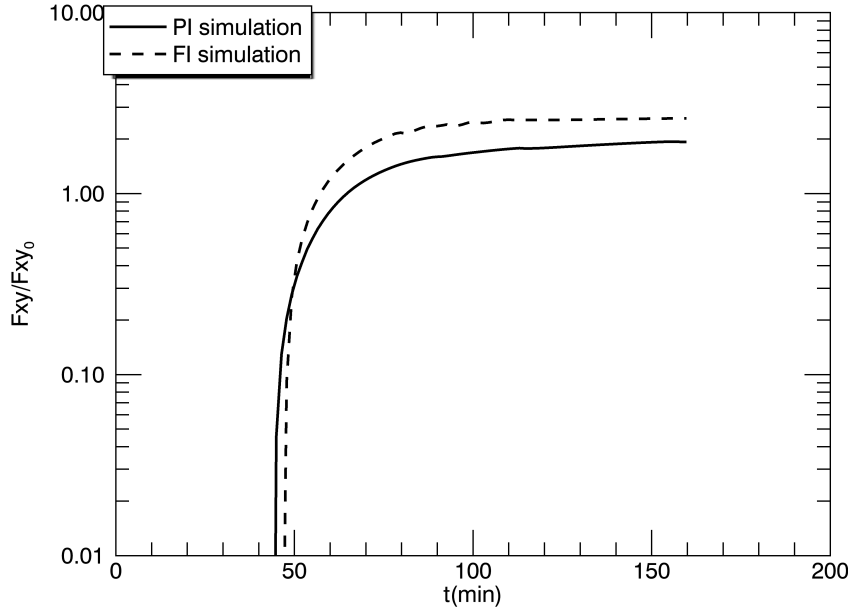


Figure 3.14: Emerged vertical in plane flux at $z=1.2\text{Mm}$.

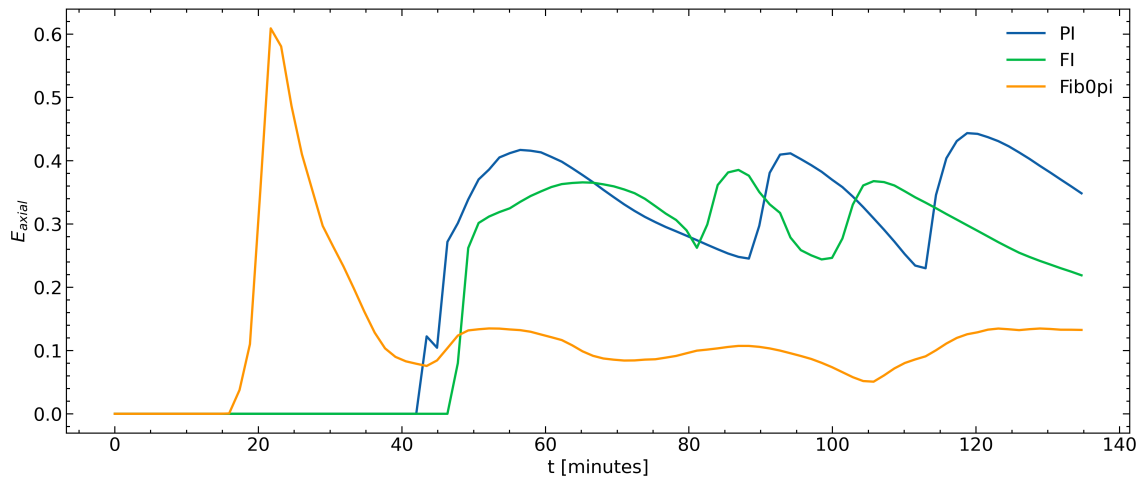


Figure 3.15: Time evolution of E_{axial} from $z > 0.36\text{Mm}$ for 3 simulations.

In Figure 3.15, we present the temporal evolution of E_{axial} for PI, FI and Fib0pi. Observations indicate that E_{axial} values are predominantly elevated in the PI in comparison with the same initial beta plasma simulation FI. This phenomenon can be attributed to the initial conditions: while the plasma beta remains consistent across both simulations, the PI case exhibits heightened values for B and B_y . The

FIb0pi at this figure 3.15 had the greatest peak located at 20 minutes which correspond to the moment that the apex reaches the $z=0.36$ Mm height. Due to the different beta plasma the evolution of the magnetic flux emergence process is entirely different, the stronger initial magnetic field create an increased horizontal expansion than the FI proving that our results for the spindle like shape of the PI flux tube apex is entirely due to the partially ionized induced slippage effect. The subsequent oscillations are attributed to the newly created FR's and it appears that even with the biggest initial magnetic field that the Fib0pi has in comparison with the FI the coronal structures that it creates have less axial magnetic energy than the PI.

3.2.4 Magnetic flux emergence at solar atmosphere

Figure 3.16 presents the magnetic flux emergence into the solar atmosphere for both the FI and PI cases, with the initial plasma beta for the sub-photospheric magnetic field held constant. The selected times for comparison are $t = 3042s$ for the FI case and $t = 2782s$ for the PI case, corresponding to when the apex of the expanding volume reaches the same atmospheric height.

Upon examining the magnetic field characteristics (B and B_y), we observe that the FI case displays a more pronounced horizontal expansion of the emerging field.

The visualization of the temperature (column 2) confirms two results, which have been reported in previous numerical simulations Leake & Arber (2006). Firstly, the temperature inside the expanding field is lower than the background temperature due to the adiabatic expansion in the FI case. Secondly, in the PI case, the inclusion of the partial ionization reduces the adiabatic cooling. We have to highlight that this process does not heat the local plasma above nominal values. Therefore, perpendicular resistivity should be considered as a mechanism that reduces the heavy cooling from the adiabatic expansion, however it should not be considered (at least in this case) as a generic heating mechanism of the atmospheric plasma.

Figure 3.17 displays a quantitative measurement of the adiabatic cooling reduction due to the effect of partial ionization. We plot the temperature along height, at the centre of the computational domain ($x=y=0$) for both cases, when the emerging field has expanded into corona. The temperature of the plasma inside the expanding volume increases to about 3000 K (solid black line), but it is still lower than the

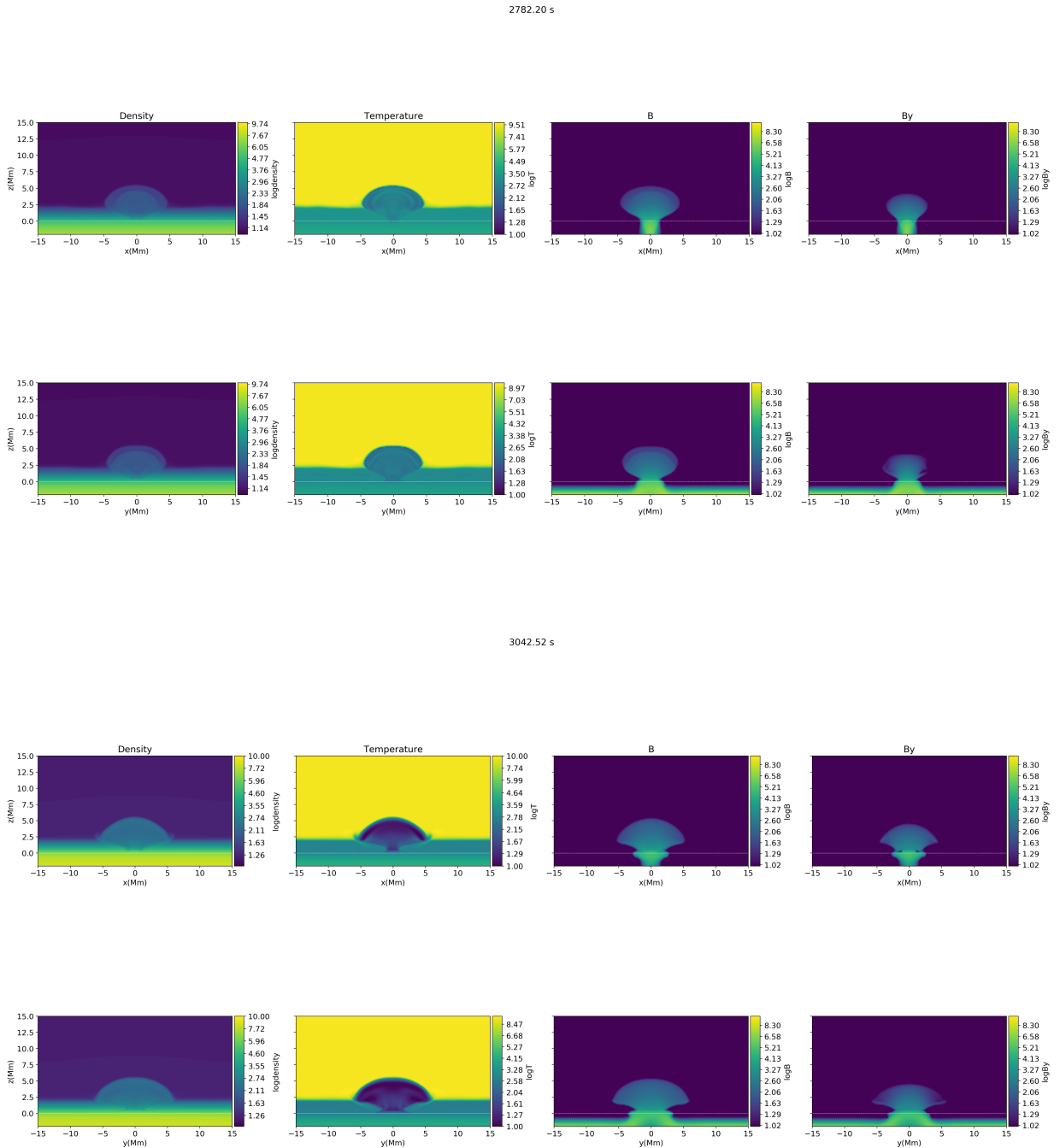


Figure 3.16: Visualization of various quantities (temperature, density, total magnetic field strength (B) and axial magnetic field (By)), for the PI case (first two rows) and the FI case (last two rows), at the vertical xz -midplane (rows 1 and 3) and at the vertical yz -midplane (rows 2 and 4), at two different times.

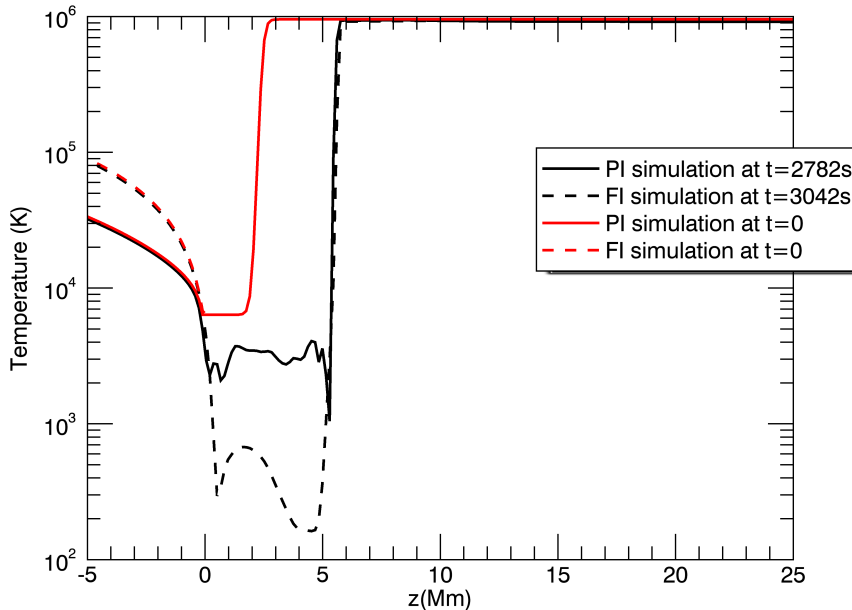


Figure 3.17: The comparison of the temperature profiles on both simulations in the $x=y=0$ plane in $t=2782\text{s}$ on FI and $t=3042\text{s}$ on PI.

nominal background value (red solid/dashed lines).

Similar to prior flux emergence simulations, our findings reveal that post-photospheric emergence is succeeded by the formation of an eruptive flux rope, driven by the shearing and reconnection of magnetic field lines along the polarity inversion line. The nature of the eruption—whether confined or ejective—hinges on specific parameters.

In studies without an ambient magnetic field in the solar atmosphere (Fan, 2001b; Archontis & Török, 2008; Archontis & Hood, 2012), the eruption remains confined when the downward tension exerted by the outer field lines of the emerging domain retains the flux rope. Such confinement arises when, for instance, the flux rope lacks the requisite free energy to effectively displace the outer field lines and erupt, or when restricted numerical domains and closed boundary conditions limit the magnetic system’s evolution. However, introducing a pre-existing magnetic field in the solar atmosphere can trigger ejective eruptions through effective reconnection with the emerging field. Nevertheless, even with a pre-existing field, a flux rope with minimal free energy can result in a confined eruption (Leake et al., 2022).

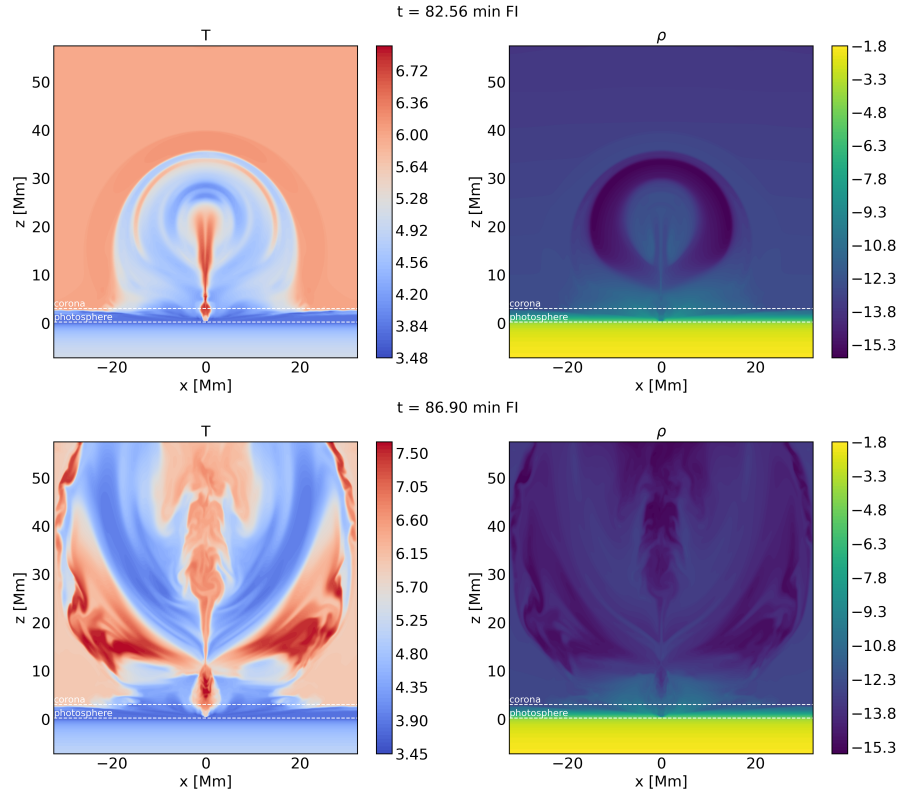


Figure 3.18: Visualization of the logarithm of the temperature and the logarithm of density in the xz midplane for FI simulation in $t=82.56$ minutes and $t=86.90$ minutes.

Interestingly, ejective eruptions can manifest even without the reconnection between emerging and pre-existing fields (Fan, 2009; Archontis et al., 2014; Syntelis et al., 2017). For instance, Syntelis et al. (2017) demonstrated that the interplay of torus instability and tether-cutting reconnection can trigger sequential eruptions. Our simulations, sharing identical initial conditions with Syntelis et al. (2017), exhibit a consistent eruption mechanism, especially evident in the FI case that we will see in more detail in the next chapter.

Figure 3.18 captures the eruption of the FI simulation at two distinct time-frames: $t = 82.56$ minutes (upper row) and $t = 86.90$ minutes (lower row). At $t = 82.56$ minutes, the flux rope's core settles between $z = 25 - 30$ Mm at $x = 0$ Mm. This region is characterized by a cool, dense plasma encasing the rope and a heated vertical plasma column beneath, stemming from a bidirectional reconnection jets. Originating in the lower corona (around $z = 3$ Mm), these jets arise from the tether-cutting reconnection of field lines that belong to the magnetic shear ar-

cade. This phase marks the eruption's transition to its ejective state. By $t = 86.90$ minutes, the ejected flux rope exits the numerical domain's upper boundary, revealing an expanding post-flare loop and a complex interplay of hot and cool coronal plasma. The eruption onset and evolution in both FI and PI simulations, and their comparative analysis, will be the focus of the next chapter of this thesis.

3.3 Discussion

Our understanding about the importance of the presence of neutral atoms in the Sun comes from a couple of theoretical models and observations. We established that the upper convection zone along with the lower atmosphere(photosphere,chromosphere) will have the presence of neutrals introducing possible effects to the dynamic evolution of the magnetic field. We have performed 3-D numerical simulations to investigate the effect of partial ionization on the magnetic flux emergence process. We have modified the single-fluid MHD equations to include the effects of neutral hydrogen on our simulations. This modification induced a different induction equation which included the collisions between the three different species and how these collisions affect the evolution of the magnetic field.

We find that partial ionization affects the emergence of magnetic flux at the photosphere. The slippage effect is an imminent result of the ion-neutral collisions leading to the dynamic movement of the ions through the plasma and simultaneously the couple of neutrals to the magnetic field. This slippage explains the slow horizontal expansion and the spindle-like shape of the emerging structure of the magnetic field.

Another result of the aforementioned phenomenon is the failed emergence of the flux tube axis in the photosphere. More precisely, the apex of the flux tube experiences the slippage effect which takes place if the ion-neutral collisions are sufficient to decouple the ions from the field. The axis on the other hand still “experiences” ion-neutral collisions but they are not sufficient in order to decouple the ions so the collisions there act like a deceleration device leading to the failed emergence of the axis to the solar surface.

The ion-neutral collisions also contribute to the reduced amount of plasma being transferred by the PI axis to the solar atmosphere. This specific characteristic is the

reason that the PI's apex starts to ascend towards the solar corona earlier than the FI case, although the emerging tubes in the two cases have the same plasma beta.

Since our numerical simulations are fully three-dimensional, we have studied also the appearance of the emerging field around the PIL at the photosphere. We have found that in the PI case, the polarities adopt a more circular-like shape. This is because the dominant magnetic field component in this case is the vertical component, B_z . On the other hand, the magnetic tails are more apparent in the FI case, where the azimuthal component of the magnetic field is very strong.

Previous studies (e.g. Khomenko & Collados, 2012; Martínez-Sykora et al., 2015; Leake & Arber, 2006; Leake & Linton, 2013) have indicated that partial ionization due to the induced perpendicular resistivity could be an important heating mechanism in the solar atmosphere. However, our simulation show that the inclusion of PI could reduce the intensive cooling from the adiabatic expansion, yet it does not heat the plasma above the nominal background values.

We have also found that the amount of the emerged flux into the solar atmosphere is slightly greater in the PI simulation. However, this is mainly due to the fact that the initial sub-photospheric magnetic fields have the same plasma beta in both cases, but the initial field strength is bigger in the PI simulation. Therefore, the inclusion of PI can not determine (alone) the amount of flux transfer at and above the solar surface. Finally, our numerical experiments show that PI does not halt the formation of unstable structures at the PIL of the emerging region, which can eventually erupt into the outer solar atmosphere. To some extent, this result contradicts the assumption, based on the outcome of previous 2.5D studies (e.g., Leake & Linton, 2013), that PI may not help to the creation of unstable coronal structures. At the next chapter we will observe how partial ionization affects the expansion of the magnetic loop to the solar atmosphere and how it affects the occurrence of the solar eruptions.

Chapter 4

Effects of partial ionization on solar eruptions.

In the previous chapter, we detailed our model and how we modified the single-fluid MHD equations to incorporate the effects of partially ionized plasma in our system. Additionally, we highlighted how partially ionized plasma influences the emergence of magnetic flux tubes below the solar atmosphere. We briefly discussed the creation of unstable coronal structures in our experiment, which eventually led to eruptions. In this chapter, we will delve deeper into how partially ionized plasma impacts these solar eruptions.

4.1 Results

4.1.1 Analysis of the Pre-Eruptive Stage

We created contour plots of the logtemperature and logdensity in various snapshots on both simulations, we analyze the development of the emerging magnetic field as its apex ascends to approximately 8 Mm, illustrated in the first and second columns of Figure 4.1. The subsequent columns capture the expansion of the plasma into the corona at a height of about 15 Mm. We observe that the interior of the PI loop maintains a greater temperature relative to the FI loop, which we attribute to the presence of neutrals within the loop that mitigate adiabatic cooling through

ion-neutral collisions, as is evident in the FI case at $t = 53.59$ min.

The second row of Figure 4.1 displays the density distribution during these evolutionary stages. Consistent with our findings in the chapter 3, the FI emergence carries denser plasma above the photosphere at the initial stages ($t = 49.24$, $t = 53.59$ min), a difference that becomes more pronounced as the field ascends higher ($t = 57.93$, $t = 60.83$ min).

At later stages, detailed in the third and fourth rows of Figure 4.1, both simulations reveal upward movement of cool and dense plasma from the centre and inside of the emerging field. In both scenarios, cool and dense plasma from the core and interior of the emerging field ascends. For the FI case, this ascent is linked to the creation of a new FR in the lower atmosphere, caused by the reconnection of sheared field lines. This process can transport dense plasma to the upper atmosphere, leading to eruptions of filament-like structures, as documented in previous studies (van Ballegooijen & Martens, 1989; Magara & Longcope, 2001; Archontis & Török, 2008; Fan, 2009; Leake et al., 2014; Syntelis et al., 2017). In contrast, in the PI case, no new FR is formed at this stage. Instead, the dense plasma is lifted by emerging arch-like field lines. A detailed structure of the emerging field is provided in following subsection.

At times when the apex of the emerging field reaches approximately 22 Mm, the dense volume within the emerging field in the PI case has expanded more both vertically and horizontally. In the FI case, the dense and cool material stays at 2-4 Mm above the photosphere. The temperature distribution shows no heating under the expanding flux system in the PI case at $t = 69.52$ min, whereas in the FI case, heating occurs in the central region ($x = 0$, $y = 0$), right below the new FR. This heating becomes more pronounced at $t = 81.11$, concentrated in a Y-shaped area beneath the cool and dense rising plasma. In contrast, there is no significant heating in the PI case at this time. This suggests two key differences between the FI and PI cases: the magnetic field structure within the emerging volume differs, and low atmosphere reconnection, which locally heats the plasma, only occurs in the FI case. The next subsection will elaborate on these differences. Additionally, examining the temperature distribution between the rising field and the apex of the emerging field, the local plasma temperature is higher in the PI case. At this stage, the plasma density inside the rising field is higher in the FI case (e.g., last panel, fourth row) compared to the PI case (e.g., third panel, fourth row). This aligns with

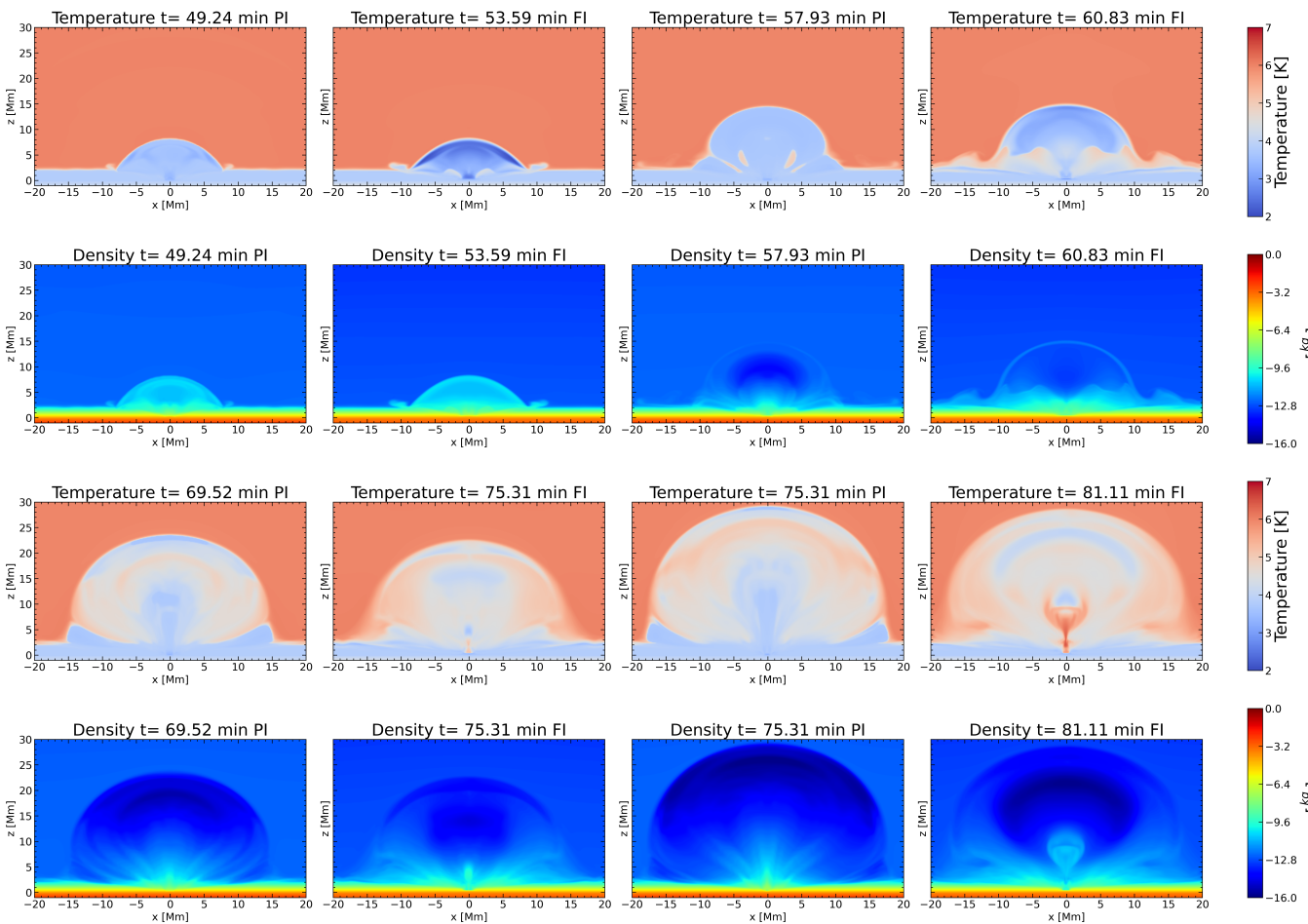


Figure 4.1: Contour plots that depict the logarithm of the temperature and density in 4 times on both simulations. The plots represent the early evolution of the magnetic loop to the solar atmosphere at the xz midplane. At four different times the apex of the tubes is located at the same height in both simulations.

the results of Chapter 3 based on the slippage effect. In a forthcoming subsection, it will be shown that, later in the evolution, the inside rising field erupts ejective in both cases.

4.1.2 Topology of fieldlines and height-time profile.

To understand better the internal structure of the magnetic field emerging above the photosphere, we trace fieldlines at three different times up to just before the first eruption. This is illustrated in Figure 4.2. In all snapshots, fieldlines are traced from the central vertical line at $(x,y) = (0,0)$ from the photosphere up to $z = 30$ Mm. The FI case is shown in the first column, while the PI case is in the second column of Figure 4.2. It is important to note that in Chapter 3 indicated that the axis of the twisted emerging flux tube in FI rises above the photosphere and remains there throughout the evolution of the system. Conversely, in the PI case, the axis of the emerging field stays below the photosphere during the simulation. This finding aligns with the results of Leake & Linton (2013) in a similar numerical experiment. In the first row, the fieldlines depict the emergence of the field into the corona before the formation of a new FR. The horizontal slice displays the distribution of B_z at the photosphere, with white indicating positive polarity and black indicating negative polarity. A notable difference between the two cases is the shape of the fieldlines, which collectively form the 3D structure of the field. In the lower atmosphere of the FI case, the fieldlines have a more horizontal orientation, connecting the two polarities. These fieldlines are part of the field near the axis of the emerging field that has risen above the photosphere. At higher altitudes, the fieldlines form an expanding, fan-like shape, as seen in many previous studies. In the PI case, the low-lying fieldlines above the PIL are less horizontally oriented and more stretched upwards, forming an arcade-like structure at all heights, connecting the positive and negative polarities of the emerging bipole. This is because the axis of the emerging twisted flux tube is below the photosphere, so the fieldlines above the axis that manage to emerge above the photosphere are visible in this panel.

In the second row, the fieldlines are shown just before the first eruption. In the FI case, several twisted fieldlines appear above the PIL, formed by the reconnection of sheared fieldlines as detailed in previous studies (Manchester et al., 2004; Archontis & Török, 2008; Syntelis et al., 2017; Leake et al., 2022). These new fieldlines create

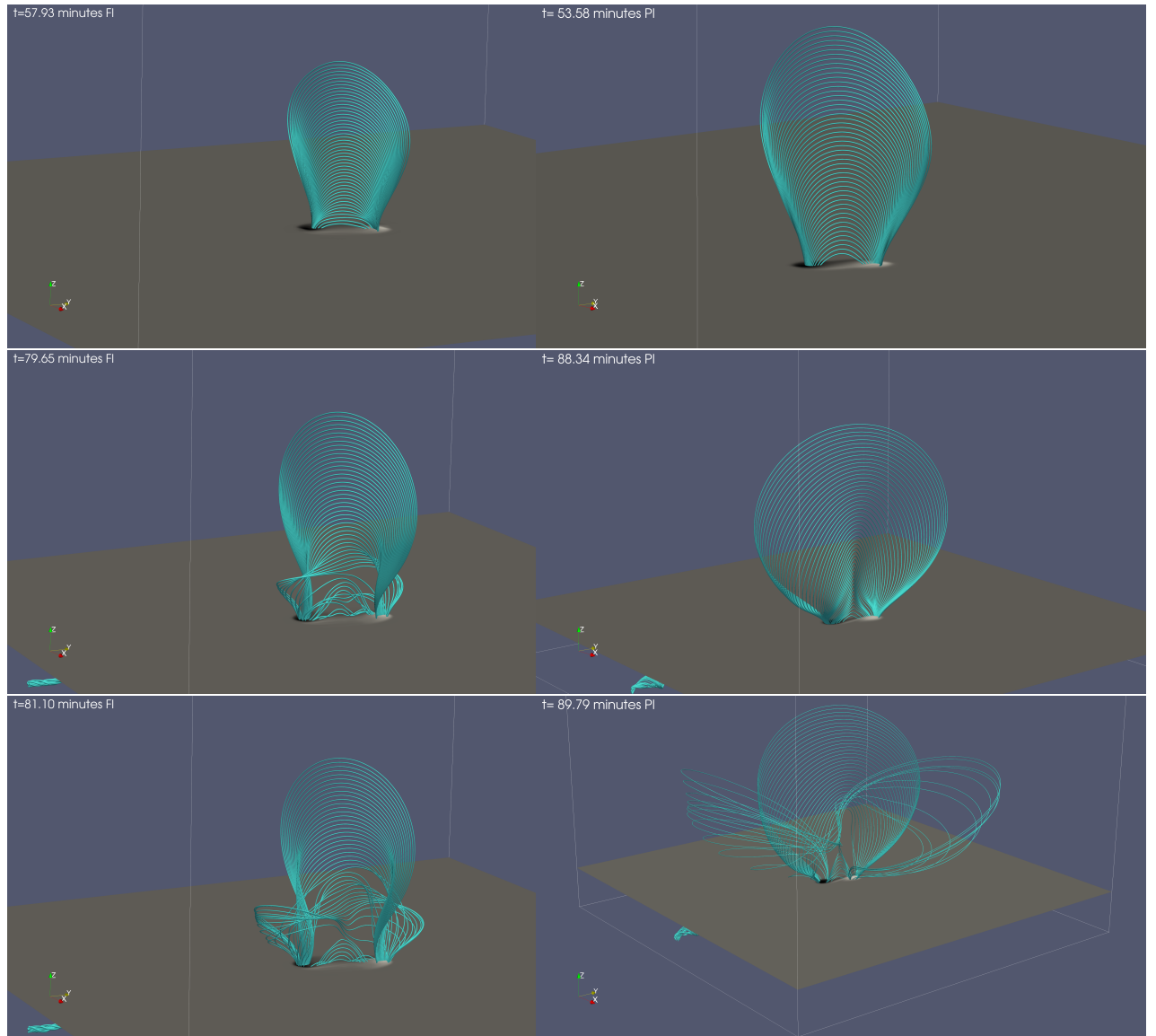


Figure 4.2: 3D magnetic field line topology for both simulations with traced magnetic field lines along a vertical line at the centre of the box. The left column represents the FI simulation and the right column represents the PI.

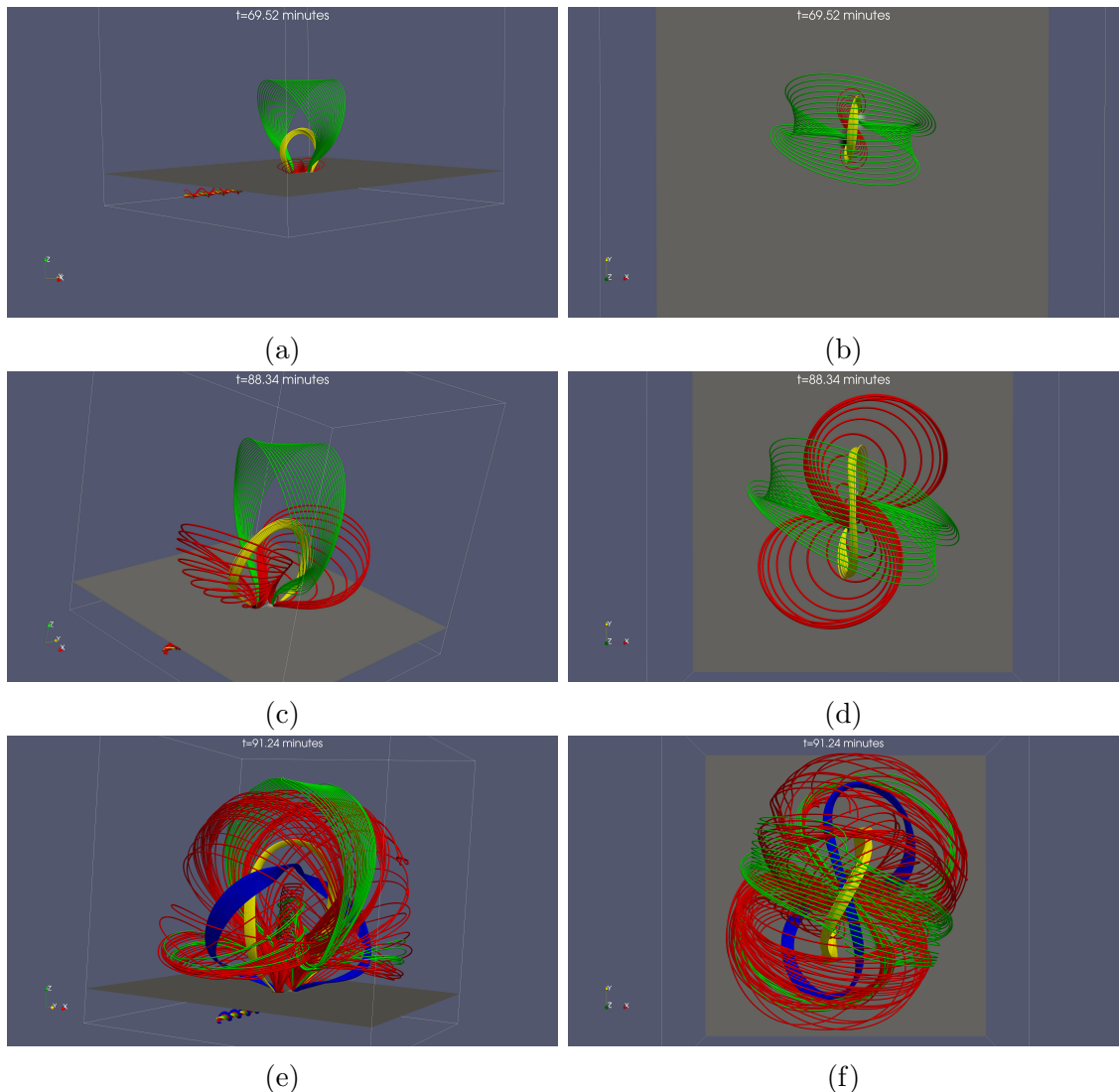


Figure 4.3: Field line morphology of the first eruption in PI simulation at (a,b) $t=69.52$ minutes side and top view (c,d) $t=88.34$ minutes side and top view and (e,f) $t=91.24$ minutes side and top view.

the FR, oriented along the y -direction, which will erupt later. In the PI case, the field continues to expand, and the central part shows upward stretching as the footpoints connect down to the photosphere without undergoing reconnection. The upward stretching occurs because the plasma behind the apex of the emerging field moves faster than the apex itself, causing vertical stretching of the fieldlines at the centre. At this stage of evolution, it is evident that the structure of the emerging field is significantly different in the two cases. In the FI case, a FR has already formed and is rising, while in the PI case, the magnetic field adopts an arcade-like configuration.

In the third row, the flux rope in the FI case has reached coronal heights and begun to erupt at a higher speed. In the PI case, we observe reconnection for the first time between field lines that have expanded at the two flanks of the emerging field. These field lines reconnect at the centre of the emerging volume (around $x = 0, y = 0$) at coronal heights. Reconnection between similar field lines continues at progressively higher altitudes, leading to the formation of a FR that will eventually erupt ejective. The mechanism for the FR formation in the FI case is similar to those described in previous experiments (e.g., Manchester et al. (2004); Archontis & Török (2008); Syntelis et al. (2017); Leake et al. (2022)). To study the FR formation mechanism in the PI case, we show the evolution of the magnetic field lines from various locations in the 3D space during the field's emergence.

Figure 4.3 visualizes magnetic field lines in 3D at three different times (top row: $t = 69.52$ minutes, middle row: $t = 88.34$ minutes, and bottom row: $t = 91.24$ minutes). In the top row, green field lines represent the apex of the emerging field. The yellow field lines are traced from the vertical xz mid-plane at a height where the magnetic field is primarily oriented along the y -direction and where the B_x component changes sign from negative to positive. Red field lines are traced from the photosphere around the centre ($x = 0, y = 0$) from the two opposite polarity sides of the PIL. At this stage, the red field lines are not connected to each other. The top view (top right panel) shows that each set of red field lines has a J-like shape. The middle row shows field lines traced from similar locations at later times. It is important to note that these are not the same field lines as those visualized at the earlier stage (top row). However, they show that the overall expansion of the field and that the J-like field lines have not yet reconnected but their footpoints get closer over time, adopting a more vertical configuration. Between the vertical footpoints

of the two J-like sets of field lines, a strong current sheet forms, and reconnection between the J-shaped lines will occur soon. In the bottom row of Figure 4.3, we show the field line topology after the J-like field lines have reconnected. The blue field lines are new field lines formed after the reconnection, adopting an overall S-like shape (top view). The yellow field lines are now traced from a height between the new reconnected field lines (blue) and the apex of the emerging field (green). At this stage, a new FR is formed, which will also erupt into the outer atmosphere, similar to the FI case. The core of the new FR consists of the blue field lines. Field lines twisted around the core of the FR are present above and behind it. For example, some low-lying red field lines are wrapped around the flanks of the core field lines of the FR. Note that the reconnected field lines (blue) in the bottom row of Figure 4.3 are essentially the same as the reconnected field lines shown in the bottom right panel of Figure 4.2.

We have not specifically studied the origin mechanism of the eruption(s) in the PI case, but we expect that the tether-cutting reconnection of the J-like fieldlines contributes to releasing the downward tension of the envelope fieldlines (above the yellow fieldlines) and gradually initiates the fast eruption of the magnetic field. The mechanism for eruptions in the FI case is similar to that described by Syntelis et al. (2017). The time evolution of the erupting magnetic field's height is shown in Figure 4.4. We track the rising plasma in the vertical xz-midplane with the following characteristics: a) the azimuthal magnetic field component (B_x) is zero at that height, and B_x changes sign above and below it, b) the magnetic field is primarily directed along the y-direction, and c) the fieldlines passing through this height have their photospheric footpoints at the maximum values (positive and negative) of B_z at the two main polarities of the emerging field. This plasma element appears to be close to the core of the erupting field. In both cases, there is a slow rise phase followed by a fast rise phase, where the height increases exponentially over time. These height-time profiles strongly suggest that the erupting field in both cases reaches the outer solar atmosphere. There are two main differences between the cases. In the PI case, the slow rise phase lasts longer (up to around $t = 90$ min) and the fast rise phase begins at a higher altitude, around $z = 22$ Mm compared to $z \approx 6$ Mm in the FI case. To link the height-time profile with the dynamics of the erupting field's motion, we will study the velocity profiles of the rising magnetized plasma in the next subsection.

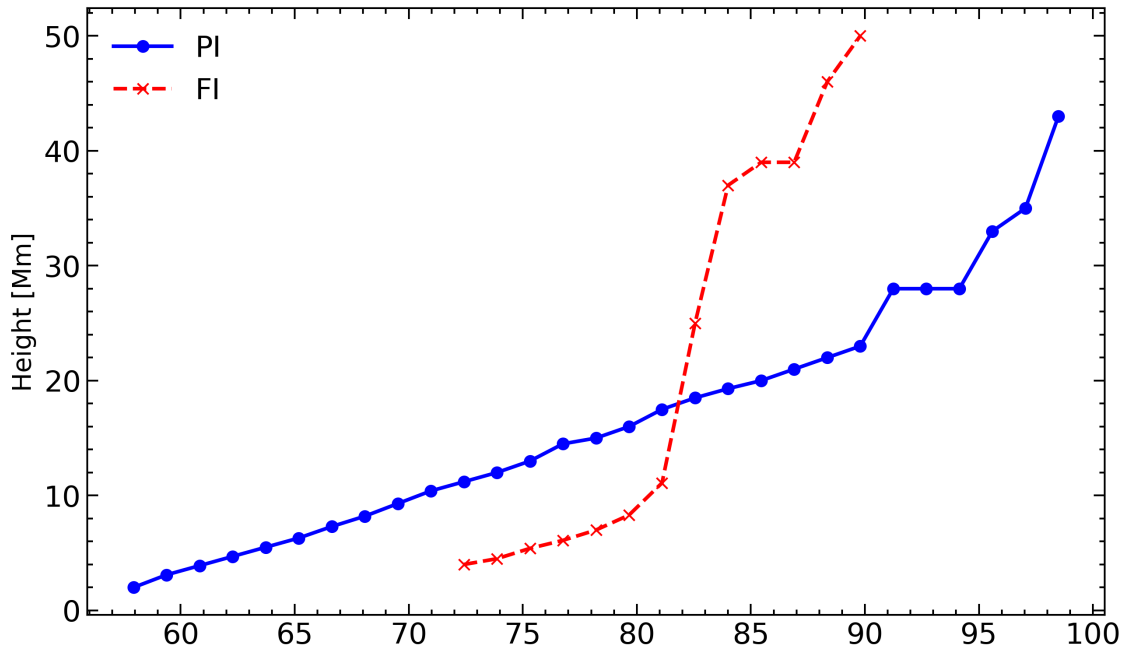


Figure 4.4: Height time profile of the internal rising plasma in both simulations. The slow rise phase is prolonged in the PI case.

4.1.3 The rising motion of the erupting field

Figure 4.5 shows the distribution of V_z along height at the centre of the computational domain above the photosphere. We have selected three times. The first and second columns show V_z before the eruption, and the third column shows V_z during the eruptive phase in both cases.

In the FI case, at $t = 53.59$ minutes, the apex is located at $z \approx 8 - 9$ Mm. This represents the early stage of the field's emergence above the photosphere, with the plasma at the apex and inside the emerging field moving at a similar speed, $V_z \approx 20$ km/sec. At $t = 60.83$ minutes, the emerging field expands further into the corona, and the apex reaches $z \approx 14 - 15$ Mm, moving faster than the heavier plasma behind it. At $t = 81.1$ minutes, the apex has reached $z \approx 30$ Mm, but the plasma inside the emerging field is now moving faster than the apex. Specifically, at $z \approx 9 - 10$ Mm, there is a local maximum in V_z , indicating that this plasma is moving faster than any other plasma above it. This fast-moving plasma is the central part (around the core) of the erupting field. Below the erupting field, there is a strong bi-directional V_z flow due to reconnection, leading to the formation of the flux rope, which eventually erupts.

In the PI case, the rising motion of the erupting field shows some differences. At the early stage of emergence, at $t = 49.24$ min, the plasma between $z \approx 4.5 - 7$ Mm is moving faster than the apex ($z \approx 8 - 9$ Mm). The faster-moving plasma inside the emerging expanding volume is less heavy compared to the apex, thus rising with higher speed. As time progresses, the apex reaches $z \approx 14 - 15$ Mm, and the plasma behind continues to rise with higher speed. At this point, the amount of plasma rising faster than the apex is larger, extending from $z \approx 4.5 - 13$ Mm. This occurs because the arch-like structure of the magnetic field stretches upwards, causing most of the plasma behind the apex to move faster. The plasma behind the apex moves faster in the PI case because the magnetic field emerges with an arch-like shape, allowing the heavier plasma to drain more effectively along the curved fieldlines due to gravity. In the FI case, the concave dips of the twisted fieldlines of the FR can carry more heavy plasma upwards. It is worth mentioning that in Figure 4.1, we found heating of the plasma behind the apex of the emerging field. This heating occurs because the plasma is compressed at the interface between the faster-moving plasma of the interior and the slower-moving plasma of the apex. At this stage, there is no reconnection at the lower parts of the arch-like field. However, at $t = 95.59$, reconnection occurs at $z \approx 11.5$ Mm, creating a bi-directional reconnection flow with a maximum upward speed of $V_z \approx 580$ km/sec. At this stage, the emerging field has an overall flux rope-like configuration, undergoing an eruptive phase.

4.1.4 The first eruption

To further study the first eruption in the FI and PI experiments, we visualize the temperature, density, and vertical velocity when the "central" part of the erupting field is in the fast eruptive phase, and the apex of the emerging field in both experiments has reached similar heights. This is shown in Figure 4.6. The vertical velocity (first column in Figure 4.6) shows a strong upflow at the centre of the domain, extending from $z \approx 6 - 8$ Mm to the high corona, up to the vicinity of the "central" part of the erupting flux system. This represents one part of the bi-directional reconnection flow occurring at the current sheet beneath the erupting magnetic field. The other part is a downflow (faint blue color) that impacts the heavier plasma at lower atmospheric heights. The downflows at the low edges of the expanding field (e.g., at $x = -20$ Mm, $x = 20$ Mm, and $z = 4 - 6$ Mm for PI) are due to gravitational draining of the plasma along the fieldlines from their apex

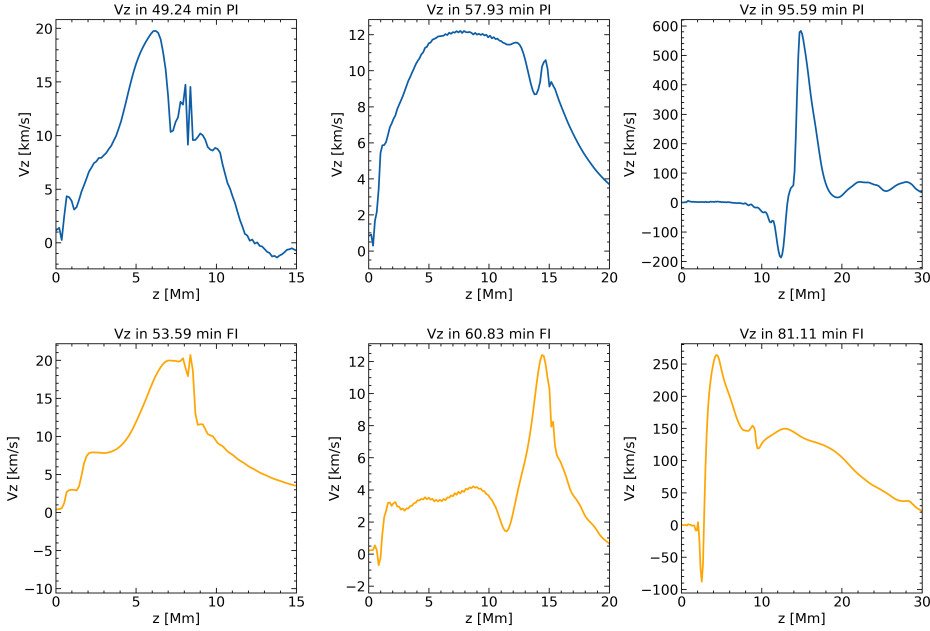


Figure 4.5: V_z distribution in the centre of the box along height for both simulations that depict the rising motion of the IRFS before the solar eruption (first and second columns) and at the eruptive phase (third column).

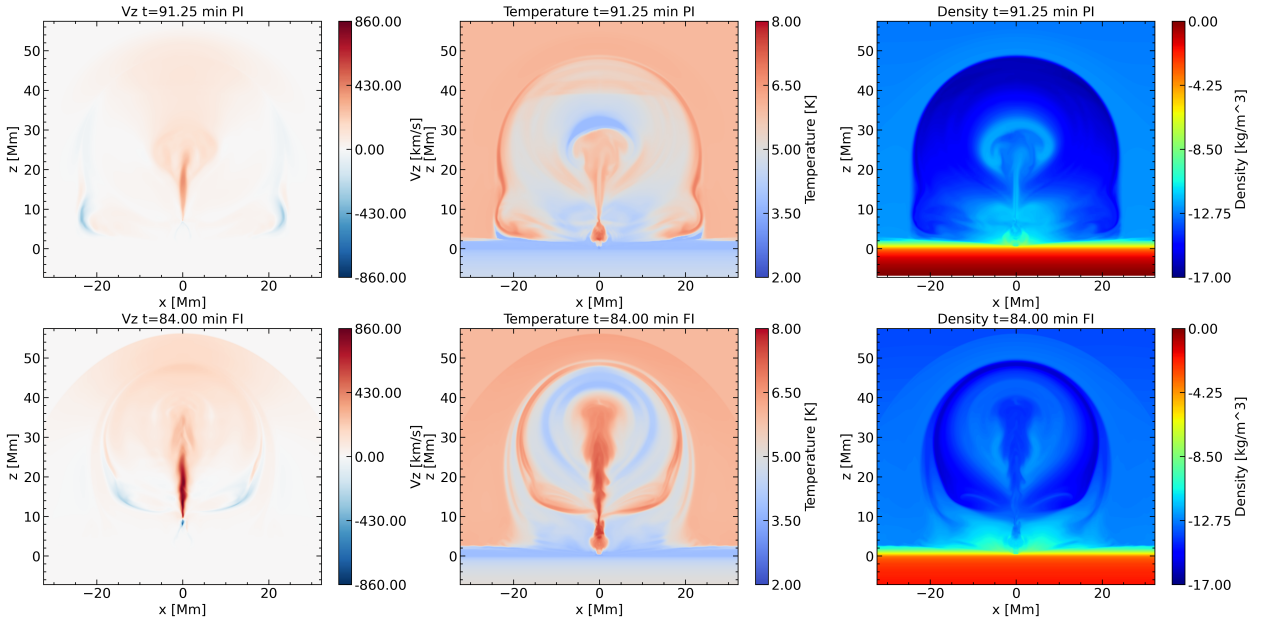


Figure 4.6: Contour plots that depict the v_z profile (first column), the logarithm of temperature (second column) and the logarithm of density (third column) in both simulations at the xz midplane. The contour plots are in times that capture the onset of the first solar eruption.

towards their footpoints.

The temperature distribution reveals that the reconnection outflows are hot, as anticipated, creating a mixture of cool and hot plasma within the expanding volume of the emerging field, with temperatures ranging from 10^4 to 10^7 K. The density distribution (third column) aligns closely with the temperature distribution in both scenarios. When observing the density distribution alone, it is evident that the central part of the erupting field in the PI case, at this stage and at coronal heights, contains denser plasma. However, over the entire evolution of the magnetic flux system in our simulation, the average density emerging or ejected into the corona (during eruptions) is higher in the FI case. Differences in vertical velocity (e.g., higher in the FI case) and temperature arise because the FI eruption is well into the fast rise phase (Figure 4.4) at this point, while the PI eruption is just entering this phase.

4.1.5 Energy evolution during eruptions

Figure 4.7 contains two panels. The first panel depicts the time evolution of the average value of B^2 at $z = 40$ Mm in the xy plane, normalized by the average value of B^2 in the subphotospheric tube at $t = 0$. The second panel illustrates the temporal evolution of the average value of ρv_z^2 at the same height in the xy plane. The right panel shows three local maxima in both PI and FI cases. In the FI case, the first peak occurs between $t = 80$ and $t = 90$ minutes, corresponding to the reconnection outflow that triggers the first eruption. In contrast, this event occurs in the PI case between $t = 100$ and $t = 110$ minutes. The second peak in FI, occurring between $t = 100$ and $t = 110$ minutes, corresponds to the reconnection outflow that initiates the second eruption. The third peak in FI, indicating the start of the third eruption, occurs between $t = 140$ and $t = 150$ minutes.

Meanwhile, in PI, the second peak occurs between $t = 115$ and $t = 130$ minutes, corresponding to the reconnection outflow that marks the onset of the second and strongest eruption. The third peak in PI, occurring between $t = 160$ and $t = 180$ minutes, corresponds to the third eruption. As discussed in previous sections, there is a slight time difference in the occurrence of emergence and eruptions between the PI and FI cases. The actual emergence into the corona happens slightly earlier in the PI case, while the formation of the new FR that eventually erupts into the

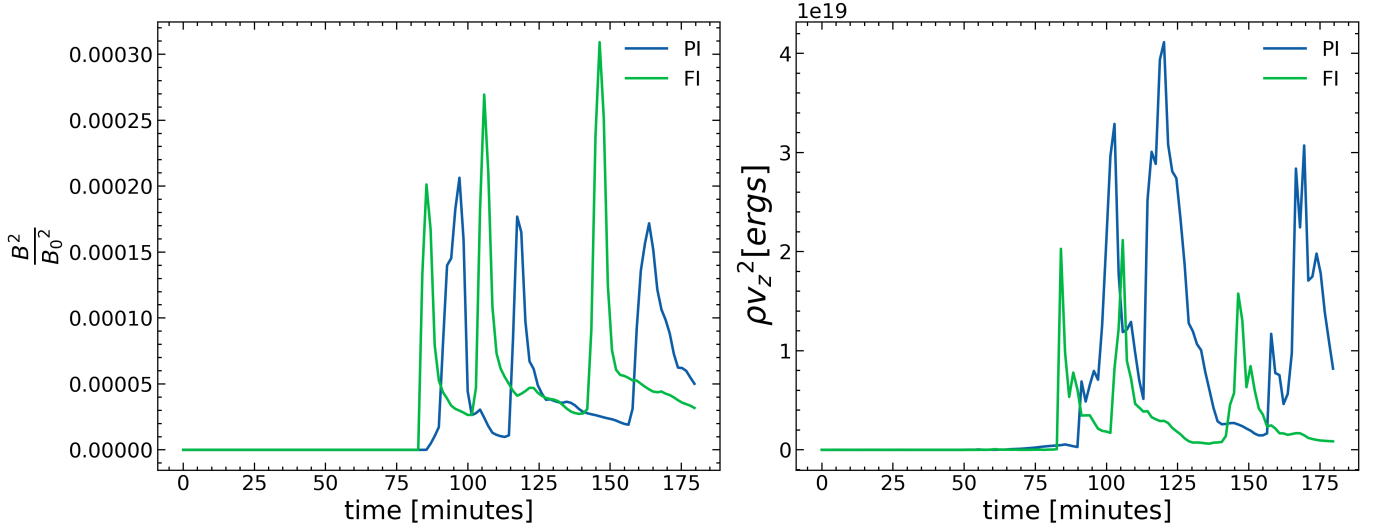


Figure 4.7: Comparison of the average values of normalized B^2 at 40Mm height (left panel) and ρv_z^2 at the same height (right panel) in both simulations.

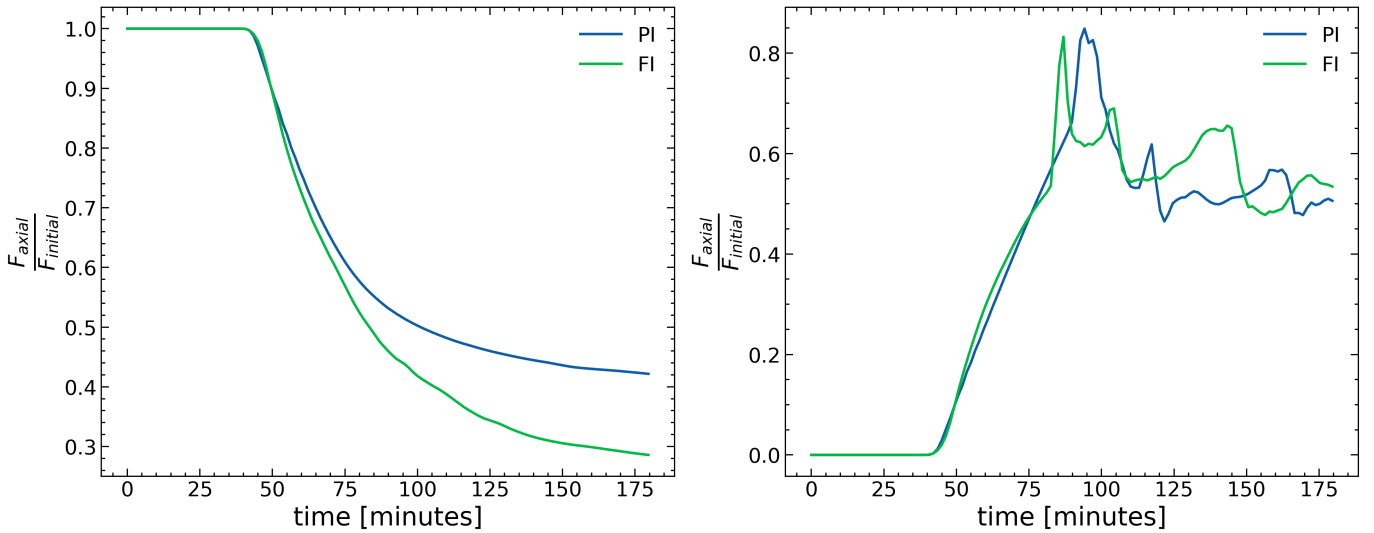


Figure 4.8: Comparison of the normalized axial flux below photosphere (left panel) and above photosphere (right panel) in both simulations.

corona occurs earlier in the FI case. Observing the left panel in Figure 4.7, we find that B^2 reaches three local maxima just before the peaks in kinetic energy. This occurs because, with each eruption, the strong magnetic field of the erupting FR reaches the corona first, followed by the strong vertical reconnection upflow originating from the vertical current sheet behind the FR. Thus, there is a small delay between the maxima of B^2 and the kinetic energy peaks. Another interesting result is that the normalized B^2 is overall higher in the FI case, indicating that the

FI eruptions consist of stronger magnetized plasma.

This is because, as discussed in Chapter 3, a stronger magnetic field, including the axis of the emerging flux tube, rises above the photosphere in the FI case, whereas in the PI case, the strong axial magnetic field does not emerge above the photosphere. Observing the right panel in Figure 4.7, we find that plasma acceleration during eruptions in the FI case is lower compared to the PI case. This is due to the larger value of V_z in the FI case. The primary component of the vertical velocity V_z is the reconnection upflow, which follows the core of the erupting FR. The reconnection leading to the formation of the erupting FRs occurs at different heights in the two cases. In the FI case, it occurs in the low atmosphere (chromosphere/transition region), whereas in the PI case, it happens in the corona. Since the reconnection outflows move at speeds close to the local Alfvén speed, which is higher in the corona, the kinetic energy of the eruptions is higher in the PI case.

We now focus on the distribution of axial flux below the photosphere and in the corona during the simulation. Specifically, we calculate $F_{\text{axial}} = \iint B_y dx dz$ at the vertical xz-midplane at $y = 0$. These values are normalized with the initial flux at $t = 0$ for two distinct regions: below the photosphere (left panel in Figure 4.8) and above the photosphere (right panel). In the PI simulation, a significant portion of the axial flux remains subphotospheric, aligning with findings from Chapter 3 where the flux tube's axis does not fully emerge at the solar surface.

By the end of the simulation, the normalized axial flux in the PI case converges to about 40%, while in the FI case, it converges to just below 30%. Above the photosphere (right panel in Figure 4.8), a similar evolution is observed in both cases, with the flux reaching three local maxima at times just before the eruptions. This suggests that the erupting structures have a significant axial field (B_y) component, consistent with the results in subsection 4.1.2, where we traced the fieldlines before and after the first eruption, showing that the erupting field adopts a FR configuration with fieldlines directed along the y-axis at the core.

The local increase in normalized axial flux is related to the formation of new flux ropes, which eventually erupt into the outer solar atmosphere. Overall, the normalized axial flux above the photosphere is higher during the first eruption and gradually decreases over the simulation. This may indicate that subsequent eruptions do not have the exact structure of the first eruption. Another interesting finding

is that the normalized axial flux values vary within a similar range throughout the simulation. For example, the first maximum is close to 0.85, and it approaches saturation towards the end of the simulation, with a value of about 0.5. Thus, in both experiments, the amount of normalized axial flux in the corona does not differ dramatically over the entire simulation. Further investigation is needed to study both the structure of the erupting field (see e.g., Moreno-Insertis & Galsgaard (2013)) and the evolution of the associated axial flux.

4.1.6 Neutrals, emergence, and eruptions

In this subsection, we examine the evolution of the neutral fraction during the emergence and the first eruption in the PI case. Figure 4.9 displays three columns: neutral fraction, temperature, and density (from left to right) at the vertical xz -midplane of the numerical domain at four different times.

In the first row, the temperature distribution reveals three notable areas within the emerging volume: a top arch-like layer with cool plasma, a middle/central column with cool plasma, and an interface layer between them with much higher temperatures. This stage of evolution was previously discussed in Figure 4.1, where it was noted that the less dense, rising plasma within the expanding volume moves faster, compressing the plasma above it and causing heating at the interface. Now, we find that the neutral fraction is higher in both low-temperature areas: at the arch-like front and in a vertical column at the centre ($x=0, y=0$) of the domain. This neutral column extends along the y -direction along the polarity inversion line of the emerging bipolar field. It is important to note that this column of neutrals lies between the footpoints of the J-like fieldlines, similar to the red fieldlines in the top row of Figure 4.3, which will eventually reconnect to form the erupting flux rope.

As time progresses (second and third row in Figure 4.9), the entire emerging volume expands laterally, while the faster-moving plasma continues to rise, further compressing the material above and increasing its temperature. Consequently, neutrals persist only in the vertical middle column where the plasma remains cool and dense. Notably, the lower part of this column becomes thinner. This thinning occurs because the oppositely directed magnetic field (J-like fieldlines) near the column on the left (negative x -axis) and right (positive x -axis) sides gradually approach each

other, forming a strong and thin current sheet where the local temperature increases. During this process, dense low-atmospheric plasma (around $x=0$, $y=0$) is brought up, loading part of the neutrals column with heavy material.

At $t = 89.80$ min (third row), reconnection between the J-like fieldlines has already begun. The temperature distribution shows the cool area of the internal magnetic field and the hot reconnection plasma flows beneath it. The density distribution correlates well with the temperature distribution. Neutrals now exist only within the cool area of the internal magnetic field, which is erupting. A significant amount of neutrals is carried upwards into the corona, just above the hot jets. The densest neutrals are also the largest fraction. Eventually (not shown here), as the eruptive plasma rises higher, neutrals continue to exist, though in lower fractions, as they are pushed upwards by the upward reconnection jet. Neutrals disappear when the temperature within the eruptive material increases enough to prevent their existence.

4.2 Discussion

Chapter 3 focused on the effect of partial ionization on the flux tube's emergence beneath the solar surface. This Chapter extended the analysis to the structure, dynamics, and thermodynamic properties of the emergence into the solar corona and the subsequent eruptions from the emerging bipolar region.

In Chapter 3, we demonstrated that the tube's axis remains below the photosphere in the PI simulation. Here, we show that the emerging field above the photosphere consists of arch-like fieldlines with little or no twist. After expanding into the outer solar atmosphere, reconnection between J-like fieldlines occurs at the central part of the domain and at coronal heights. This reconnection leads to the formation of a new flux rope, which eventually erupts. Therefore, the topology of the fieldlines, the structure of the emerging field, and the process leading to the formation of an erupting FR differ significantly between the PI and FI cases. In the FI cases, the axis of the original twisted flux tube emerges above the photosphere and remains there for the rest of the simulation. Sheared fieldlines from this tube experience reconnection at the PIL of the emerging region, forming a new FR that erupts into the corona.

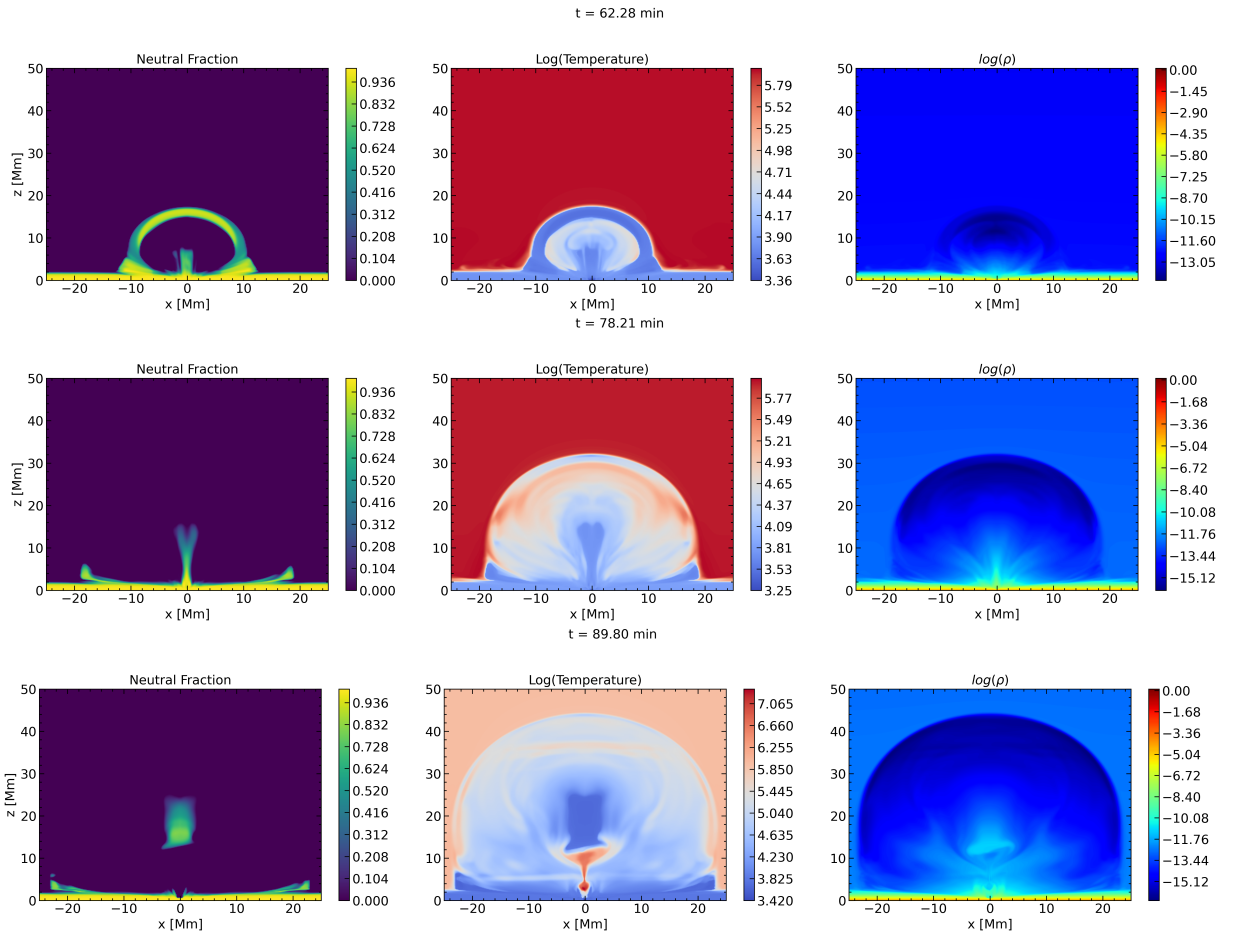


Figure 4.9: Contour plots of the Neutral fraction, the logarithm of the temperature and the logarithm of the density in the xz mid plane in various snapshots that display the evolution of the neutral atoms in the simulation.

We confirmed the findings of Leake & Linton (2013) that the plasma inside the expanding magnetized volume in the PI simulations is less cool than in the FI simulation due to ion-neutral collisions, which reduce the intensive cooling from adiabatic expansion. Additionally, the plasma inside the expanding volume and below the apex of the magnetic field is less dense in the PI simulation compared to the FI simulation and rises faster than the apex. Consequently, the plasma just below the apex is compressed, increasing its temperature. Thus, the temperature and density distributions inside the expanding magnetic field differ between the two cases.

During our simulations, we observed three major eruptions following the expansion of the emerging field. The normalized axial flux remaining below the photo-

sphere is less in the PI case, consistent with the previous results. However, the normalized axial flux above the photosphere is similar in both simulations. Further detailed analysis is needed to understand this result, likely related to the formation mechanism of the eruptions and the flux they carry during their formation and ejection. We calculated the average values of normalized B^2 and ρv_z^2 in the high corona and found local maxima of these quantities during the eruptions. Overall, in the PI case, the local maxima are lower for B^2 and higher for ρv_z^2 . This indicates that the PI eruptions consist of weaker magnetized plasma (relative to the initial magnetic field of the sub-photospheric tube) and are faster by a factor of two.

For the first eruption in the PI case, we found a thin column of neutrals in the central region of the domain, extending from the PIL to the low corona, where the plasma is cool and relatively dense. A strong current sheet eventually forms in this area, and reconnection of J-like fieldlines creates the first FR that erupts into the outer solar atmosphere. The reconnection upflow at the current sheet pushes a fraction of the neutrals upward along with the newly formed FR. The hot reconnection flows increase the plasma temperature near the erupting FR, reducing the number of neutrals in the high atmosphere.

In our simulations, the emergence occurred into a null corona. It is well known that emergence into a magnetized atmosphere can lead to the formation of solar jets, triggered by reconnection or driven by eruptions Raouafi et al. (2016). In the next chapter, we will examine the effect of partial ionization on the structure and thermodynamic properties of jets in the solar atmosphere.

Chapter 5

Effects of partial ionization on solar jets.

In chapters 3 and 4, we presented the results of the PI and FI simulations. A key characteristic of these simulations is the unmagnetized state of the solar atmosphere, a simplification from reality that allows us to focus on the intrinsic properties of the emerged and expanded magnetic loop. This approach enables us to identify the distinct effects of partially and fully ionized plasmas to the emergence of a magnetic flux system and the subsequent dynamics of the solar eruptive events. Understanding these differences in a simplified experimental setup will guide our expectations for more complex scenarios. Such a complex scenario, which we will explore in this chapter, involves magnetic flux emergence in a magnetized solar atmosphere.

In the introductory chapters, we noted the significance of solar jets in solar physics through both observations and theoretical simulations. According to Moore et al. (2010b), jets associated with magnetic flux emergence are categorized as standard jets and blowout jets. When the magnetic flux region reaches the solar surface, it interacts with the ambient magnetic field, generating a strong current and creating a current sheet. The first interaction of the emerged flux system with the ambient one will create the standard solar jets (e.g. Shibata et al. (1992); Shibata & Tanuma (2001)). The emerged magnetic field forms a PIL, and the converging and shearing motions subsequently create a FR as we stressed in previous chapters. This FR, propelled by both internal and external reconnection, travels towards the solar

atmosphere, producing both cold and hot jets. This process was first explained by Moore et al. (2010b) and further described numerically by Archontis et al. (2013) and Moreno-Insertis & Galsgaard (2013). In this chapter, we investigate the impact of partially ionized plasma on the formation and characteristics of both standard solar jets and eruption-driven jets.

5.1 Numerical Setup

The numerical setup, in terms of the equations solved, remains the same as in our previous simulations featuring the unmagnetized solar atmosphere. In this study, we again conduct two simulations: one assuming a fully ionized plasma (FI) and the other assuming a partially ionized plasma (PI), both with the same initial plasma beta. The primary difference in this experiment lies in the solar atmosphere and the ambient magnetic field configuration, which was absent in the previous experiment. To simulate the environment found in solar coronal holes, we used a uniform unipolar magnetic field.

The magnetic field configuration employed in both simulations is as follows:

$$\begin{aligned} B_x &= b_{\text{cor}} \sin(\theta) \cos(\phi), \\ B_y &= b_{\text{cor}} \sin(\theta) \sin(\phi), \\ B_z &= b_{\text{cor}} \cos(\theta). \end{aligned}$$

Here, b_{cor} represents the magnitude of the ambient field, which in our case is $b_{\text{cor}} = 9.9G$. The angle θ is defined as the angle between the z-axis and the magnetic field vector. For instance, if $\theta = 0$, then the magnetic field B is parallel to the z-axis. The angle ϕ is defined as the angle between the x-axis and the projection of B onto the xy-plane, denoted as B_{xy} . Therefore, if $\phi = 0$, then B is parallel to the x-axis. The initial conditions in a 3D representation are depicted in Figure 5.1.

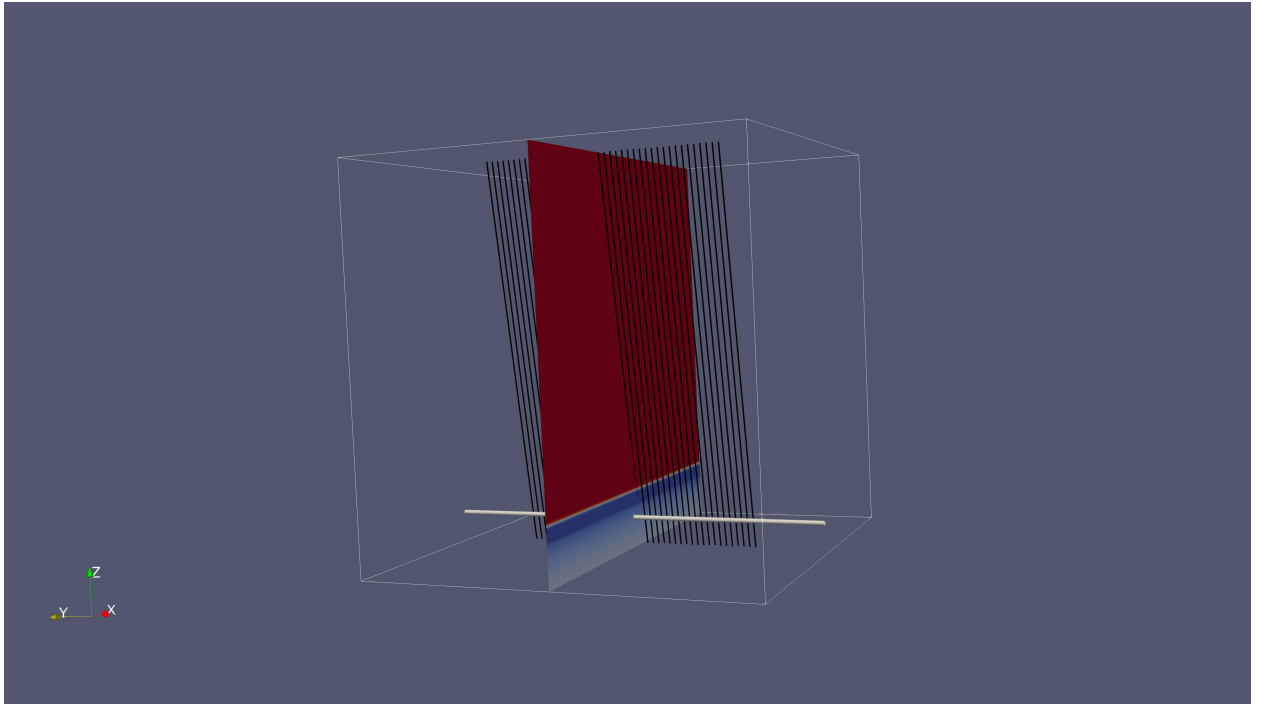


Figure 5.1: 3D representation of the initial setup of our FI and PI simulations with the unipolar ambient magnetic field (black field lines) and the isosurface of the maximum B_y which is the axial component of the magnetic field of our TFT(white contour). The xz midplane contour depicts the temperature distribution.

In our PI and FI we used the same θ and ϕ angles for the orientation of the ambient field with 11 and 183 degrees respectively.

5.2 Results

5.2.1 The Emergence of the Magnetic Flux to the solar surface.

The two simulations conducted share the same physical characteristics as those presented in Chapters 3 and 4. Consequently, the emergence of the TFT at the solar surface, along with the subsequent differences between the PI ,FI plasmas observed in previous experiments, are expected to be consistent even with the introduction of a unipolar ambient magnetic field. The magnitude of the ambient field is relatively weak and does not alter the results presented in the earlier chapters.

5.2.2 The comparison of the kinetic energy budget of the solar eruptive events.

To assess the number and dynamic impact of eruptive events in our simulations, we calculated the kinetic energy above corona for both simulations associated on the ν_z component. The kinetic energy was computed using the following formula:

$$E_{kinetic} = \frac{1}{2} \int_x \int_y \int_{3.2Mm}^{z_{end}} \rho \nu_z^2 dz dy dx \quad (5.1)$$

we displayed the results in figure 5.2.

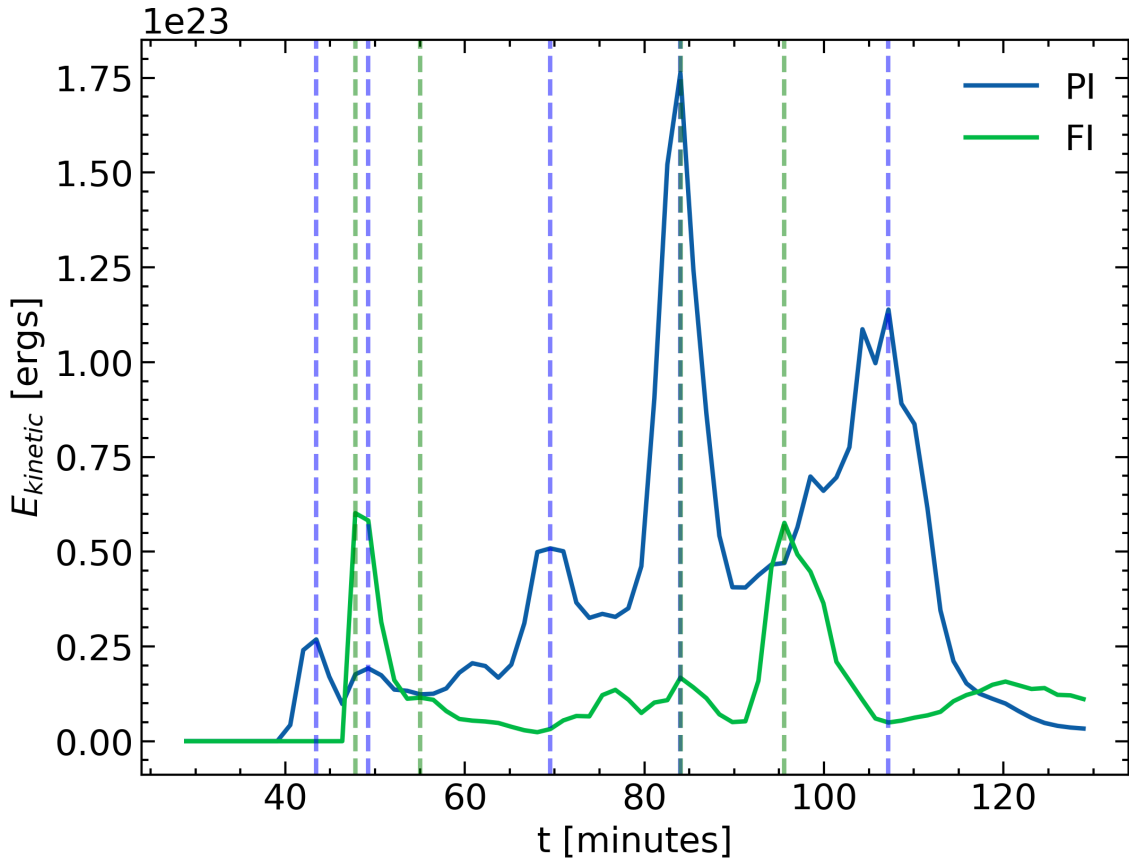


Figure 5.2: The temporal evolution of the kinetic energy above corona for both simulations. Every simulation has eruptive events marked by the vertical lines (blue for the PI and green for the FI simulation).

In both simulations, we observe local maxima in the kinetic energy, signaling

eruptive events. The initial peak corresponds to the first reconnection between the emerged flux system and the ambient magnetic field, leading to the creation of a standard jet. Similarly, the second peak in both simulations indicates the formation of another standard jet. We will provide more detailed observations of these jets later. As detailed in Chapter 3, the first apex expanding through the solar atmosphere originates from the PI simulation, leading to the first standard jet at $t = 44$ minutes with a kinetic energy of $E_{\text{kinetic}} = 2.5 \times 10^{22}$ ergs, marked by the first blue vertical line in Figure 5.2. In contrast, the standard jet in the FI simulation occurs at $t = 47.79$ minutes, with $E_{\text{kinetic}} = 6 \times 10^{22}$ ergs. This indicates a more energetic standard jet in the FI simulation, ejecting plasma with nearly 2.5 times more kinetic energy than the PI simulation. The second standard jet in the PI simulation occurs at $t = 49.24$ minutes, shortly after the first jet, ejecting plasma with kinetic energy of $E_{\text{kinetic}} = 2.0 \times 10^{22}$ ergs. This is slightly weaker compared to the first jet. In contrast, the second peak in the FI simulation is observed at $t = 55.36$ minutes, releasing $E_{\text{kinetic}} = 1.2 \times 10^{22}$ ergs, which is weaker than its first jet. Thus, the PI simulation demonstrates greater values of the kinetic energy in this instance.

Subsequent peaks observed in the PI simulation at $t = 69.52$, 84.8 , and 104.8 minutes eject kinetic energies of 5×10^{22} ergs, 1.75×10^{23} ergs, and 1.1×10^{23} ergs, respectively. These events, indicated by additional blue vertical lines, are mainly eruption-driven jets, with the PI simulation showcasing greater kinetic energy outputs. For the FI simulation, peaks occurring at $t = 84$ and 95.59 minutes release kinetic energies of 1.5×10^{22} ergs and 5.5×10^{22} ergs, respectively. This comparative analysis highlights differences in the dynamics and impact of jets between the two simulations: while the FI simulation leads in the first reconnection jet event, the PI simulation exhibits more powerful eruption-driven jets and a stronger second standard jet in terms of kinetic energy. Although there are other peaks in the plot, our focus will be on those that exhibit the most significant kinetic energy ejections, namely the two standard jets and the most energetic eruption-driven jet in both simulations.

Apart from identifying the kinetic energy budget and distinguishing the number of events, this plot does not clearly indicate whether the differences are due to higher density in the PI simulation or greater velocities.

To determine which simulation exhibits higher velocities, we computed the tem-

poral evolution of the normalized total sum of the density at the height of 40Mm in the xy-plane like this :

$$\frac{\iint \rho dx dy}{\iint \rho_0 dx dy}$$

We normalized it due to differences in the initial density profiles, the ρ_0 is the density of the plasma at this height at $t = 0$. Additionally, we calculated the temporal evolution of the maximum value of v_z at the same height and displayed the results in Figure 5.3. In the density plot, we observe that the standard jets eject more dense plasma in the FI simulation, consistent with the results of Chapter 3. For the eruption-driven jets, the FI simulation again has the upper hand in events with a significant kinetic energy budget at $t = 95.59$ minutes for FI and $t = 84.8$ minutes for PI in Figure 5.2, but in Figure 5.3, this corresponds to the peaks located at $t = 90$ minutes for PI and $t = 105$ minutes for FI. In the velocity plot, we observe numerous peaks, as there are numerous transient events occurring in our simulations. However, if we focus on the specific events (standard jets and eruption-driven jets with greater kinetic energy), we will see that except for the first reconnection jet, all other events have an enhanced velocity in the PI simulation. These two plots provide insights into the density and speed of the eruptive events in our simulations and consistently explain the peaks in the kinetic energy plot 5.2.

5.2.3 Comparison of the standard jets.

In Figure 5.2 and Figure 5.3, the first two peaks correspond to jets resulting from the initial interaction of the emerged magnetic flux system with the ambient field. These jets, resulting from the initial interaction, are termed standard jets and are the focus of this subsection. The first jet in the PI simulation occurs at $t = 43.45$ minutes, and the subsequent one at $t = 47.80$ minutes. In the FI simulation, the first jet is noted at $t = 49.24$ minutes, with the second following at $t = 55.04$ minutes. To examine the first standard jet, we produced two contour plots at these specific times, showing the logarithm of the temperature at the xz midplane, as illustrated in Figure 5.4. Observation of these two contour plots reveals differences between the jets, such as the FI jet's spire being larger compared to the PI jet's. Additionally, it appears the magnetic loop expanded more in the PI scenario up to

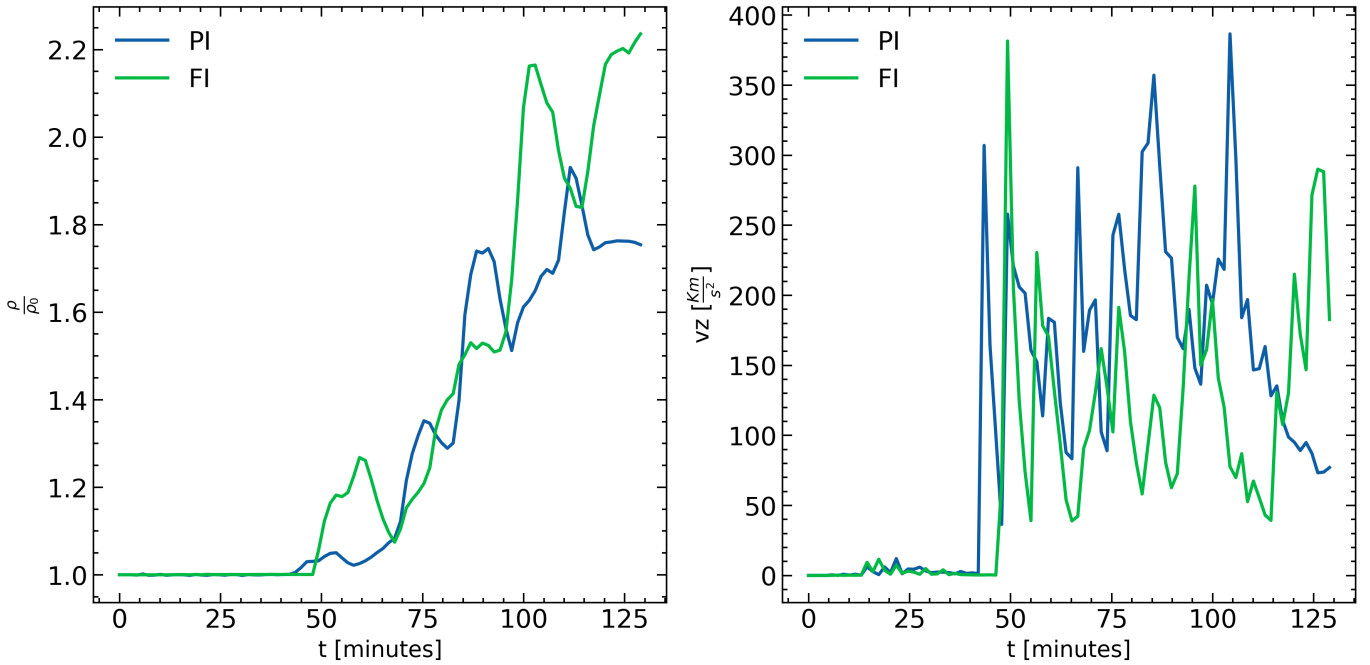


Figure 5.3: Temporal evolution of the normalized total sum of the density in both simulations evaluated at the xy plane and 40Mm height (first plot). Temporal evolution of v_z evaluated at the same height as the first plot.

the reconnection event compared to the FI. Despite these differences, the jets share similarities, including the presence of both cold and hot plasma within the spire.

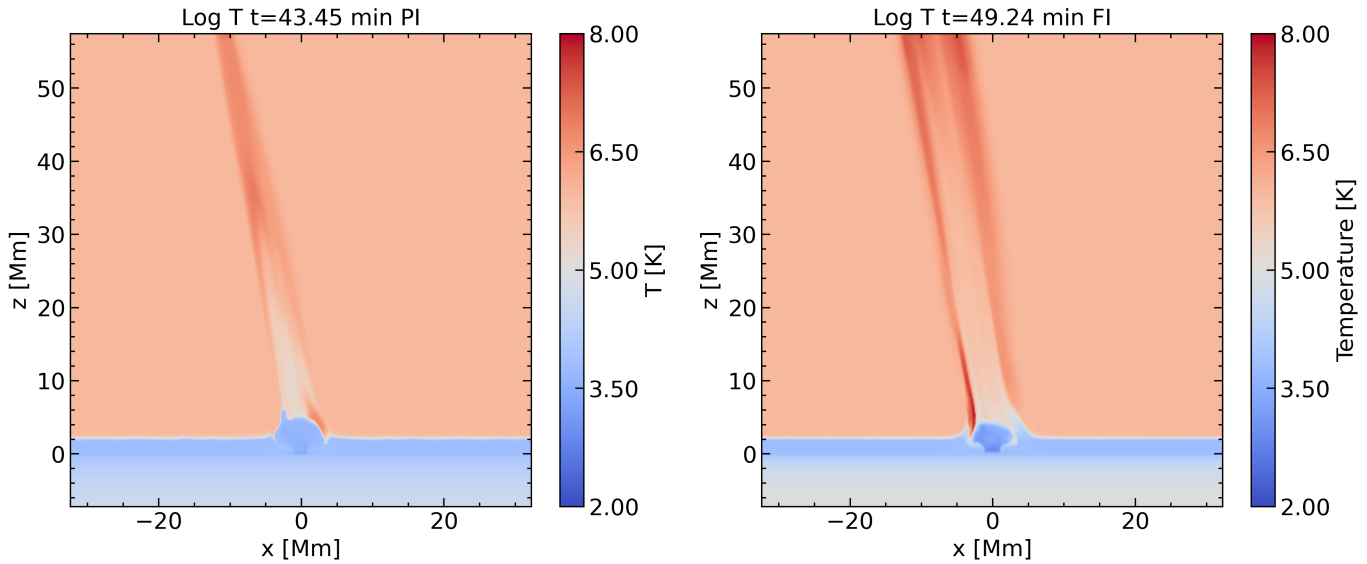


Figure 5.4: Contour plots that depict the logarithm of the temperature at times that capture the first standard jet in both simulations at the xz midplane.

In order to closely examine the jet's structure, we took a horizontal slice at a height of 20Mm across x and plotted the temperature, density, and the velocity component computed as $v_{xz} = \sqrt{v_x^2 + v_z^2}$, which was then normalized by the local Alfvén speed to assess the jet's true speed. These plots are depicted in Figure 5.5. The temperature profile of the jet reveals a structure that consists of two narrow regions with hot plasma and a central region of cold plasma in both simulations. Thus, in both simulations, the first reconnection jet manifests as a multithermal jet, a phenomenon previously observed and has been linked with the presence of plasmoids in the current sheet as numerous of studies indicated (observations and numerical simulations) (Mulay et al., 2017; Zhang & Ni, 2019; Chen et al., 2022; Mulay et al., 2023; Li et al., 2023a). The initial current sheet, formed by the interaction of the emerged magnetic flux with the ambient flux system we observe the formation of plasmoids (not showed here). Eventually the plasmoids are ejected, creating the observed cold central part in the first temperature plot of Figure 5.5. The hot narrow regions are produced by magnetic reconnection that takes place in the upper segment of the current sheet (Ni et al. (2017) and reference therein).

Moreover, it is noted that the FI simulation exhibits hotter lanes than the PI, with the jet's central part being slightly colder in the PI due to the greater adiabatic expansion of the loop. The second plot emphasizes the density of the plasma ejected through the jet, with the first reconnection jet in the FI ejecting more than twice the plasma compared to the PI. This finding aligns with Chapter 3's results and the amount of dense plasma both apexes deliver to the solar surface. The third plot shows that the true speed of the jet is higher in the FI simulation. Reviewing all three plots, we conclude that the spire of the FI jet is slightly larger than that of the PI. The increased temperature and velocity in the FI jet are associated with the efficiency of reconnection in the current sheet, formed by the emerged flux system's interaction with the ambient field. The difference in dense plasma ejection is linked to the volume of plasma brought to the solar surface by both apexes. To understand the disparities in temperature and velocity, further investigation into the current sheet's environment is necessary to elucidate the factors enhancing magnetic reconnection efficiency in the FI simulation.

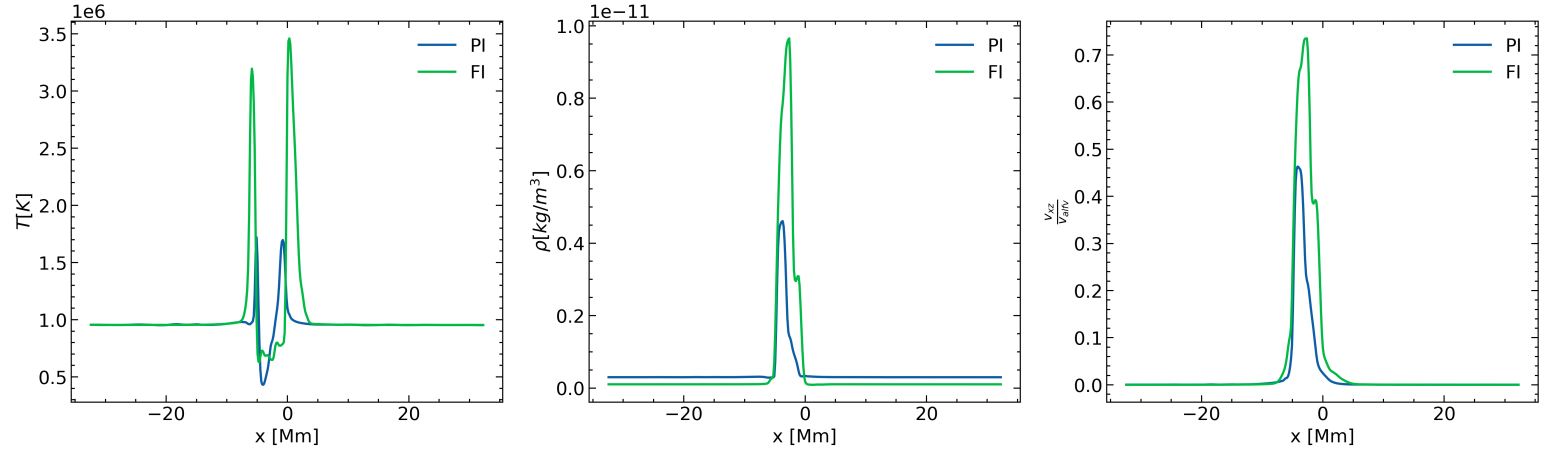


Figure 5.5: 1D plots of temperature, density and the v_{xz} normalized by the local Alfvén velocity at the height 20 Mm and $y=0$.

To quantify the efficiency of magnetic reconnection in our simulation, we compute the dimensionless reconnection rate, denoted as M , defined as the ratio of the inflow velocity (v_{in}) to the Alfvén velocity (v_A) in the current sheet. The Alfvén velocity is a characteristic velocity given by $v_A = \frac{B}{\sqrt{\mu_0 \rho}}$, where B is the magnetic field strength, μ_0 is the vacuum permeability, and ρ is the plasma mass density.

The inflow velocity is ascertained by projecting the plasma velocity vectors onto the direction normal to the current sheet. The normal vector at each point within the current sheet region is determined by the gradient of the magnetic field magnitude, computed as:

$$\mathbf{n} = \frac{\nabla B}{|\nabla B|} \quad (5.2)$$

where ∇B is the spatial gradient of the magnetic field magnitude. This gradient is calculated exclusively within the current sheet region. The current sheet region was computed by keeping the indices that have value greater than $0.8 \cdot \max(a)$ within the domain of interest, alpha parameter is $a = \frac{|J|}{|B|}$. The projection of the plasma velocity vectors (\mathbf{v}) onto the normal vector (\mathbf{n}) yields the inflow velocity component:

$$v_{in} = |\mathbf{v} \cdot \mathbf{n}| \quad (5.3)$$

We calculate the Alfvén velocity by computing the magnetic field and the plasma

density close at the current sheet. The dimensionless reconnection rate M is then expressed as the ratio:

$$M = \frac{\nu_{\text{in}}}{\nu_A} \quad (5.4)$$

A higher M signifies a more dynamic and efficient reconnection process, typically accompanied by more vigorous plasma flows.

The average magnetic reconnection rate has been computed one snapshot before the occurrence of the jet. The average magnetic reconnection rate in PI is 0.009 and in FI is 0.016. By comparing M from PI and FI simulation scenarios, we found that the reconnection rate in the FI case regarding the current sheet that produces the first standard jet is nearly two times greater than PI. It is important to examine the events occurring within the current sheet prior to the onset of the first reconnection jet. Initially, we took a slice along the z -axis and $y = 0$ at various x coordinates to ascertain at which height in both the PI and FI simulations the current density reaches its maximum value. Subsequently, we plotted the current density sliced at this height in the xy -plane, capturing a snapshot just before the first jet's onset in both simulations. These results are presented in Figure 5.6, enabling us to scrutinize the current sheet's structure. Typically, the initial interaction between the emerged flux system and the ambient field results in the formation of a thick current sheet, as illustrated for both the PI and FI simulations in Figure 5.6. Having examined the structure of the current sheet, it is important to study the phenomena occurring within it. We take a slice along y from the contour plots in Figure 5.6 at $x = 0.46$ Mm and plot the density, the magnitude of the magnetic field vector, and the current density to reveal the conditions inside the thick current sheet. The outcomes are depicted in Figure 5.7. The first plot demonstrates that the density within the current sheet in the FI simulation surpasses that in the PI, aligning with the findings discussed in Chapter 3. The second plot indicates a stronger magnetic field in the PI case. The current density plot, which shows that the FI simulation harbors a more intense current than the PI, despite having a weaker magnetic field. In order to find the reason for the enhanced current density in the FI case we computed at height beneath the current sheet the shear angle of the emerged magnetic flux system with the ambient one.

The shear angle between two magnetic field vectors, $\mathbf{B}_{\text{emerging}}$ and $\mathbf{B}_{\text{ambient}}$, is calculated using the following equations:

The magnitude of a vector \mathbf{B} is given by:

$$|\mathbf{B}| = \sqrt{B_x^2 + B_y^2 + B_z^2} \quad (5.5)$$

where B_x , B_y , and B_z are the components of the vector \mathbf{B} .

The dot product between two vectors \mathbf{B} and \mathbf{B}_{amb} is computed as:

$$\mathbf{B} \cdot \mathbf{B}_{\text{amb}} = B_x B_{\text{amb},x} + B_y B_{\text{amb},y} + B_z B_{\text{amb},z} \quad (5.6)$$

where B_x , B_y , and B_z are the components of the vector \mathbf{B} the emerged magnetic flux system, and $B_{\text{amb},x}$, $B_{\text{amb},y}$, and $B_{\text{amb},z}$ are the components of the vector \mathbf{B}_{amb} e.g the ambient field.

The cosine of the angle θ between vectors \mathbf{B} and \mathbf{B}_{amb} is given by:

$$\cos(\theta) = \frac{\mathbf{B} \cdot \mathbf{B}_{\text{amb}}}{|\mathbf{B}| |\mathbf{B}_{\text{amb}}|} \quad (5.7)$$

where $|\mathbf{B}|$ and $|\mathbf{B}_{\text{amb}}|$ are the magnitudes of vectors \mathbf{B} and \mathbf{B}_{amb} , respectively.

Finally, the angle θ is found by taking the inverse cosine (\arccos) of $\cos(\theta)$:

$$\theta = \arccos \left(\frac{\mathbf{B} \cdot \mathbf{B}_{\text{amb}}}{|\mathbf{B}| |\mathbf{B}_{\text{amb}}|} \right) \quad (5.8)$$

We have plotted the shear angle at $y=0$, along x and $z=2.77\text{Mm}$ for the PI and $z=2.31\text{Mm}$ for the FI in figure 5.8. The FI presents a higher shear angle compare to the PI and the maximum difference is 15 degrees.

In the FI simulation, the angle between the emerged magnetic field lines and the ambient ones appears more antiparallel compared to the PI simulation as we show in figure 5.8. This variation in orientation which is influenced by the partially ionized plasma (slippage effect), could play a role in the efficiency of magnetic reconnection. Consequently, the differences in temperature and velocity of the plasmoid-induced jet illustrated in Figure 5.5 can be explained by the disparity in magnetic field line orientation between the PI and FI simulations. This seems to lead to more efficient

magnetic reconnection in the FI simulation, where magnetic energy is converted into thermal and kinetic energy more rapidly, resulting in the observed differences in the temperature and velocity profiles of the jet.

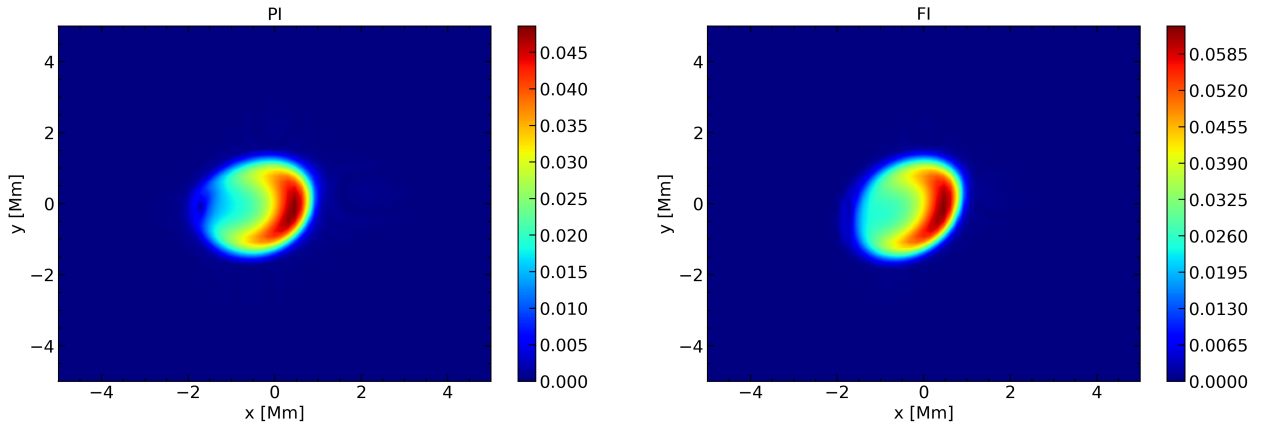


Figure 5.6: Contour plots of the current density one snapshot before the onset of the first reconnection jet in both simulations at $z=3.13$ Mm in the PI and at $z=2.67$ Mm at the FI.

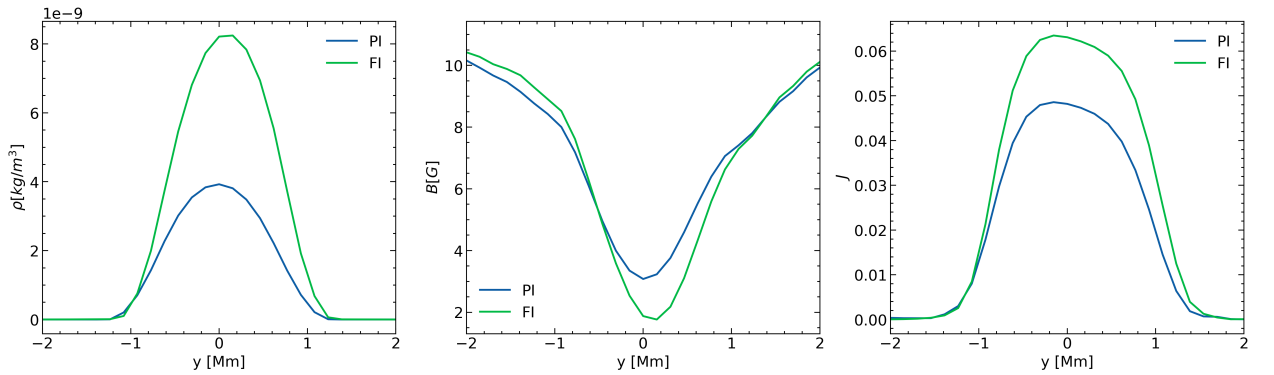


Figure 5.7: 1D plots of density, magnetic field and current density inside the thick current sheet at $x=0.46$ Mm.

The second standard jet appears at $t = 49.24$ minutes in the PI simulation (as indicated by the kinetic energy plot) and at $t = 55.36$ minutes in the FI simulation. We will adopt the same analytical framework as was utilized for the previous jet. Initially, we examine the structure of the second standard jet through contour plots of the logarithm of temperature in the xz midplane, as depicted in Figure 5.9.

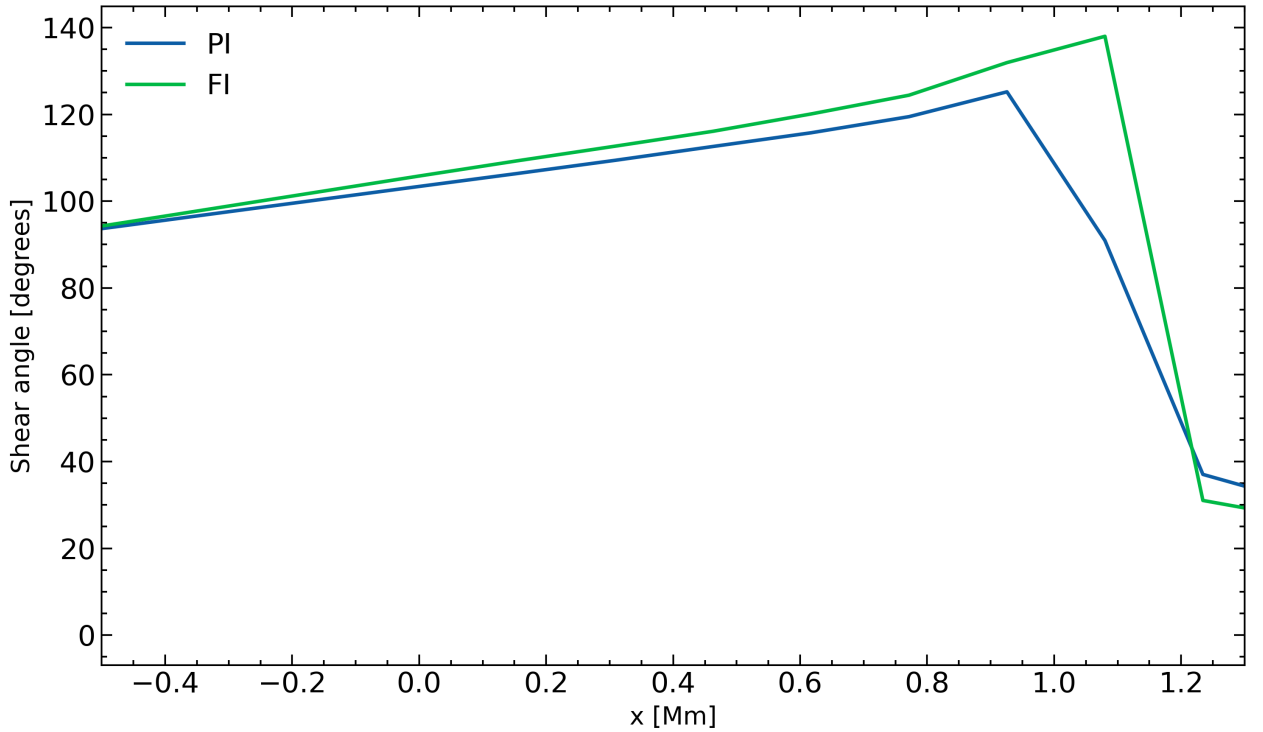


Figure 5.8: 1D plot of the shear angle of the emerged magnetic flux system and the ambient in both simulations at $y=0$, along x and $z=2.31\text{Mm}$ for the FI and $z=2.77\text{Mm}$ for the PI.

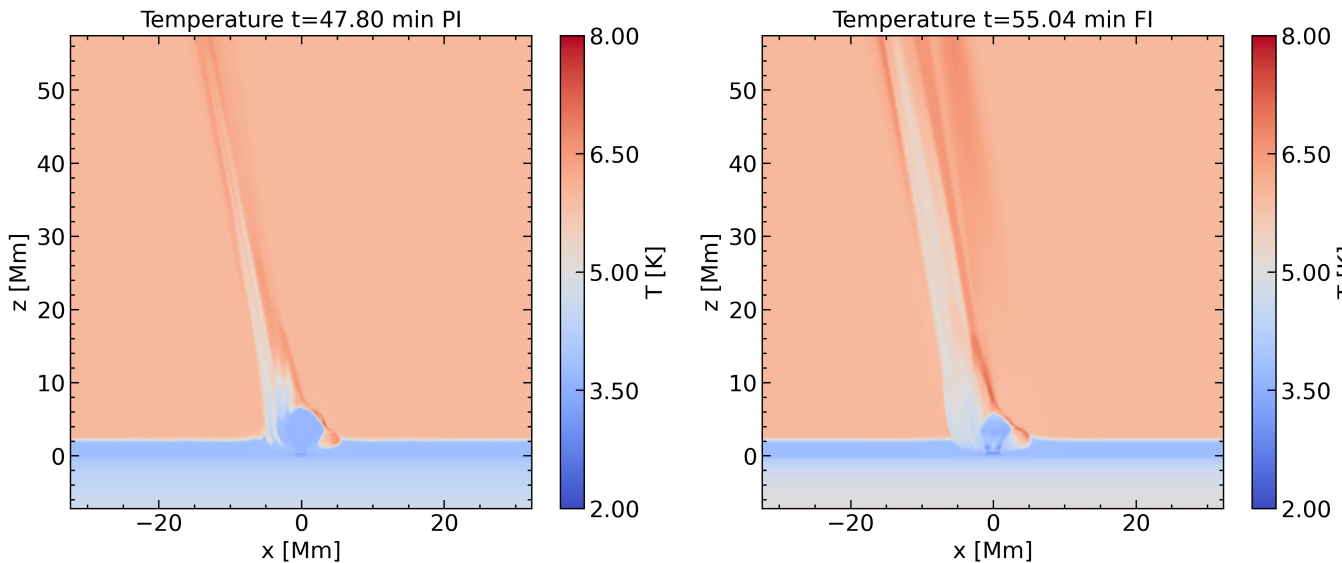


Figure 5.9: Contour plots that depict the logarithm of the temperature at times that capture the second standard jet in both simulations at the xz midplane.

In both cases, there are some common characteristics. One of them is the column

of dense plasma, on the left-hand side of the emerging loop. This is very similar to the “dense wall” which has been discussed in the work by Moreno-Insertis & Galsgaard (2013). On the right-hand side of the emerging loop, there is a hot arcade, which is formed by reconnected fieldlines, after reconnection starts at the current sheet between the emerging and the ambient field. The hot plasma of the arcade is due to compression between the downward reconnection jet and the dense plasma at the top of the arcade. Additionally, a hot jet originating from the current sheet is observed, due to the interaction between the emerged flux system and the ambient field. The spire of the jet is wider in the FI case. To study the jet’s structure, we took a slice along x at a height of 10 Mm in both simulations and plotted the logarithm of the temperature, density, and the ν_{xz} —normalized by the local Alfvén velocity—along the x -axis at $y = 0$. We display the results in figure 5.10. These plots reveal the details of the jet’s structure with greater clarity. The temperature plot shows that the right edge of the spire, in both simulations, is hot plasma, which represents the coronal jet originating from the current sheet due to the interaction of the emerged field with the ambient one.

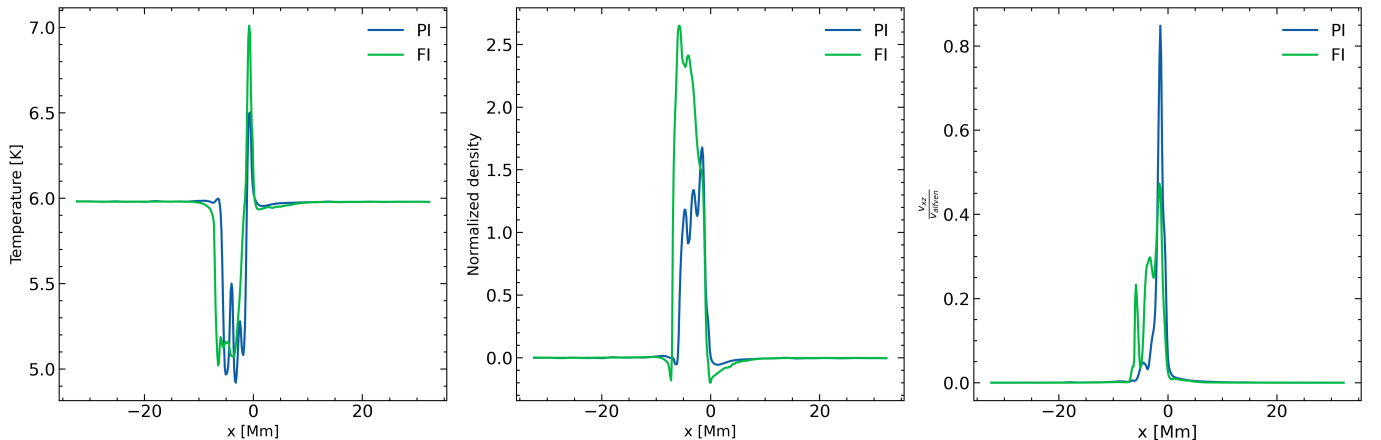


Figure 5.10: 1D plots of logarithm of the temperature, logarithm of the density, and the ν_{xz} normalized by the local Alfvén velocity at $z=20$ Mm and $y=0$.

The second plot depicts the plasma density distribution of the coronal jets.

The last plot displays the velocity of both the hot and cold parts, with the hot part moving faster in the PI simulation, whereas the FI simulation features faster cold parts. To elucidate these differences, we will employ a method akin to that used for analyzing the previous jet. Determining the structure of the current sheet presents a challenge due to its increased curvature. We produced contour plots

of current density at the xz midplane in both simulations at three different times: the onset of the standard jet and two snapshots before, to examine the temporal evolution of the current sheet. Furthermore, we overlaid a polygon on each contour plot to mark the area of the current sheet, facilitating the computation of various variables within the current sheet to monitor its temporal evolution, as illustrated in Figure 5.11. The first row depicts the current sheet before the initial reconnection jet. The second row, a snapshot preceding the coronal standard jet's emergence, reveals a plasmoid ejection in both simulations, in the PI at $x \approx -2$ and $z \approx 6$ and in FI at $x \approx -1.5$ and $z \approx 5$. The third row, coinciding with the onset of the standard jet, shows the current sheet narrowing due to plasmoid departure, enabling direct interaction between the emerged and ambient fields. We will do the same as before and we will try to see what is happening inside the current sheet just to be able to explain the structure of this jet. We computed on each polygon for every snapshot that we displayed on figure 5.11 the current density, joule heating and specific energy terms.

For the PI simulation, the Joule heating term is given by:

$$Q_{\text{PI}} = \eta j_{\parallel}^2 + (\eta + \eta_{\perp}) j_{\perp}^2 \quad (5.9)$$

where Q_{PI} denotes the Joule heating in the PI simulation, η is the ohmic resistivity (uniform), j_{\parallel} is the current density parallel to the magnetic field, η_{\perp} is the perpendicular resistivity, and j_{\perp} is the current density perpendicular to the magnetic field the same as the ones that we defined in chapter 3.

For the FI simulation, the Joule heating term is simpler:

$$Q_{\text{FI}} = \eta j^2 \quad (5.10)$$

where Q_{FI} represents the Joule heating in the FI simulation, η is the ohmic resistivity (uniform), and j is the current density.

We also plotted the specific energy terms in both simulations. In the context of the simulations, we remind that the specific energy equation for the PI plasma is:

$$\epsilon = \frac{k_B T}{\mu_m(\gamma - 1)} + (1 - \xi_n) \frac{X_i}{m_i} \quad (5.11)$$

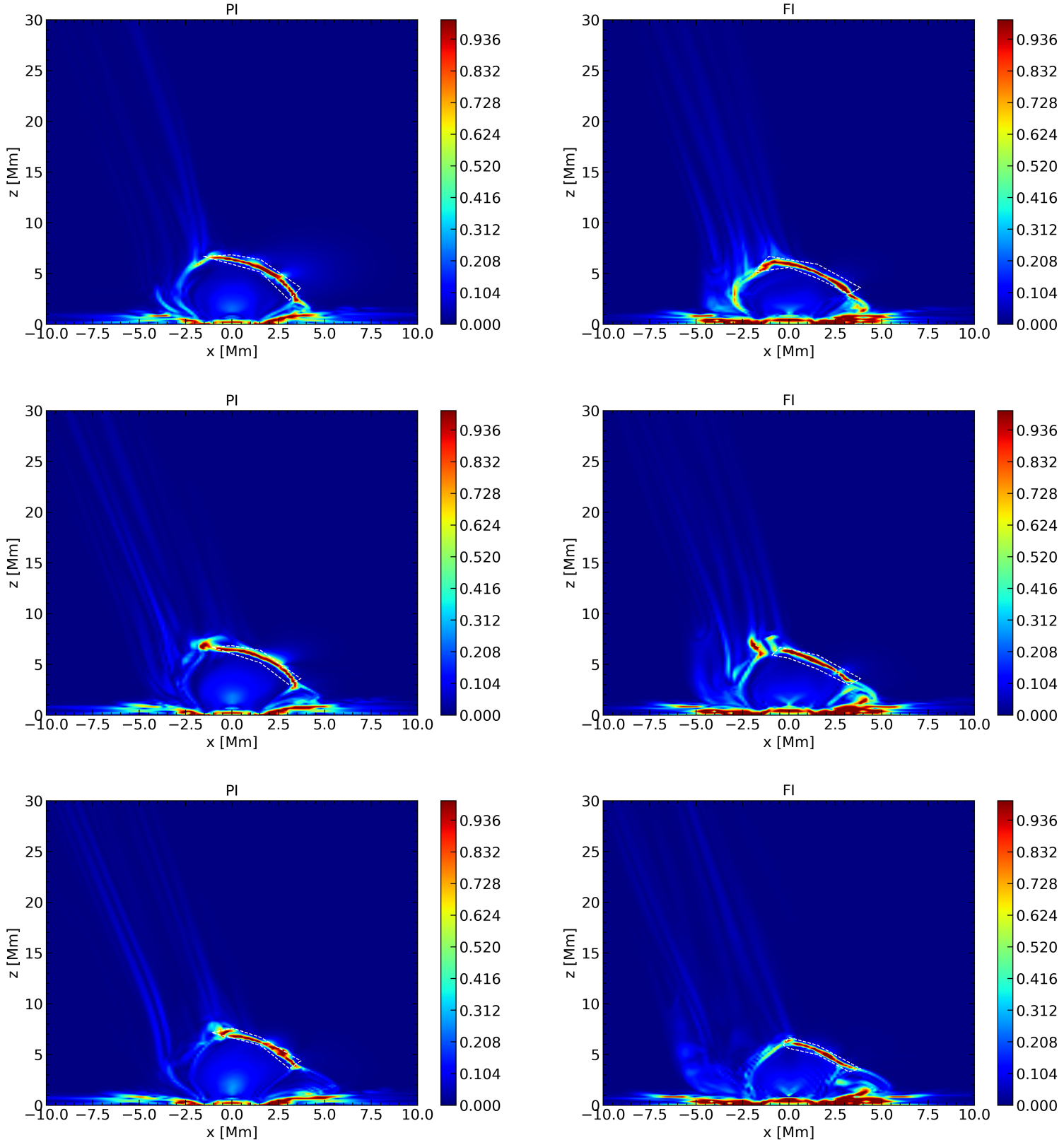


Figure 5.11: Contour plots of alpha ($\alpha = \frac{|J|}{|B|}$) at the xz midplane that capture the curved current sheet. The first row for PI is at $t=44.9$ minutes and for FI at $t=52.14$ minutes, the second row for PI at $t=46.34$ min and for FI at $t=53.58$ min, and the third row for PI at $t=47.795$ min and for FI at $t=55.03$ min.

In this formulation, the first term on the right side of Equation (5.11) represents the thermal energy, while the second term accounts for the ionization potential energy. For the FI plasma, the ionization fraction ξ_n is set to 1, simplifying the specific energy equation by removing the ionization potential term. Therefore, the specific energy for the FI plasma is represented solely by the thermal energy term:

$$\epsilon_{\text{FI}} = \frac{k_B T}{\mu_m(\gamma - 1)} \quad (5.12)$$

In the plots, the term $E1_{\text{PI}}$ corresponds to the first term of Equation (5.11) in the PI simulation, and $E1_{\text{FI}}$ corresponds to Equation (5.12) in the FI simulation. The term $E2_{\text{PI}}$ represents the second term of Equation (5.11), which is the ionization potential energy, exclusive to the PI simulation. The ionization potential energy term in the specific energy equation represents the energy necessary to ionize the gas. In contexts where the plasma is only partially ionized, this term accounts for the portion of the gas undergoing ionization, reflecting the energy required to liberate an electron from its atomic nucleus. It signifies the magnitude of energy needed to counteract the electrostatic forces between the electron and the nucleus, indicating the electron's stability within the atom. The factor $(1 - \xi_n)$ indicates that only a fraction of the atoms, those that are not yet ionized, will contribute to the ionization potential energy in the system. Here, ξ_n represents the neutral fraction, which is the proportion of neutral atoms to the total number of atoms. This term is important for understanding the energy dynamics in PI, where ionization and recombination processes have impacts on the thermal behavior of the system.

We can rearrange the equation to solve for the temperature T :

$$T = \frac{\mu_m(\gamma - 1)}{k_B} \left(\epsilon - (1 - \xi_n) \frac{X_i}{m_i} \right) \quad (5.13)$$

This equation indicate that the ionization-recombination of the neutral atoms can potentially affect the temperature of the plasma. In Figure 5.12, we display the current density, the logarithm of the Joule heating, and the logarithm of the specific energy terms. Inside the polygon, we averaged the values along the z-axis for each x-coordinate before plotting them along the x-axis. The first row corresponds to the polygon that we overlaid in the first row of Figure 5.11, and so forth. The first column shows the current density evolution, with the PI simulation exhibiting

higher values. This could lead to greater magnetic reconnection efficiency, leading to a faster conversion of magnetic energy to thermal and kinetic energy, resulting in a faster and hotter jet. Although this may explain the increased velocity of the PI standard jet as shown in Figure 5.10, the temperature is higher in the FI standard jet.

The second column shows the Joule heating's temporal evolution in both simulations. We observe an increase in Joule heating from the first to the second row in both simulations, which corresponds to times that magnetic reconnection is on its peak and the jet's occurrence from the second to the third row. The last column depicts the temporal evolution of specific energy density terms along with the neutral fraction, the neutral fraction values are depicted in the right y-axis and the dimensionless values of the rest of the quantities on the left y-axis. We previously explained the meanings of E1 PI, E2 PI, and E1 FI. Notably, neutrals were detected within the current sheet as the first and second plot (third column) indicate. The FI simulation consistently shows an increase in thermal energy as magnetic reconnection intensifies, with the highest value at the jet's onset (see the yellow line from the first to the third plot with maximum values of the thermal energy 9.5, 10, 11). Conversely, in the PI simulation, thermal energy (blue line) decreases from the first to the second row as neutrals ionize over time (the red line decreases). Post the second row, the neutrals become fully ionized (the red line is 0 inside the current sheet), and thermal energy increases, but not as substantially as in the FI case. Neutrals in the current sheet can potentially affect the thermodynamics, consuming thermal energy for ionization, as demonstrated by equation 5.13. This effect may explain the temperature differences seen in Figure 5.10. The PI simulation's enhanced current density could lead to more efficient magnetic reconnection for the standard jet, explaining the greater jet velocity compared to the FI simulation, as depicted in Figure 5.10. Furthermore, the difference in jet temperature can potentially be explained by the ionization of neutral atoms in the current sheet, affecting the jet's thermodynamics. We will comment more on this result in the last Chapter.

5.2.4 Comparison and evolution of the eruption driven jets.

We turn our attention now to the eruption driven jets that we have in our simulations. In both simulations as we deduced from figure 5.2 we have 3 eruptive events

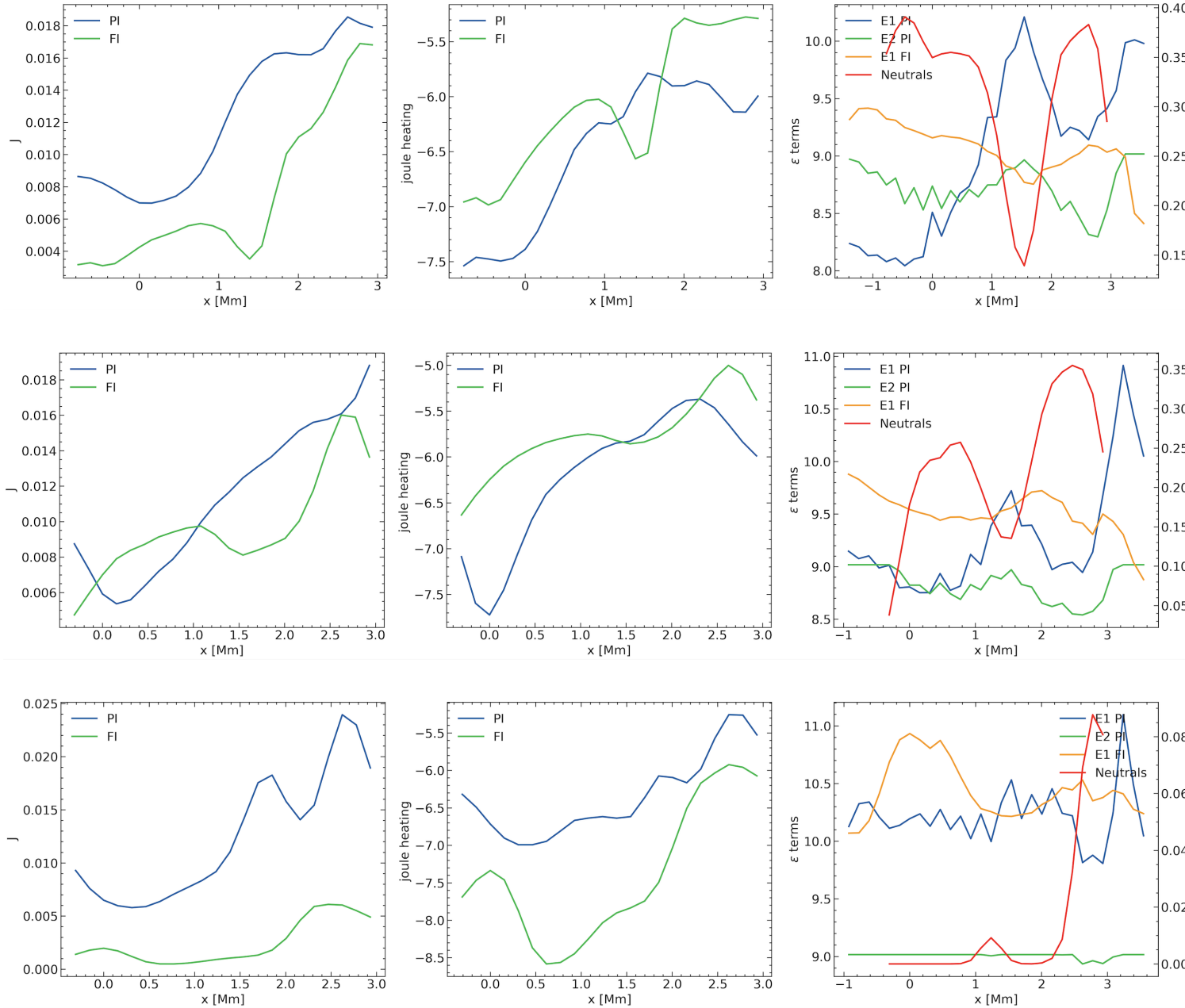


Figure 5.12: One dimensional plots of current density, joule heating and specific energy terms along x inside the polygons that define the current sheet in both simulations. The first row for PI is at $t=44.9$ minutes and for FI at $t=52.14$ minutes, the second row for PI at $t=46.34$ min and for FI at $t=53.58$ min, and the third row for PI at $t=47.795$ min and for FI at $t=55.03$ min.

distinguished by the peaks. Judging from the kinetic energy peak values the third and fourth event in PI might correspond to a blow out jet termed like this by Moore et al. (2010b). According to them the blow out jets have 2 distinct phases, first the envelope field is reconnecting externally with the ambient field and this reduce the magnetic tension of the envelope field (break out reconnection according to Moore et al. (2010b)) and then the magnetic shear arcade that has been created above the PIL from the converging and shearing motions becomes unstable possibly convert to a FR and erupts triggering subsequent reconnection along its trajectory and eventually reconnected and ejected through the open magnetic field lines of the ambient field. This mechanism has been suggested by (Moore et al., 2010b) and it has been shown numerically by (Moreno-Insertis & Galsgaard, 2013; Archontis et al., 2013).

5.2.5 The blowout jets

5.2.6 The dynamic evolution of the blowout jets in PI.

To investigate the dynamic evolution of the blowout jets in PI, it is essential to monitor the distribution of neutrals. This involves visualizing the contour plots of the neutral fraction, the logarithm of the temperature, the logarithm of the density, and the alpha parameter at the xz midplane during the snapshots capturing the blowout jet in PI.

The results are depicted in Figure 5.13. At the first row, the temperature shows again the hot arcade between $x=2-10$ Mm. We have to highlight that this is not the first eruptive event. This hot loop area expands over time. At $x=0$, we observe a structure of neutrals as shown in column 1. We note that this column of neutrals exists for the same reason explained in Chapter 4. This structure is also visible in the temperature plot, indicating cold plasma. In addition to the high concentration of neutrals and its cold nature, the structure is also dense, as evidenced by the density plots in column 3.

Examining the alpha parameter in column 4, we notice a current sheet in the low chromosphere and photosphere, situated above the PIL. The first row shows the current sheet that generated the standard jet ($z=10$ Mm, $x=6$ Mm). At the tip of this structure, we detect the formation of a thin current sheet, likely a result of the

shearing between the field lines of the cold structure and the hot loop.

The second row captures the moment when the current density within the central current sheet intensifies, resulting in Joule heating from Ohmic dissipation. This process generates sufficient thermal energy to ionize the neutrals at the reconnection onset, as observed at $x = 0$ and $z = 3$ Mm in the second plot of the second row. Correspondingly, the last plot in this row shows the enhanced current density at $z = 3$ Mm, pinpointing the magnetic reconnection site.

In the third row, the neutral population decreases due to the heating from the hot reconnection outflow, visible in the temperature contour plot (column 2) at $x = 0$ and $z = 0 - 10$ Mm. This energetic outflow transfers momentum and kinetic energy to the newly formed FR. This magnetic reconnection, probably between the J_s magnetic field lines similar with the ones that we show in chapter 4 will create this hot outflow and the azimuthal oriented ejection of this outflow dictates the field line azimuthal orientation that are involve in this process. The last plot reveals that this hot outflow stimulates magnetic reconnection in its path, as denoted by the more extensive presence of the strong alpha parameter than previously observed.

The fourth row captures the moments preceding the jet, marked by an external reconnection event. This event, between the envelope field and the ambient unipolar field, mirrors the mechanism of a standard jet and leads to a fast X-ray jet- denoted from the values of the temperature and vertical velocity that we will examine later. The reconnection is discernible in the last plot of the fourth row at $x=6$ Mm and $z=14$ Mm. At the same time, the second plot displays a narrow, hot outflow ejected from $x = 6$ Mm and $z = 25$ Mm to the boundary of the box. Additionally, the residual neutral atoms, now sparse, are accelerated by the reconnection outflow toward the right edge of the spire at $x=10$ Mm.

The magnetic field lines, carrying the few remaining neutral atoms, breach the right edge of the spire, propelled by the acquired momentum. This dynamic is evident across all plots in the fourth row, leading to reconnection with new open field lines of the ambient field, thereby broadening the jet's width and spire thus forcing more reconnection events. Notably, at $x=8$ Mm, this process seems to bisect the hot loop, dividing the spire into two distinct segments: one comprising the new open field lines with the residual neutrals and the magnetic structure, and the other, the central magnetic loop.

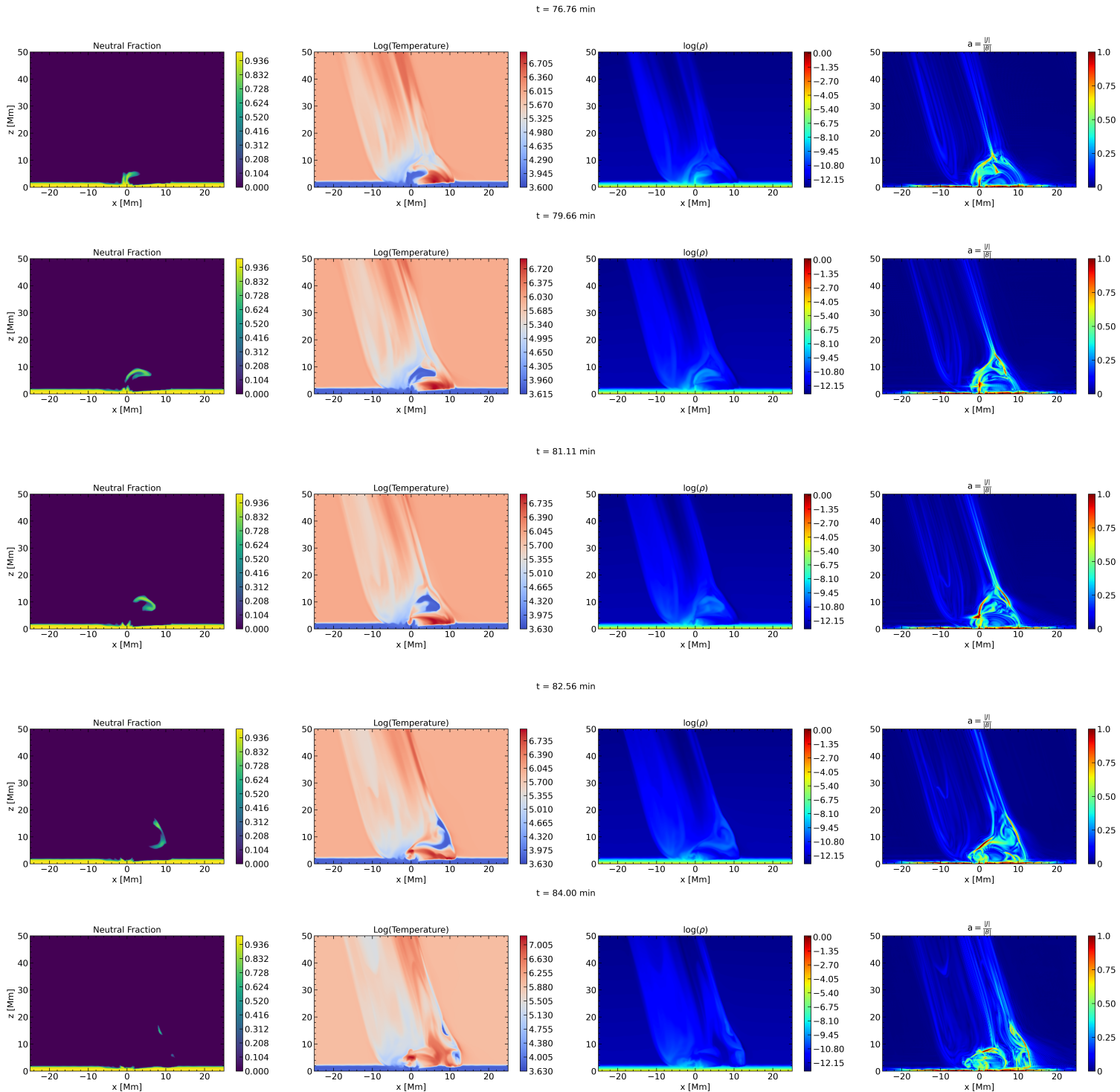


Figure 5.13: Contour plots of the slices of neutral fraction in the xz midplane (column 1), of the logarithm of the temperature in the xz midplane (column 2), of the logarithm of the density (column 3), and of the alpha parameter (column 4) at times of the evolution of the blowout jet.

The fifth row presents the ejection phase of the cold structure. The first plot shows the complete dissipation of neutrals, while the second plot reveals the expulsion of cold plasma between $x=12\text{-}14\text{Mm}$ and $z=2$ to the box's end. The density plot corroborates this, depicting the ejection of dense plasma at the same location, alongside emerging plasma from below at $x=0$. Finally, the last plot highlights the complicated topology that the ejection of the FR leaves at the centre of the magnetic loop and the structure that is ejected from the reconnection with the new open magnetic field lines.

In 5.14, we show the three-dimensional shape of some of the magnetic fieldlines around the centre of the numerical domain at $t=78.21$ minutes for the PI simulation. In this figure, the red fieldlines symbolize the magnetic field lines of the hot loop area. The grey fieldlines represent the open magnetic field lines of the ambient field to the right of the hot loop (positive x -axis) and a section of the emerged segment of the flux tube that has reconnected with these open lines (negative x -axis). The green fieldlines illustrate the envelope magnetic field lines that have extended into the solar atmosphere, while the yellow tubes indicate the lines of the magnetic arcade.

The top plot in figure 5.14 offers a side view, and the bottom plot provides a top view. Both plots feature a horizontal contour plot representing the B_z component at the photospheric height (akin to a magnetogram), with both positive and negative polarities. We will not examine the mechanism that is in play for the eruptive event, from Chapter 4 we highlighted that the magnetic reconnection of the J_s lines plays an important role. The envelope and magnetic arcade field lines appear twisted, emerging into an environment already affected by previous eruptive events. From the top view, it is evident that both groups of field lines are adopting a sigmoidal-like shape. These connectivity patterns align with findings in previous work (e.g. (Moreno-Insertis & Galsgaard, 2013)).

Our aim now is to visualize the position and three-dimensional shape of the neutral/cold structure. We show a visualization of isosurfaces of the neutral fraction and overlaying them onto the same set of field lines depicted in figure 5.14.

In figure 5.15, we present the results of our analysis. The blue isosurface depicts neutral fractions ranging from 0.1 to 0.99. This visualization suggests that the neutrals are situated beneath the envelope field. Observing the top view, which is

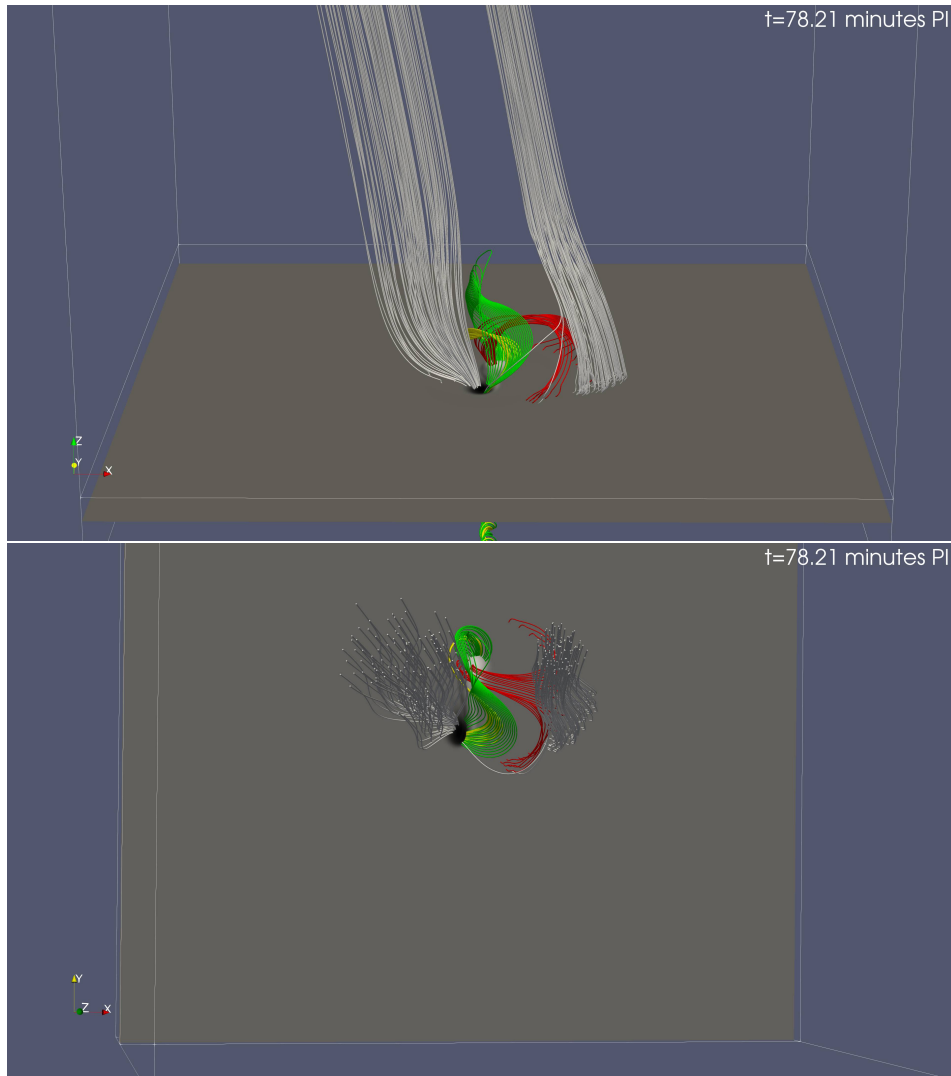


Figure 5.14: 3D plot of some of the magnetic fieldlines at $t=78.21$ minutes in PI as seen on side view (top) and on top view (bottom). The green lines represent the envelope field, the yellow field lines represent the magnetic arcade and the grey lines represent the spire of the jet.

the bottom plot in figure 5.15, we notice that this structure adopts a sigmoidal shape. The positioning of these neutrals appears to be influenced by the slippage effect, akin to the phenomenon described in chapter 3 concerning the behavior of magnetic fields below the photosphere. In this scenario, the newly emerged magnetic field (envelope field) slips through the photosphere and chromosphere, typically without transporting dense material or neutrals like the apex in our early experiments in chapter 3. However, at the photosphere and chromosphere the neutral fraction has maximum value thus as the magnetic field is ascending towards the solar atmosphere

due to the slippage effect an amount of neutrals are “trapped” below the envelope field. Due to the sigmoidal shape of the lines, the neutrals adopt this distinct shape.

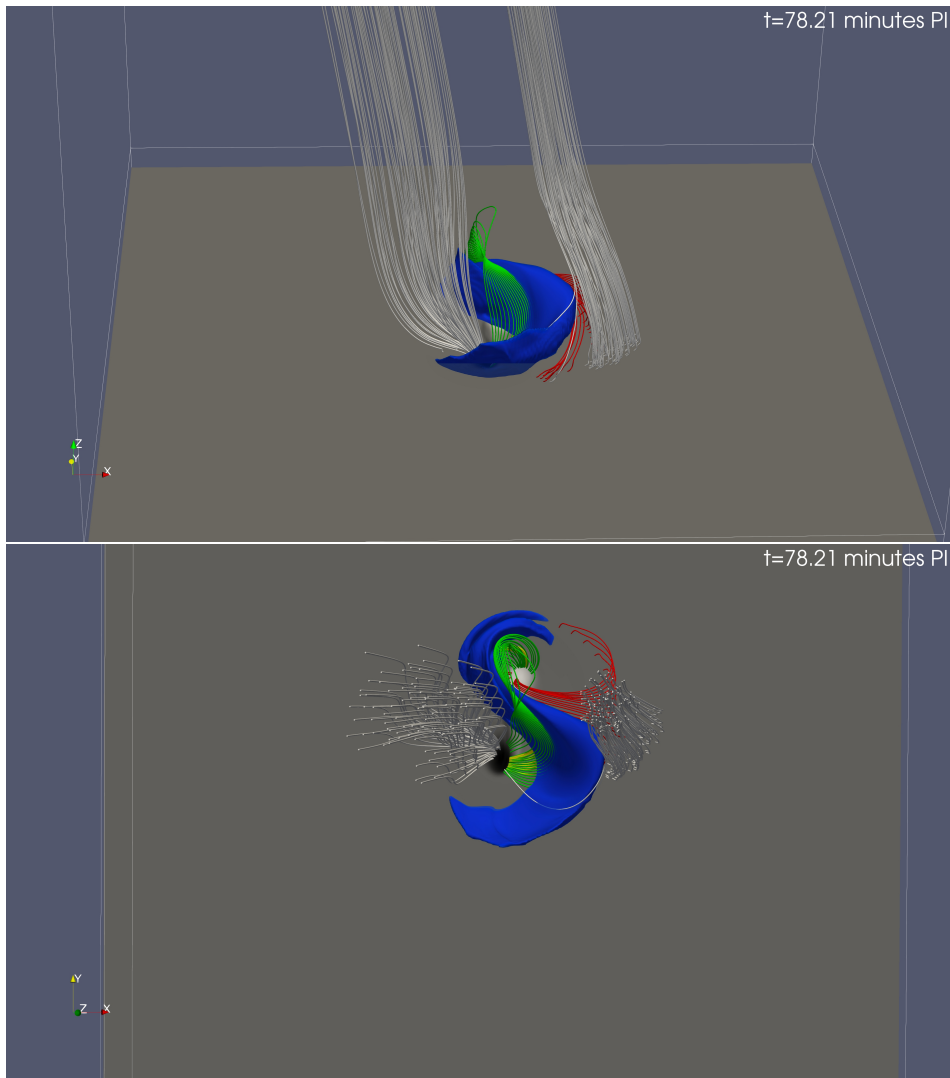


Figure 5.15: 3D plot that highlights the magnetic field line connectivity at $t=78.21$ minutes in PI as seen from the side (top bottom) and from the top (bottom view). The green lines represent the envelope field, the yellow field lines represent the magnetic arcade and the grey lines represent the spire of the jet. The blue isosurface infer the 3D shape of the neutral atoms structure.

The cold structure with neutral atoms might account for a mini-filament structure, characterized by cold plasma, located above the PIL, and exhibiting a sigmoidal shape. Earlier in this chapter, we showed that ν_z is greater in the blowout jets in PI. In Chapter 4, we explained that the higher kinetic energy in PI eruptions is linked

to the height at which internal reconnection occurs. In PI, this reconnection happens at coronal heights, whereas in FI, it occurs below the corona. The local Alfvén velocity is greater in the corona compared to lower heights, resulting in a higher outflow velocity in PI. This effect is further enhanced by the dynamic movement of the mini-filament structure.

This mini-filament, propelled to the right side of the spire and triggering multiple magnetic reconnection sites, along with the different heights of internal reconnection, explains the greater kinetic energy of the blowout jets in the PI scenario, which is an important difference.

5.3 Discussion

In this chapter, we have examined the impact of partially ionized plasma on the dynamics and thermodynamics of solar coronal jets. Our results show that neutrals close at the surface, affect the structure of the emerging field. In turn, this affects the magnetic reconnection between the emerged magnetic flux system and the ambient unipolar field. The slippage effect further impacts the first reconnection jet's density, as the apex of the partially ionized flux tube brings less dense plasma above the photosphere. As a result, the first reconnection jet in the fully ionized case is hotter, denser, and faster compared to PI. This jet is a multithermal jet resulting from plasmoid ejection in both simulations and it emits more kinetic energy in the FI case because of its higher density and velocity. For the second reconnection jet, an inverted-Y-shaped standard jet we find that the PI jet is less hot, less dense, but faster than the FI jet.

Investigating variables within the current sheet, we observed that PI shows higher current density at all examined times, indicating a possible more efficient magnetic reconnection compared to FI. This observation could account for the greater velocity of the PI jet, though its temperature was expected to be higher as well. Examining the role of neutral atoms in the current sheet, we noted their potential impact on the thermodynamics of the plasma. Thermal energy from magnetic reconnection, rather than solely increasing the jet's temperature, also could go toward ionizing the neutral atoms in the current sheet, thus lowering the jet's temperature. This insight suggests that neutrals in the current sheet may play a role

in the thermodynamics of the standard jet, explaining the temperature difference observed in the jet's structure plot. We will discuss about this result further in the next Chapter.

Our analysis revealed that eruption-driven jets in the PI simulation exhibited greater kinetic energy, though the densities, particularly in the blowout jets, were comparable. The notable distinction is found in their velocities, with blowout jets in the PI case achieving higher speeds. 3D visualization of isosurfaces for the neutral fraction, together with magnetic fieldlines, showed that neutrals are located inside a cold structure above the PIL, adopting an overall S-like shape. In fact, this structure is the FR which eventually erupts to drive the onset of the blowout jet. During the eruption, the neutrals are moving upwards, together with the FR, towards the spire of the blowout jet. However, they are not ejected along the spire of the blowout jet because of the intense heating of the plasma due to reconnection between the emerging/erupting field and the ambient field.

We have identified that in both simulations we have the presence of mini-filament structure. Observational studies have linked the presence of mini-filaments with the occurrence of energetic solar jets, noting their role in triggering blowout jets and as the cooler components within such jets (Chen et al., 2008, 2009; Shen, 2012; Shen et al., 2017). Recent work further confirms the role of mini-filaments in initiating blowout jets (Adams et al., 2014; Hong et al., 2014; Li et al., 2015; Sterling et al., 2016).

Regarding the driving of the blowout jets in the two cases, we should mention that there are some common features in both cases. The erupting FR has an S-like shape in both cases. During the eruption, there is internal reconnection underneath the erupting FR and external reconnection between the emerging and the ambient field. This led to the expansion of the jet spire and a blowout jet. Recent observations from Solar Orbiter (Li et al., 2023b) closely monitoring a mini-filament eruption leading to a blowout jet, identify a similar mechanism involving initial internal reconnection followed by external reconnection, which also broadens the jet spire. The PI had more energetic blowout jets in terms of kinetic energy compared to the FI. This is consistent with the results from Chapter 4, which showed more energetic solar eruptions in terms of kinetic energy. The reason is the same: internal reconnection in PI occurs at coronal heights, while in FI, it occurs at lower heights. Therefore, the outflow is faster in PI due to the greater Alfvén velocity at these

heights, potentially explaining the more energetic blowout jets in PI.

Chapter 6

Conclusions

The objective of this thesis was to illuminate the role of partially ionized plasma on the magnetic flux emergence process, solar jets and small-scale solar eruptions.

Our simulations utilized a single-fluid MHD framework, which offers the advantage of being less computationally intensive than multi-fluid MHD. One drawback is the inability to track the evolution of individual species, preventing us from observing specific details like the drift velocity between ions and neutrals or their individual densities. Nevertheless, our methodology includes effective collisional frequencies, a concept detailed in Chapter 3 and first implemented by Leake et al. (2005). This approach enables us to examine the effects of ion-neutral interactions, even though it does not provide separate observations of each interaction.

Chapters 3 and 4 present the results from our initial simulations in an unmagnetized solar atmosphere, comparing PI and FI simulations. We have used the initial conditions by Syntelis et al. (2017). This numerical setup, which showed the onset of solar eruptions was applied identically to our FI and PI. Both shared the same boundary conditions and were designed to have matching initial plasma beta values. However, the distinct equation of states for PI and FI plasmas dictated different initial atmospheric profiles. Thus, we used TFT with the same initial beta plasma but this resulted in a different initial magnetic field magnitude.

Our findings demonstrated that the ion-neutral collisions in the PI simulation's upper convection zone changed the emerging magnetic field's structure, forming a spindle-like shape, in contrast to the more horizontally expansive shape seen in FI

simulation. Additionally, the ion-neutral collision-induced slippage effect influenced the amount of dense plasma transported by the flux tube’s apex to the solar surface in the PI simulation, leading to an earlier atmospheric expansion compared to the heavier apex in the FI case. The ion-neutral collisions also acted as a frictional force along the tube’s axis, which hindered the axis’s complete emergence in the PI case. The heating expected from ion-neutral interactions was also a point of consideration. Along these lines, we explored the thermodynamic influence of ambipolar diffusion in our simulations. We found that ambipolar diffusion could alleviate the intense cooling from the magnetic loop’s adiabatic expansion, yet it did not heat the plasma. To ensure the robustness of our findings, we ran an additional simulation identical to the FI setup but with an initial flux tube magnetic field matching that of the PI. However, due to a differing plasma beta, its evolution was distinct, and the E_{shear} component we examined during eruptive events was greater in the PI, followed by FI, and weakest in the Fib0PI—the simulation with a varied beta plasma. Furthermore, this simulation exhibited a broader horizontal expansion in the emerged magnetic field structure compared to the FI. These observations affirm that the spindle-like shape of the emerged structure in the PI is a direct result of the slippage effect, a manifestation of the partially ionized plasma. This effect also modifies the orientation of magnetic field lines that reach the solar surface, yielding more vertically aligned field lines and causing the bipolar regions to be more circular and compact. Moreover, the magnetogram analysis indicated an absence of magnetic tongues in the PI simulation, linked to the diminished azimuthal magnetic field component, which typically fosters their formation.

This chapter briefly addresses the emergence of solar eruptions within a partially ionized plasma, an innovative aspect of this study as it represents the first observation of an eruptive flux rope in such conditions. To conclude, the preliminary results of these experiments reveal that the partially ionized plasma close to the solar surface affects the emerged magnetic field structure, which, in turn, alters the dynamic evolution of the magnetic loop as it ascends into the solar atmosphere.

In Chapter 4, we found that the expanding magnetic field in the PI simulation exhibited arch-like field lines throughout its structure, a consequence of the “failed” emergence of the flux tube axis due to the reasons explained in Chapter 3 and the altered structure of the emerged magnetic field. An important difference between the simulations is the distinct density and temperature distributions within the

magnetic loop. The plasma below the apex of the emerged magnetic field in PI is less dense, causing it to rise faster than the plasma at the apex. This results in the compression and heating of the plasma at the interface. Over time, as the magnetic loop expands in all directions, more plasma gets compressed and heated. Consequently, this leads to different density and temperature distributions within the magnetic loop, affecting the distribution of neutral atoms present inside the magnetic loop.

The topology of the field lines and the overall structure of the emerged magnetic field lead to distinct differences in the process on the creation of an erupting flux rope in both simulations. In the PI simulation, the emerging field consists of less-twisted field lines because the main axis of the emerging field remains below the solar surface. The J-shaped lines play a key role in the formation of an erupting flux rope in PI. Over time, these J-shaped lines expand vertically and laterally, and their footpoints come closer together and eventually reconnect. While we did not investigate the exact eruption mechanism in PI, it is evident that the internal reconnection of the J-shaped lines will play an important role in alleviating the downward magnetic tension of the envelope field lines, aiding the ejection of the flux rope. In FI, this process is different. The axis remains in the photosphere throughout the simulation, and the sheared magnetic field lines at the PIL reconnect, creating a sigmoidal structure (flux rope) that eventually erupts.

We reported recurrent ejective solar eruptions in both simulations. The energy assessment showed that the PI had weaker magnetized solar eruptions relative to the sub-photospheric axis of the flux tube, but they were twice as fast. Notably, internal reconnection in PI occurs at coronal heights, whereas in FI, it occurs at lower heights (transition region to chromosphere). The outflow speed of the internal reconnection generally matches the local Alfvén speed, which is higher at coronal heights compared to the chromosphere or transition region. This difference, an effect of partially ionized plasma, could explain why the PI eruptions have substantially greater kinetic energy.

In Chapter 5, we present the results from simulations using a unipolar ambient magnetic field. Our goal was to explore the impact of PI plasma on solar coronal jets, maintaining the same setup as in Chapters 3 and 4.

The initial reconnection jet in the FI simulation had greater kinetic energy than

the one in PI. The FI jet was hotter, denser, and faster compared to the PI jet, displaying a multithermal plasma along its spire. This denser nature of the FI ejecta can be explained by the slippage effect, consistent with the findings in Chapter 3. The first current sheet, formed by the interaction of the flux system with the ambient field, was notably thicker in the FI case. Measurements within this current sheet before the first reconnection jet showed higher current density in the FI simulation, indicating more efficient magnetic reconnection. This likely accounts for the higher temperature and velocity of the FI ejecta.

Calculations of the shear angle below the current sheet along the x-axis at $y=0$ revealed a maximum difference of 15 degrees favoring the FI simulation. This closer to antiparallel configuration suggests more effective reconnection and higher current density in FI. This constitute an important effect of the PI as it alters the thermodynamic variables of the first reconnection jet.

The second reconnection jet, with its inverted-Y shape, showed differences between the FI and PI environments. In the FI scenario, the jet emerged from a curved coronal current sheet, displaying higher temperatures and densities but moving slower compared to the PI jet. Over time, the PI current sheet exhibited higher current density, suggesting more effective magnetic reconnection in PI. This likely accounts for the higher velocity of the PI jet.

Further analysis focused on the evolution of thermal energies and, in the case of PI, the energy involved in ionizing neutrals within the current sheet. This investigation highlighted that neutrals present in the current sheet potentially absorb a portion of the generated thermal energy for ionization during the magnetic reconnection process. This interaction within the partially ionized plasma potentially affects the thermodynamics of the standard jet, offering a plausible explanation for the observed temperature differences in the jet's structure. This insight could be important, illustrating how neutrals can impact key thermodynamic properties of solar coronal jets, affecting their temperature characteristics. It should be noted that our simulations do not include heat conduction, which could affect the thermal energy transfer from the magnetic field to the plasma. While this omission may change the impact of this particular result, it suggests that the presence of neutrals in the current sheet could affect the thermodynamics of solar jets. For a more comprehensive understanding, we recommend conducting further simulations with the heat conduction term included to determine the persistence of this effect.

In the final section of this chapter, we explored why the PI simulation produced the most energetically kinetic blowout jets. We noticed some differences in the dynamic evolution of the blowout jets between the two simulations.

To clarify these differences, we depicted the dynamic evolution of neutrals in both 2D and 3D. We found that due to the slippage effect the magnetic arcade drags neutrals within its structure, forming a sigmoidal mini-filament-like structure. This naturally occurring mini-filament influences the thermodynamics of the plasma there, as the neutrals absorb some of the thermal energy keeping the plasma cold. Not all neutrals are ionized, resulting in cooler plasma within the magnetic arcade area compared to FI. Then an internal reconnection occurs maybe between the J_s lines as we have seen in Chapter 4, the exact mechanism of these eruptive events should be examined in a future work. The reconnection upflow from the internal reconnection is pushing the newly formed flux rope toward the spire's edge, leading to multiple magnetic reconnection events with new open ambient field lines. This internal reconnection takes place in coronal heights in comparison with the FI that happens lower. The outflow velocity of this internal reconnection event is greater in PI due to this difference in the height as the Alfvén velocity is greater in coronal heights compare with the Alfvén velocity in lower heights.

We identified the presence of a mini-filament structure in both simulations. The primary differences between the PI and FI eruption-driven jets lie in the location and the field lines involved in the internal reconnection event. As discussed in Chapter 4, in PI, the key lines that come closer and reconnect are the J_s lines, and this occurs at coronal heights. In contrast, in FI, the field lines involved in the internal reconnection event are different, and this event takes place at heights below the corona. These differences may have led to more energetic blowout jets in PI in terms of kinetic energy, due to the greater Alfvén velocity at coronal heights compared to lower heights.

This PhD thesis highlights the importance of partial ionization in the magnetic flux emergence process and associated events, such as solar eruptions and jets, using 3D MHD numerical simulations. The results show that, indeed the inclusion of PI in the simulations has a considerable effect not only on the shape of the 3D structure that emerges above the photosphere but also on how it interacts with the ambient magnetic field. As a consequence, eruptions and jets triggered in the emerging region show differences in their thermo-dynamical evolution between the

PI and FI simulations. We should mention that this is just one of the first attempts towards understanding the nature of PI and its effect on these manifestations of solar magnetic activity. More simulations and comparison with observations is required to advance our knowledge on this research topic.

Bibliography

- Acheson, D. J. 1979, Solar Physics, 62, 23, doi:10.1007/BF00150129
- Adams, M., Sterling, A. C., Moore, R. L., & Gary, G. A. 2014, The Astrophysical Journal, 783, 11, doi:10.1088/0004-637X/783/1/11
- Arber, T., Longbottom, A., Gerrard, C., & Milne, A. 2001, Journal of Computational Physics, 171, 151 , doi:10.1006/jcph.2001.6780
- Arber, T. D., Haynes, M., & Leake, J. E. 2007, The Astrophysical Journal, 666, 541, doi:10.1086/520046
- Archontis, V., & Hood, A. W. 2012, Astronomy and Astrophysics, 537, A62, doi:10.1051/0004-6361/201116956
- Archontis, V., Hood, A. W., & Tsinganos, K. 2013, The Astrophysical Journal, 778, 42, doi:10.1088/0004-637X/778/1/42
- . 2014, Astrophysical Journal Letters, 786, L21, doi:10.1088/2041-8205/786/2/L21
- Archontis, V., Moreno-Insertis, F., Galsgaard, K., Hood, A., & O'Shea, E. 2004, Astronomy and Astrophysics, 426, 1047, doi:10.1051/0004-6361:20035934
- Archontis, V., & Török, T. 2008, Astronomy and Astrophysics, 492, L35, doi:10.1051/0004-6361:200811131
- Athay, R. G., & Thomas, R. N. 1961, Physics of the solar chromosphere
- Avrett, E. H., & Loeser, R. 2008, The Astrophysical Journal Supplement Series, 175, 229, doi:10.1086/523671
- Beck, J. G., & Schou, J. 2000, Solar Physics, 193, 333, doi:10.1023/A:1005258123855

- Beer, J. 2000, in ESA Special Publication, Vol. 463, The Solar Cycle and Terrestrial Climate, Solar and Space weather, ed. A. Wilson, 671
- Berghmans, D., & Clette, F. 1999, Solar Physics, 186, 207, doi:10.1023/A:1005189508371
- Braginskii, S. I. 1965, Reviews of Plasma Physics, 1, 205
- Brown, J. C. 1973, Solar Physics, 29, 421, doi:10.1007/BF00150822
- Brun, A. S., & Zahn, J. P. 2006, Astronomy and Astrophysics, 457, 665, doi:10.1051/0004-6361:20053908
- Caligari, P., Moreno-Insertis, F., & Schussler, M. 1995, The Astrophysical Journal, 441, 886, doi:10.1086/175410
- Cattaneo, F., & Hughes, D. W. 1988, Journal of Fluid Mechanics, 196, 323, doi:10.1017/S0022112088002721
- Chen, F., Rempel, M., & Fan, Y. 2022, The Astrophysical Journal, 937, 91, doi:10.3847/1538-4357/ac8f95
- Chen, H., Jiang, Y., & Ma, S. 2009, Solar Physics, 255, 79, doi:10.1007/s11207-008-9298-1
- Chen, H. D., Jiang, Y. C., & Ma, S. L. 2008, Astronomy and Astrophysics, 478, 907, doi:10.1051/0004-6361:20078641
- Curdt, W., Brekke, P., Feldman, U., et al. 2001, Astronomy and Astrophysics, 375, 591, doi:10.1051/0004-6361:20010364
- Emonet, T., & Moreno-Insertis, F. 1998, The Astrophysical Journal, 492, 804, doi:10.1086/305074
- Fan, Y. 2001a, The Astrophysical Journal, 546, 509, doi:10.1086/318222
- . 2001b, Astrophysical Journal Letters, 554, L111, doi:10.1086/320935
- . 2009, The Astrophysical Journal, 697, 1529, doi:10.1088/0004-637X/697/2/1529
- Fan, Y., Fisher, G. H., & McClymont, A. N. 1994, The Astrophysical Journal, 436, 907, doi:10.1086/174967

- Golub, L., & Pasachoff, J. M. 1997, *The Solar Corona*
- Guglielmino, S. L., Bellot Rubio, L. R., Zuccarello, F., et al. 2010, *The Astrophysical Journal*, 724, 1083, doi:10.1088/0004-637X/724/2/1083
- Haigh, J. D. 2007, *Living Reviews in Solar Physics*, 4, 2, doi:10.12942/lrsp-2007-2
- Hathaway, D. H., Beck, J. G., Bogart, R. S., et al. 2000, *Solar Physics*, 193, 299, doi:10.1023/A:1005200809766
- Hong, J., Jiang, Y., Yang, J., et al. 2014, *The Astrophysical Journal*, 796, 73, doi:10.1088/0004-637X/796/2/73
- Howe, R., Christensen-Dalsgaard, J., Hill, F., et al. 2005, *The Astrophysical Journal*, 634, 1405, doi:10.1086/497107
- Hughes, D. W. 2007, in *The Solar Tachocline*, ed. D. W. Hughes, R. Rosner, & N. O. Weiss, 275
- Jiang, C., Duan, A., Feng, X., et al. 2019, *Frontiers in Astronomy and Space Sciences*, 6, 63, doi:10.3389/fspas.2019.00063
- Kano, R., Shimizu, T., & Tarbell, T. D. 2010, *The Astrophysical Journal*, 720, 1136, doi:10.1088/0004-637X/720/2/1136
- Khomenko, E., & Collados, M. 2012, *The Astrophysical Journal*, 747, 87, doi:10.1088/0004-637X/747/2/87
- Kichatinov, L. L., & Rüdiger, G. 1996, *Astronomy Letters*, 22, 279
- Kosovichev, A. G., & Zharkova, V. V. 1998, , 393, 317, doi:10.1038/30629
- Leake, J. E., & Arber, T. D. 2006, *Astronomy and Astrophysics*, 450, 805, doi:10.1051/0004-6361:20054099
- Leake, J. E., Arber, T. D., & Khodachenko, M. L. 2005, *Astronomy and Astrophysics*, 442, 1091, doi:10.1051/0004-6361:20053427
- Leake, J. E., & Linton, M. G. 2013, *The Astrophysical Journal*, 764, 54, doi:10.1088/0004-637X/764/1/54
- Leake, J. E., Linton, M. G., & Antiochos, S. K. 2014, *The Astrophysical Journal*, 787, 46, doi:10.1088/0004-637X/787/1/46

- . 2022, *The Astrophysical Journal*, 934, 10, doi:10.3847/1538-4357/ac74b7
- Leake, J. E., Linton, M. G., & Török, T. 2013, *The Astrophysical Journal*, 778, 99, doi:10.1088/0004-637X/778/2/99
- Li, X., Keppens, R., & Zhou, Y. 2023a, *Astrophysical Journal Letters*, 947, L17, doi:10.3847/2041-8213/acc9ba
- Li, X., Yang, S., Chen, H., Li, T., & Zhang, J. 2015, *Astrophysical Journal Letters*, 814, L13, doi:10.1088/2041-8205/814/1/L13
- Li, Z. F., Cheng, X., Ding, M. D., et al. 2023b, *Astronomy and Astrophysics*, 673, A83, doi:10.1051/0004-6361/202245814
- Lindsey, C., & Braun, D. C. 2000, *Science*, 287, 1799, doi:10.1126/science.287.5459.1799
- MacTaggart, D., Guglielmino, S. L., Haynes, A. L., Simitev, R., & Zuccarello, F. 2015, *Astronomy and Astrophysics*, 576, A4, doi:10.1051/0004-6361/201424646
- Magara, T., & Longcope, D. W. 2001, *Astrophysical Journal Letters*, 559, L55, doi:10.1086/323635
- Manchester, IV, W., Gombosi, T., DeZeeuw, D., & Fan, Y. 2004, *The Astrophysical Journal*, 610, 588, doi:10.1086/421516
- Martínez-Sykora, J., De Pontieu, B., & Hansteen, V. 2012, *The Astrophysical Journal*, 753, 161, doi:10.1088/0004-637X/753/2/161
- Martínez-Sykora, J., Moreno-Insertis, F., & Cheung, M. C. M. 2015, *The Astrophysical Journal*, 814, 2, doi:10.1088/0004-637X/814/1/2
- Matthews, P. C., Hughes, D. W., & Proctor, M. R. E. 1995, *The Astrophysical Journal*, 448, 938, doi:10.1086/176022
- Moore, R. L., Cirtain, J. W., Sterling, A. C., & Falconer, D. A. 2010a, *The Astrophysical Journal*, 720, 757, doi:10.1088/0004-637X/720/1/757
- . 2010b, *The Astrophysical Journal*, 720, 757, doi:10.1088/0004-637X/720/1/757
- Moreno-Insertis, F., & Emonet, T. 1996, *Astrophysical Journal Letters*, 472, L53, doi:10.1086/310360

- Moreno-Insertis, F., & Galsgaard, K. 2013, *The Astrophysical Journal*, 771, 20, doi:10.1088/0004-637X/771/1/20
- Moreno-Insertis, F., Galsgaard, K., & Ugarte-Urra, I. 2008, *Astrophysical Journal Letters*, 673, L211, doi:10.1086/527560
- Mulay, S. M., Del Zanna, G., & Mason, H. 2017, *Astronomy and Astrophysics*, 598, A11, doi:10.1051/0004-6361/201628796
- Mulay, S. M., Tripathi, D., Mason, H., Del Zanna, G., & Archontis, V. 2023, , 518, 2287, doi:10.1093/mnras/stac3035
- Murray, M. J., Hood, A. W., Moreno-Insertis, F., Galsgaard, K., & Archontis, V. 2006, *Astronomy and Astrophysics*, 460, 909, doi:10.1051/0004-6361:20065950
- Nandy, D. 2011, in *Astronomical Society of India Conference Series*, Vol. 2, *Astronomical Society of India Conference Series*, 91–100
- Ni, L., Zhang, Q.-M., Murphy, N. A., & Lin, J. 2017, *The Astrophysical Journal*, 841, 27, doi:10.3847/1538-4357/aa6ffe
- Nóbrega-Siverio, D., Moreno-Insertis, F., Martínez-Sykora, J., Carlsson, M., & Szydlarski, M. 2020, *Astronomy and Astrophysics*, 633, A66, doi:10.1051/0004-6361/201936944
- Parker, E. N. 1955, *The Astrophysical Journal*, 121, 491, doi:10.1086/146010
- Parnell, C. E., & De Moortel, I. 2012, *Philosophical Transactions of the Royal Society of London Series A*, 370, 3217, doi:10.1098/rsta.2012.0113
- Perez, A., Mussack, K., Däppen, W., & Mao, D. 2009, *Astronomy and Astrophysics*, 505, 735, doi:10.1051/0004-6361/20077713
- Priest, E. 2012, in *Comparative Magnetic Minima: Characterizing Quiet Times in the Sun and Stars*, ed. C. H. Mandrini & D. F. Webb, Vol. 286, 3–14
- Priest, E. 2014, *Magnetohydrodynamics of the Sun*
- Raouafi, N. E., Patsourakos, S., Pariat, E., et al. 2016, , 201, 1, doi:10.1007/s11214-016-0260-5

- Savcheva, A., Cirtain, J., Deluca, E. E., et al. 2007, Publications of the Astronomical Society of Japan, 59, S771, doi:10.1093/pasj/59.sp3.S771
- Shen, Y. 2012, in 39th COSPAR Scientific Assembly, Vol. 39, 1774
- Shen, Y., Liu, Y., Tian, Z., & Qu, Z. 2017, The Astrophysical Journal, 851, 101, doi:10.3847/1538-4357/aa9af0
- Shibata, K., Nozawa, S., & Matsumoto, R. 1992, Publications of the Astronomical Society of Japan, 44, 265
- Shibata, K., & Tanuma, S. 2001, Earth, Planets, and Space, 53, 473, doi:10.1186/BF03353258
- Shimizu, T., Tsuneta, S., Acton, L. W., Lemen, J. R., & Uchida, Y. 1992, Publications of the Astronomical Society of Japan, 44, L147
- Shimojo, M., & Shibata, K. 2000, The Astrophysical Journal, 542, 1100, doi:10.1086/317024
- Spitzer, L. 1962, Physics of Fully Ionized Gases
- Sterling, A. C., Moore, R. L., Falconer, D. A., et al. 2016, The Astrophysical Journal, 821, 100, doi:10.3847/0004-637X/821/2/100
- Stix, M. 1991, The Sun. an Introduction
- . 2002, The sun: an introduction
- . 2004, The sun : an introduction
- Syntelis, P., Archontis, V., & Tsinganos, K. 2017, The Astrophysical Journal, 850, 95, doi:10.3847/1538-4357/aa9612
- Tobias, S. M., Weiss, N. O., & Kirk, V. 1995, , 273, 1150, doi:10.1093/mnras/273.4.1150
- Toriumi, S., & Yokoyama, T. 2011, The Astrophysical Journal, 735, 126, doi:10.1088/0004-637X/735/2/126
- van Ballegooijen, A. A., & Martens, P. C. H. 1989, The Astrophysical Journal, 343, 971, doi:10.1086/167766

Vernazza, J. E., Avrett, E. H., & Loeser, R. 1981, , 45, 635, doi:10.1086/190731

Zhang, Q. M., & Ni, L. 2019, The Astrophysical Journal, 870, 113, doi:10.3847/1538-4357/aaf391